A STUDY OF HVAC CHANNEL FOR 60 GHZ INDOOR HIGH-SPEED

WIRELESS COMMUNICATIONS

by

Esha Bangar

APPROVED BY SUPERVISORY COMMITTEE:

___________________________________________

Kamran Kiasaleh, Chair

___________________________________________

Issa M.S. Panahi

___________________________________________

Randall E. Lehmann

___________________________________________

Rashaunda Henderson

To my mother

A STUDY OF HVAC CHANNEL FOR 60 GHZ INDOOR HIGH-SPEED

WIRELESS COMMUNICATIONS

by

ESHA BANGAR, BE, M. TECH

DISSERTATION

Presented to the Faculty of

The University of Texas at Dallas

in Partial Fulfillment

of the Requirements

for the Degree of

DOCTOR OF PHILOSOPHY IN

ELECTRICAL ENGINEERING

THE UNIVERSITY OF TEXAS AT DALLAS

August 2021

ACKNOWLEDGEMENTS

I would like to express my utmost gratitude towards my PhD advisor, Dr. Kamran Kiasaleh for his continuous support throughout my degree, guiding me with my research and other extremely useful projects. I will be forever grateful for his patience, motivation and enthusiasm, and immense theoretical and practical knowledge. His guidance not only helped me in understanding the various aspects of research but also shaping my personality to deal with the complexities of everyday life. I could not have imagined having a better advisor and mentor for my PhD study.

I would also like to thank rest of my PhD committee, starting with examination chair, Dr. Chandrasekaran, Dr. Henderson, Dr. Lehmann and Dr. Panahi for their support, encouragement, insightful comments and helpful suggestions. The final version of my dissertation was shaped because of the hard but extremely meaningful questions posed by the committee members. My sincere thanks also go to the team at Ansys lead by Mr. Kezhong Zhao, for his excellent guidance during the one-year long internship at Ansys. His technical acumen and will to guide the future engineers, helped me immensely in developing my dissertation's final chapter.

Lastly, I would like to acknowledge the efforts of the people who mean the most in my life, my family, and friends. My dad Rajendra Bangar, who supported me always and picked me up every time I fell apart, without him, I would not be where I am. My boyfriend, Dr. Akash Jaggi, M.D., there can never be enough words to describe the love, support and motivation, he has showered on me. He is the only one who deserves the sole credit of encouraging me to complete this dissertation. Also, my friends Anusha Mohan, Merve Apalak and Sweekriti Deshmukh, thank you for the sleepless nights, endless talks and lending me the sympathetic ear when I needed it the most.

Thank you, Lord Almighty for giving me the means to continue and excel in my journey.

July 2021

A STUDY OF HVAC CHANNEL FOR 60 GHZ INDOOR HIGH-SPEED WIRELESS COMMUNICATIONS

Esha Bangar, PhD
The University of Texas at Dallas, 2021

Supervising Professor: Kamran Kiasaleh, Chair

With the deployment of the fifth generation (5G) wireless communications systems, research and practical implementation work on millimeter wave (mm-wave) technology has gained tremendous momentum. With the evident advantages and obstacles with employing higher frequency signals, there is a demand for technological advancements required for the implementation of the millimeter wave systems in indoor communication settings. The wavelength of the mm-wave at 60 GHz is 5 mm, due to which the reception of mm-wave suffers from the propagation loss which is around 50 dB for a distance of 1 meter. Further, the small wavelength also leads to substantial losses by objects present inside a building. To gain further insight on this, wooden walls and doors lead to an attenuation loss of 20 dB, concrete walls would cause 40 dB, glass door would lead to an attenuation of around 16 dB and lastly human body accounts for an attenuation of 35 dB.

Hence, the wireless mm-wave channels with substantial path and multipath propagation losses turn out to be the biggest hurdles in the implementation of the mm-wave wireless systems. In

order to circumvent this limitation, in this study, we propose the use of heating, ventilation and air conditioning (HVAC) ducts for the transmission of mm-wave signals. These ducts act as waveguides, providing an electrically insulated, linear channels which are already present in most indoor constructions.

To establish the viability of HVAC duct mm-wave channels, we conduct experiments using the WiGig compliant transceiver chipsets as the transmitter and receiver. The experiments involve measuring the various RF parameters, such as signal-to-noise ratio (SNR), error vector magnitude (EVM), received signal strength indicator (RSSI), received signal power indicator (RSPI), packet transmission and reception percentage, and bit rate. Initial experimentation involves comparison of the results between a straight HVAC duct and free space for various transmitter-receiver separation, alignment of the transmitter and receiver, and variation in the height of the transmitter/receiver from the ground. Subsequent experiments are performed considering the different bend angles, such as $45°, 90°, 180°$ (U shape), and S shape of the HVAC duct, resulting in results which are similar to that of a straight duct.

The dissertation provides theoretical calculation of the duct channel frequency response for the overall duct system using transfer matrix theory and calculation of the power delay profile. Different dispersion phenomena are also explored. To further substantiate the results, image-theory based ray-tracing algorithms using MATLAB are developed. The experimental, theoretical, and simulation results are shown to correlate favorably, thereby allowing the extension of the results in this study to transmission scenarios of mm-waves for larger distances in indoor environment. We also propose and study a mm-wave microstrip patch antenna, which forms an important sub-component of the mm-wave systems. The proposed antenna is a low-profile, circularly polarized patch antenna that uses two substrate layers and provides high gain for a broad bandwidth.  The results obtained in this dissertation, in terms of the RSSI and throughput, establish the viability of the HVAC duct channel for the transmission of 60 GHz mm-wave wireless signals in indoor environments.

TABLE OF CONTENTS

LIST OF FIGURES

LIST OF TABLES

# CHAPTER 1

# INTRODUCTION

## 1.1 Problem Statement

The global proliferation of high-speed mobile device, including smartphones, laptops, and other multi-media applications are creating unparalleled challenges for wireless communication industry which has to address this demand while dealing with the limited available spectrum. Due to the large demand for spectrum, currently available radio frequency (RF) bands have become quite crowded. As today's cellular providers attempt to deliver high quality, low latency video and multimedia applications for wireless devices, they are limited to a carrier frequency spectrum ranging between 700 MHz and 6 GHz. Servicing legacy users with older inefficient cellphones as well as customers with newer smartphones requires simultaneous management of multiple technologies in the same band-limited spectrum. Currently, allotted spectrum for operators is divided into disjoint frequency bands, each of which is utilized by technologies which require unique radio network infrastructure that must deal with varying propagation characteristics and building penetration losses. In USA, five generations of wireless communication systems have been implemented, with a progression of one generation to another in every decade, starting from 1980s.

Table 1.1. Brief description of different wireless communication generations

| | |
|---|---|
| First Generation | Basic analog FM cellular systems for voice communication |
| Second Generation | Digital modulation, Time division, code division multiple access (CDMA), data and voice services. |
| Third Generation | Wideband-CDMA and high-speed packet access (HSPA) providing high speed internet access, improved video and audio capabilities. Later Evolved HSPA was also released. |
| Fourth Generation | International Mobile Telecommunications-Advanced (IMT-Advanced) standard, LTE advanced technology as a part supporting orthogonal frequency division multiplexing (OFDM), Multiple-Input Multiple-Output (MIMO), providing multi-stream transmission, improved spectrum efficiency and link quality, interference mitigation via adaptive beamforming using antenna arrays. |
| Fifth Generation | New spectrum allocation including 24 GHz, 28 GHz and millimeter wave (mm-wave) band 60/70/80/90 GHz. The new spectrum will lead to lower latency, faster data rates along with the use of massive MIMO, mm-wave and phased array antennas. |

However, in order to further enhance the quality of services and support the load of users, more spectrum (larger bandwidth) to accommodate higher data rates for various multi-media applications is required. With the growing number of users, the required aggregate network capacity will be higher. Therefore, one possibility is to increase the bandwidth, which is a crucial part of 5G through the use of millimeter waves (mm-waves) [1], [2]. It is noteworthy that, in order to distribute mm-wave, a line-of-sight (LOS) link is needed. Although LOS links can be accommodated in outdoor environment when propagation distances are small, the distribution of mm-wave signals in an indoor environment is an issue as mm-wave signals suffer substantial losses due to any physical obstruction of the LOS links. Hence, this is a major challenge to overcome toward utilizing mm-wave spectrum in an efficient manner for 5G systems and beyond.

### 1.2 Introduction to mm-wave

In current wireless communication technologies, several different frequency bands are used for the different services. Microwave signals are electromagnetic waves that lie in frequency band of 300 MHz (100 cm) and 300 GHz (0.1 cm) correspondingly have a wavelength ranging from a few cm to a minimum wavelength of 1 mm. Further, International Telecommunications Union (ITU) has divided the microwave band into four 4 sub-bands as shown in Table 1.2 [153][153]. These bands due to their unique properties support different and specific applications. However, unlike low frequencies, these waves do not reflect through the ionosphere and therefore are limited to line-of-sight (LOS) communication only.

Table 1.2. ITU designation of microwave spectrum

| Band Name | Frequency | Wavelength |
|---|---|---|
| Ultra-high frequency | 300 MHz – 3 GHz | 1 m – 100 mm |
| Super high frequency | 3 GHz – 30 GHz | 100 mm – 10 mm |
| Extremely high frequency | 30 GHz – 300 GHz | 10 mm – 1 mm |
| Tera Hertz high frequency | 300 GHz – 3 THz | 1 mm – 100 $\mu$m |

Table 1.3. IEEE designation of microwave spectrum

| Band Name | Frequency (GHz) |
|---|---|
| L | 1 - 2 |
| S | 2 – 4 |
| X | 8 – 12 |
| Ku | 12 – 18 |
| K | 18 – 27 |
| Ka | 27 – 40 |
| Q | 30 – 50 |
| U | 40 – 60 |
| V | 60 - 75 |
| W | 75 – 110 |
| Mm or G | 110 - 330 |

The International Telecommunication Union categorizes mm-wave band in the range of 30 to 300 GHz as extremely high frequency. In 1895, J.C. Bose developed the first mm-wave communication system which consisted of Spark transmitter, polarizer, coherer, horn antenna, dielectric lens and cylindrical diffraction grafting [153]. In his experiments, he considered a distance of 23 m between the transmitter and the receiver, and the line of sight was also obstructed by two intervening walls. The experiment showed that communication was possible at such high frequencies supporting a very high data rate due to the availability of large bandwidth. Recently, there has been an interest in mm-wave bands (including 60 GHz band), leading to the development of WiGig standard, which allows for 5 GHz unlicensed spectrum [3]. Several papers have been published in the last few years suggesting that mm-wave frequencies can alleviate the burden from the currently saturated 700 MHz to 2.6 GHz radio spectrum bands for wireless communications. The initial allocation of 60 GHz (57–59 GHZ) spectrum for commercial consumers was made by Federal Communications Commission (FCC) in 1995 and it was proposed to be used for unlicensed purposes. It was noted that the spectrum would be optimum for short-range, high data rate, broadband applications [4]. Due to the limited short-range considered for the transmission, interference was minimal and could be further decreased by the use of narrow beamwidth antennas operating in the direct line-of-sight range [5], [6]. FCC expanded the mm-wave band in the next decade to include frequency range from 57 GHz to 64 GHz. The large bandwidth available at this band increases the chances for a more versatile, high bandwidth and extremely high data rate providing spectrum throughout the world which can be used for WiFi and other license-free data communication applications.

Therefore, mm-wave systems, including the 60 GHz frequency systems, are promising candidates for the next generation short-range, high date rate wireless services allocated in United States, Canada, Japan, Europe, Australia, and Korea. This band is expected to support up to a 1 giga bits-per-second (Gb/s) throughput for low mobility wireless local area networks. The effort is aiming at multigigabit multimedia applications [7]-[15].

### 1.3 Indoor mm-wave

Communication channels using mm-wave signals have become the natural choice for high-speed applications due to their large bandwidths and data rates. Some of the earliest works related to mm-wave envisioned providing multi-Gbps data rate over indoor communication systems. These works were published as early as late 1990s. With the deployment of the fifth generation (5G) wireless networks, the importance of mm-wave systems has increased. The mm-wave frequency range proposed for WiGig has four channels, ranging from 52 GHz to 71 GHz. Particularly the spectrum from 58 GHz to 62 GHz is very attractive as it is unlicensed and has been accepted in several different countries around the globe. As part of 5G initiative, the 3$^{rd}$ generation project partnership (3GPP) has defined the enhanced mobile broadband (eMBB) Indoor Hotspot scenario as a natural case study for indoor mm-wave mobile networks [16]-[18]. The main motive of this study is to provision small-cell coverage of high data rates to a user population within a confined area. Typical examples for this type of scenario include an office, airport, or shopping complexes [19]. Several research works are dedicated towards understanding the number of required access points, deployment locations, and effective network settings with system-level evaluation of the mm-wave channel [20]-[28].

### 1.4 Advantages of using mm-wave

There are several obvious advantages of using mm-wave channels. The large bandwidth available at this band provides the user extremely high data rates and makes multi-Gbps, short-range wireless communications possible. Further, due to the small wavelength, the radio hardware and the antennas required are smaller in size as compared to the previous generations. This further enables in the efficient generation of small antenna arrays required by various multiple-input–multiple output systems for portable devices like laptops, mobile phones, etc. Recently, there have been significant advances in the development of technologies related to 60-GHz circuits, enabling the development of low-cost radio devices. Furthermore, the small beamwidth of the transmitting/receiving antennas due to large operating frequency enables one to achieve large link budgets for LOS communications. Link budget which is defined as the total received power and is given in terms of the total transmitted power, antenna gain and losses in the system. Due to the small beamwidth of the antenna, the overall gain of the antenna will be higher, and losses will be lower, resulting in a larger link budget. This also reduces interference from adjacent antennas and communication links due to receiver's small beamwidth, leading to a smaller co-channel interference. Several studies have been conducted for understanding the 60-GHz propagation channel in the last few decades [29]-[38]. However, previous studies related to indoor propagation at 60 GHz [29]-[32] are mainly focused on the statistical parameters and models. Several research studies have also been performed to understand the influence of system parameters [39], [40] human activity [19], [28], [41] and materials [42], [43] on channel properties and transmission losses. Furthermore, we can find studies comparing the 60-GHz channel characteristics with lower bands [29], [44]. Researchers in [44]-[46] have also studied the application of the Saleh–Valenzuela model in the 60-GHz frequency band. However, similar to the previous mobile communication channels, the 60-GHz indoor radio channel is also a multipath propagation channel [29], [47]. The systems being designed to operate into the mm-wave frequency bands consist of a combination of cost-effective CMOS technology, high-gain, steerable antennas at the mobile and base station [25], [26]. The increase in the RF channel bandwidth directly translates into an increase in the data rate and a decrease in the transmission latency, thus making possible the applications which require high data speed and minimal latency. Also, due to the small wavelength of the mm-wave frequencies, several new polarization and spatial process techniques such as massive MIMO, cooperative MIMO, relays, adaptive beamforming and interference mitigation between base stations become more feasible [27]. The implementation of these techniques also leads to a reduction in the cost per base station and will make easier implementation of wireless backhaul for flexibility. Finally, the current spectrum employed by the cellular operators is very disjointed, expanding over frequencies between 700 MHz and 2.6 GHz, which leads to a wide variation in the coverage distance of cell sites. The mm-wave spectrum occupies a large band of frequencies ranging from 52 GHz to 71 GHz, which consists of channels that are placed close to each other (33%), making the propagations characteristics in different channels comparable and homogenous.

Further, the 28 GHz and 38 GHz bands are also being reviewed for spectrum allocations which increases the range of the mm-wave channels [29].

### 1.5 Limitations of mm-wave

The major concern of the wireless community regarding the implementation of mm-wave is the attenuation due to rain and atmosphere which the signal at high frequencies faces. However, work done by many researchers has confirmed that, for small distances (less than 1 km), rain attenuation will present a minimal effect on the propagation of mm-waves at 28 GHz to 38 GHz for small cells [29], [41], [48]. But as the frequency increases (at 60 GHz) the rain attenuation also increases. However, it is still possible to overcome the attenuation with the implementation of smaller cells, and, therefore, mm-wave communications will definitely be an essential part of 5G and other future cellular generations [1]-[7].

The transmission of mm-wave signals poses certain other challenges as well for wireless communications. Signals at lower frequencies can easily pass-through wooden objects such as walls and furniture and, therefore, can cover indoor environment. However, mm-waves can only travel for short line-of-sight distances due to the path-loss and can easily get obstructed from the wooden/concrete/glass buildings and other constructions. These seemingly apparent limitations can be utilized to limit their transmission, thereby resulting in a reliable and secure communication system, which will be more protected from the network security intrusions. Another advantage to come out of the mm-wave limitations is their utilization in facilitating small-cell networks, increasing frequency reuse, therefore leading to efficient spectrum utilization. The principal factors which contribute to the limitations of mm-waves can be characterized as (a) free space path loss, (b) propagation loss factors such as reflection, diffraction, scattering, atmospheric gaseous losses, precipitation attenuation due to rain, and lastly foliage losses.

### 1.6 Limitations of Indoor use of mm-wave

There have been several studies conducted in the recent past and several new measurement campaigns going on with the aim of characterizing and modeling the mm-wave propagation channel (see [1]-[15], [20]-[27], [49], [50]). Most of these measurements being done are constricted by the different experimental factors governed by the modeling technique used and system-level evaluations performed. For example, in an indoor environment, the main factor limiting the signal propagation can be obstruction due to physical wooden or metallic objects, presence of the humans causing extra attenuations, also the movement of humans or objects with respect to both the user device and the access point [16]-[19], [28]-[47], [51], [52].

In indoor propagation, the total signal attenuation comprises of path loss, static fading and multipath fading. Path loss takes place due to the decrease in the signal level as it travels a certain distance for both line-of-sight (LoS) and non-line-of-sight (NLoS) configurations. Static fading happens on account of partial or complete obstruction of the signal due to static (furniture or construction), multipath fading takes place due to the mobile objects (human movement) present in the signal path which lead to spatial and temporal fading effects. However, the biggest hurdle in implementation of indoor mm-wave systems is the obstruction of line-of-sight signal. Due to the quasi-optical nature of the mm-wave signals, it results in minimal transmission and diffraction of the signal. However, the benefit is a fraction of the shortcoming posed by the obstruction of mm-wave signals by the different obstructions usually present in the indoor environment. To give an account, the wooden walls and doors pose an attenuation of 20 dB, glass leads to an attenuation of 15 dB, human bodies account for insurmountable 35 dB of attenuation [41]. The typical values of path loss exponents (PLEs) in indoor line-of-sight (LOS) environments vary by the structure of the construction, such that for symmetrical hallways, it is 1.3, for a medium size room, PLE is 1.7 and for a larger office room, PLE is recorded to be 2.2. For non-line-of-sight (NLOS) environments, larger PLEs were reported, that vary between 3.0 to 3.8 in a typical office space. There is some difference between the average RMS delay spreads recorded for LOS and NLOS environments which is 12.3 ns and 14.6 ns at 60 GHz, respectively [21].

The main concern about mm-wave frequency bands is that the signals at such high frequencies undergo a greater propagation loss (e.g., for a distance of 5 m at 2.45 GHz, the propagation loss is 40.20 dB, considering similar antenna gain, at 60 GHz, the propagation loss is 68 dB), and thus cannot be transmitted over large distances. However, even in indoor communication setting, mm-wave encounters several problems. Unlike lower frequency signals, mm-wave signals have extremely small wavelength and can be severely attenuated by physical barriers, such as walls, doors, and other commonly used objects in an indoor environment. This implies that mm-wave communications might be limited to an area where direct line of sight is present, such as a single room in the house. Subsequently, in order to provide coverage for an entire building, each room must be equipped with a wireless router. This is an expensive proposition as compared to below 6 GHz ISM band devices, which require a single router for a typical home or office.

With the rapid growth in technology, the demand for high data rates has increased exponentially which paved the way for an increased interest in millimeter-wave (mm-wave) bands, including 60 GHz band. However, there are several issues with the use of mm-wave signals, which should be addressed in order to make the optimum use of the available bandwidth in the mm-wave channels. The most concerning issue is the large propagation loss which the signals suffer and get severely attenuated by physical barriers, such as walls, doors, etc. in the indoor environment at mm-wave frequencies. Therefore, the transmission of mm-wave signals is limited to line-of-sight (LOS) communication scenario due to the barriers present in an indoor communication, essentially even restricting the coverage to within a room in the house.

## 1.7 Proposed system to distribute mm-wave in indoor scenario

There are several ways in which internet can be made accessible inside an indoor communication scenario. Using the current technologies high-data rate connection can be provided by Ethernet lines, fiber optics and Wifi. However, with the increase in demand of higher data rate and a greater number of users sharing the services, the mm-wave option is being considered. Use of the mm-wave signals in case of indoor communication would result in replacement of all the currently deployed connecting technologies, which may be a costly option. Further it's also not feasible given the small wavelength of mm-wave signals. Therefore, even though the wireless communication has been the standard mode of transmission using the latest technologies but the design of a wireless network in large buildings with the expected data rate through the use of mm-wave is still a complicated task due to the nature of indoor propagation [53], [54]. Therefore, there is a need to find alternate solutions possibly in form of the existing infrastructures that can be utilized for data communications.

To utilize the millimeter wave frequency band, the fundamental knowledge of the mm-wave channel propagation characteristics, including accurate and reliable channel models, is of vital importance for developing indoor 5G wireless communication systems. Several researchers (for example, see [3]-[6], [14]-[28], [47], [50]) have extensively studied the characteristics of a traditional indoor radio propagation channel and the use of optical fibers. Indoor channel performance strongly depends on the specifics of the environment such as the number of obstructions and static/mobile objects in the environment. In a typical office environment, the signal level decays (in dB) as the product of distance and power loss factor whose value depends on the environment (typically, this value is between two and four). Therefore, the delay spread increases with the distance from the transmitter and can vary between a few tens to a few hundreds of nanoseconds as shown in [36] and [55]. In mm-wave systems operating indoors, even though the signal's beam is somewhat narrow, the presence of multipath is unavoidable. The use of multiple directional antennas configurations has been discussed in [36], [56] in order to mitigate the effects of multipath in indoor communication using mm-wave. Other approaches have demonstrated high speed mm-wave over short ranges [55]. In [57], authors use the concept of relay nodes to mitigate the free-space path loss (FSPL) and multipath in order to provide indoor communications using mm-wave. Furthermore, the 60 GHz channel has been studied extensively in literature, for example see [11]-[56]. The use of relay nodes and directional antennas provides reliable communication for a wider coverage area but determining the exact position of the relay nodes based on the transmitter and receiver location and the extra installation cost is the drawback of the above-mentioned techniques.

This implies that mm-wave communication will be limited to an area where direct line of sight or significant multipath link can be supported (a room in the house). Subsequently, in order to provide coverage for the entire building, each room must be equipped with a router. This is an expensive proposition as compared to below 6 GHz ISM band devices, which require a single router for a typical home or office. One solution that can be considered is to distribute mm-wave signals around the building using waveguides. However, given that coaxial cables must be replaced with mm-wave waveguides at 60 GHz (often quite expensive) this solution becomes impractical and costly. Hence, to leverage the presence of a proven RF waveguide in homes and offices becomes of some interest. One communication channel that is already present in most structures is the HVAC duct system.

This chapter describes a new methodology for transmission of mm-wave signals to the users inside a residential or commercial building through the use of heating, ventilation, and air conditioning (HVAC) duct system. The system includes a transceiver device for introducing electromagnetic radiation into the duct system such that the HVAC duct acts as a waveguide for the mm-wave signals in form of electromagnetic radiation. The system also includes devices such as antennas, reflectors, power amplifiers and relays in order to transmit the signal from the duct system to the receiver. The heating, ventilation, and air conditioning (HVAC) duct system consists of rectangular or cylindrical metal pipes which are interconnected to each other in order to provide the heating and cooling services inside any residential and commercial building in most parts of the world. However, due to their metallic and symmetrical construction, these ducts act as waveguides when used as a channel for the transmission of mm-wave signals. The HVAC system in itself is a complex network of different subsections which all act as a complex mesh of waveguides, through which multiple electromagnetic modes can propagate depending on the frequency of operation, the dimension and structure of the HVAC duct and the various nonuniformities (bends, tapers, T-junctions, etc.) present as a part of the HVAC duct system. This waveguide channel can therefore be considered as a potential reliable communication medium through which extremely high-data rate communication is possible [58].

The use of HVAC ducts as a communication channel has already been studied in the past, as can be seen in [56], [59]-[71] and the references in [59], for RF signal distribution for frequencies below 6 GHz. Unlike such previous work, where the input dimensions of HVAC ducts are comparable with the wavelength of the signal in a lower frequency ISM band, the same HVAC ducts will be considered significantly large in dimension as compared to the signal wavelength at 60 GHz. Furthermore, most RF signals can penetrate residential structure, whereas at mm-wave frequencies, the signal is severely attenuated by physical barriers. Hence, it is of interest to investigate this mode of communication for the distribution of mm-wave signals. HVAC ducts are hollow cylindrical or square metal pipes that penetrate all building floors and present a reliable channel whose performance is not impacted by time-varying factors such as movement of people or arrangement of furniture. These ducts can act as large waveguides for mm-wave signals, as the signals will be travelling along the length of the duct (waveguide) suffering no attenuation from the physical barriers and minimal loss at the bends, leading to many folds increase in the coverage area and providing non-line of sight communications. Hence, HVAC has the potential to allow one to harness the advantages of using mm-wave communications, such as large bandwidths and higher data rates in sizeable infrastructures.

### 1.8 Advantages of HVAC Ducts

The HVAC duct systems consist of metal pipes of rectangular or circular cross-section through which the air with temperature and moisture is flowing through it and these systems penetrate all the building floors. It presents as a reliable time-invariant channel whose performance is not impacted by time-varying factors such as movement of people or arrangement of furniture. This is due to large free-space path loss as well as oxygen loss at this band. However, when used with HVAC ducts, mm-wave signals will be travelling along the length of the duct (waveguide), suffering no attenuation from the physical barriers and minimal loss at the bends. This will result in small path-loss, leading to many folds increase in the coverage area and providing non-line of sight communications. As the ducts are already present in most residential and commercial buildings, it saves expense incurred in laying the extensive fiber network. Also, the metal waveguides are very well shielded from any external electrical disruptions in the indoor environment. Therefore, the mm-waves can easily propagate through the HVAC duct without any significant path loss and provide extremely high data rate. Another great advantage of the HVAC duct is that they continue to carry the mm-wave signals even though the duct system suffers damage in certain parts, therefore they are robust to damage. Finally, considering the different emittance and interference regulations (base station transmitted power level should be limited to 75 dBm/100 MHz and for a mobile phone, transmitted power should be limited to 43 dBm) , different mm-wave channels consisting of different frequencies and powers can simultaneously be transmitted through the HVAC duct channel without violating any of the regulations. Hence, HVAC has the potential to serve as an independent transmission medium, allowing one to harness the advantages of using mm-wave communications, such as large bandwidths and higher data rates (up to 2 Gbps) in sizeable infrastructures.

# CHAPTER 2

# HVAC DUCT SYSTEM

## 2.1 Why HVAC Duct?

The ubiquitous presence of HVAC ducts in the residential and the commercial buildings, makes it logical to utilize the HVAC ducts as the new transmission channel in the indoor wireless communication scenario. In order to alleviate the use of wires, cables and routers to carry the various signals, HVAC ducts make an extremely promising case for their use. Installation, replacement and upgradation of the fibers and coaxial cables prove to be an expensive alternative compared to the already present HVAC ducts inside a building. Further, with the upgradation of the technology (moving from one generation to another i.e., 5G to 6G etc.), irrespective of the frequency and the power of the signal, HVAC ducts can always be used to transmit the signal as they are made up of metals and thereby behave as huge waveguides.

In case of indoor wireless communication, the signals are transmitted and received through a multitude of transceivers and antennas. These devices are placed at locations which are easily intercepted in order for the signal to reach the different user equipment. However, finding the optimum location for the transceivers so that the signal is received by the transceivers, or the signal strength is not diminished beyond reception can be a challenging task with mm-wave signals.  Finding the optimum position of the transceivers becomes more complex when mobile receivers, such as mobile phones, laptops, and the movement of humans is integrated into the communication systems.

In scenarios where experiments fail, we resort to methods such as ray-tracing which uses geometrical optics in order to predict the location of the transceivers and thereby indoor radio coverage. Other methods such as statistical channel modeling can also be used to characterize the general indoor channel by determining a fixed set of channel parameters. As these methods take only general geometrical aspect into consideration, the results are sub-optimum and inefficient communication systems are implemented. However, these methods still worked in past with the large wavelength of ISM band. However, as the mm-wave can get obstructed much more easily, it will be impossible to predict the optimum location of the transceivers for a wider indoor coverage. Moreover, the propagation of the signals can be affected due to the change in the position of a metallic or wooden object present in that room. Hence, in order to efficiently transmit and receive the mm-wave signals, we need a method and system that will prevent the obstruction of the signals from the object without having to design an elaborate system or incurring a large installation or re-installation cost.

## 2.2 Introduction to HVAC Duct System

In this chapter, we introduce the HVAC ducts system model that can be used as a potential communication channel for transmitting mm-wave signals to the users inside residential and commercial buildings. The HVAC duct system consists of hollow metal pipes which have rectangular or circular cross-section and are interconnected to form a multimode waveguide for the RF signals passing through them. The number of modes which will propagate through these multimode waveguides will eventually be determined by the dimension of the HVAC ducts, and by the various other nonuniformities such as bends, tapers, T-junctions, etc. The standard duct used in the U.S. is of cylindrical cross-section with a diameter of 5 inches or 12 inches and a cutoff frequency of 1.38 GHz and 577 MHz respectively as shown in Figure 2.1. Currently, the mm-wave/WiGig standard comprises of frequencies which are allocated for unlicensed use and the spectrum ranges from 52 GHz to 71 GHz, clearly the frequency range is above the aforementioned cutoff. The HVAC system relies on the key observation that they are present in most parts of the USA and are made up of metal which makes them behave as waveguides suitable for all forms of wireless transmission.


Figure 2.1. Typical HVAC duct used in the United States

The HVAC duct system, like any other typical communication system includes a transceiver device which will introduce the mm-wave signals into the HVAC duct which acts as a waveguide for electromagnetic signals due to its metallic construction. The system also includes devices such as antennas, relays, power amplifiers which introduce and facilitate the propagation of the electromagnetic signals through the entire length of the duct, and further distributed to the users.

For the downlink, mm-wave signal is sent from a base station [72]. The signal propagates through the HVAC duct which behaves as the propagation channel and is captured by the antenna present near the HVAC duct opening in different rooms. This antenna then transmits the signal to the different users present in each room, reducing the amount of obstruction of the signal and the path loss suffered by it. A channel access algorithm can be used to distribute the downlink signal among multiple receiving users [51], [73], [74]. In the uplink, the mm-wave signal is transmitted by a laptop, handset, or other end-user's transceivers to the passive antenna present in each room. The signal is then sent through the HVAC for reception by the base station.

An example of an HVAC system used for signal distribution is shown in Figure 2.2. The antenna present on the mm-wave access point excites the electromagnetic modes in the waveguide duct system. These modes which have different group velocities and attenuation constants, take different paths while traversing through the duct system, experiencing multiple reflections from the non-smooth edges and other non-uniformities before reception by the antenna present in the room where the intended users are present [39], [75]. Users can access the system directly from the antenna. In order to maintain the power level through the duct system, a relay can be used. Amplify and forward relays amplify the signal and retransmit it on a symbol or packet basis [12], [48], [50]. Furthermore, after reaching different rooms the signal can be distributed between the users via passive repeaters such as reflect arrays, transmit arrays [40], [52].

The HVAC channel also behaves like a linear channel and therefore can be defined in terms of its impulse response (or transfer function).

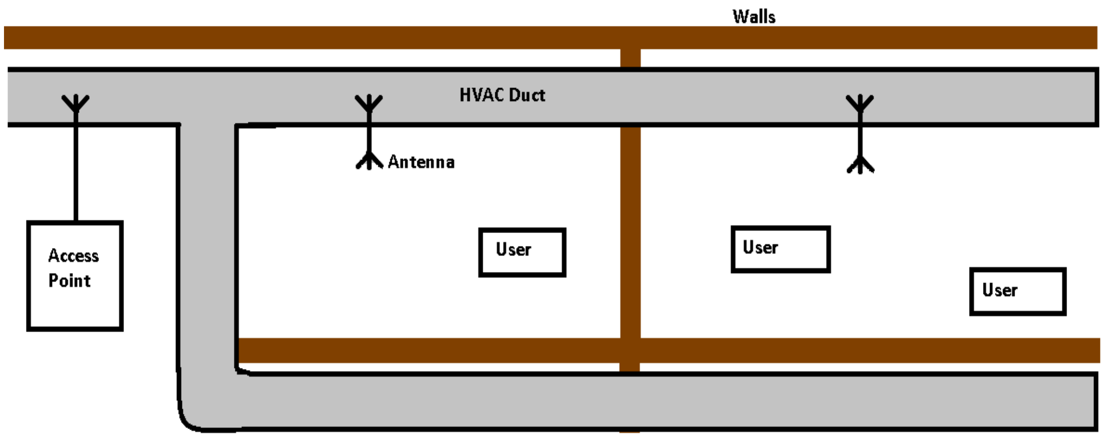


Figure 2.2. An example of proposed HVAC duct system

## 2.3 Example of an Application of HVAC Duct System

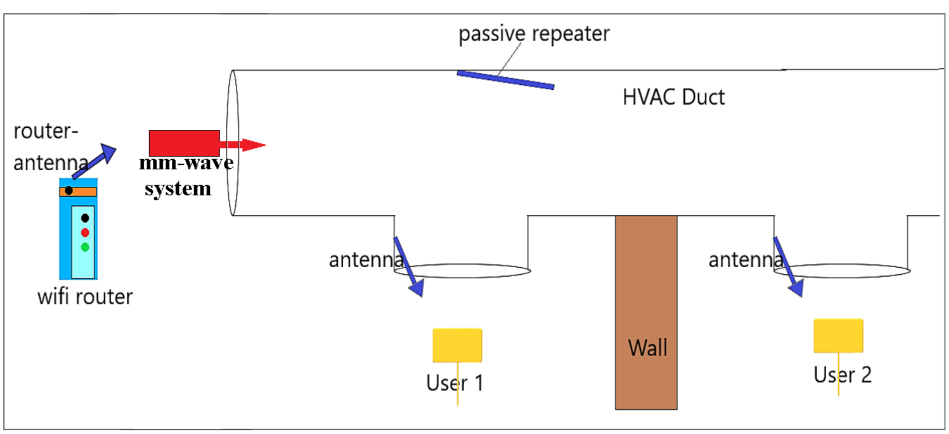


Figure 2.3. High level architecture of Wifi system propagation through HVAC duct

# CHAPTER 3

# HVAC MODES AND THEIR POWER

## 3.1 Waveguides

For the transmission of electromagnetic signals efficiently, the transmission and reception terminal can be connected through a waveguide, especially where direct line of sight communication is not possible. Some common types of guiding structures are coaxial cable, microstrip transmission lines, hollow conducting waveguides, and optical fibers as described in Table 3.1. Depending upon the frequency of operation, the amount of power that is being transferred and the permissible losses, the appropriate waveguide structure is selected.

Table 3.1. Common guiding structures for communication systems

| | |
|---|---|
| Coaxial cables | • Used at frequency < 3 GHz.<br>• High losses.<br>• Low power rating with increased frequency.<br>• Heating of the conductor and dielectric. |
| Two wire lines | • Used at microwave frequencies.<br>• Not shielded and can radiate. |
| Microstrip lines | • Used at microwave frequencies. |
| Rectangular waveguides | • Used at frequencies > 3 GHz. |
| Optical Fiber | • Used at optical and infrared frequencies.<br>• Provide wider bandwidth.<br>• Lead to low losses. |

### 3.2 Solution of Maxwell's Equations for Waveguides

For a waveguide system, Maxwell's equations are used to find the solution of electromagnetic fields that will be propagating along the length (the z direction) of the waveguide. Therefore, the electric and magnetic fields can be defined as [76]:

$$E(x, y, z, t) = E(x, y)e^{j\omega t - j\beta z}$$
$$H(x, y, z, t) = H(x, y)e^{j\omega t - j\beta z} \tag{3.1}$$

where $\beta$ is the propagation wavenumber. Due to the waveguide structure, the signal travelling through it will have a different wavelength than the free space. This wavelength is known as the guide wavelength $\lambda_g = 2\pi/\beta$. The waveguide dimensions and its cross-section (cylindrical or rectangular) will also determine the relationship between $\omega$ and $\beta$ and the modes which will be allowed to propagate. These fields vary in the transverse directions (the $x, y$ directions,) and therefore, can be decomposed into transverse $(x, y)$ and longitudinal $z$-directions. Thus, we decompose:

$$E(x, y) = \hat{x}E_x(x, y) + \hat{y}E_y(x, y) + \hat{z}E_z(x, y) \tag{3.2}$$
$$= E_T(x, y) + \hat{z}E_z(x, y)$$

Using the vectoral identities, the source-free Maxwell's equations can be written as [76]:

$$
\begin{aligned}
\nabla_T E_z \times \hat{z} - j\beta \hat{z} \times E_T &= -j\omega\mu H_T \\
\nabla_T H_z \times \hat{z} - j\beta \hat{z} \times H_T &= j\omega\epsilon E_T \\
\nabla_T \times E_T + j\omega\mu \hat{z} H_z &= 0 \\
\nabla_T \times H_T - j\omega\epsilon \hat{z} E_z &= 0 \\
\nabla_T . E_T - j\beta E_z &= 0 \\
\nabla_T . H_T - j\beta H_z &= 0
\end{aligned}
\tag{3.3}
$$

Based on the value of the longitudinal components, we can classify the solutions as transverse electric and magnetic (TEM), transverse electric (TE), transverse magnetic (TM), or hybrid:

$E_z = 0, H_z = 0$, TEM Modes

$E_z = 0, H_z \neq 0$, TE Modes

$E_z \neq 0, H_z = 0$, TM Modes

$E_z \neq 0, H_z \neq 0$, hybrid or HE or EH Modes

The first two equations form a linear system in the two unknowns $\hat{z} \times E_T$ and $H_T$, and their solution is [76]:

$$
\begin{aligned}
\hat{z} \times E_T &= -\frac{j\beta}{k_c^2} \hat{z} \times \nabla_T E_z - \frac{j\omega\mu}{k_c^2} \nabla_T H_z \\
H_T &= -\frac{j\omega\epsilon}{k_c^2} \hat{z} \times \nabla_T E_z - \frac{j\beta}{k_c^2} \nabla_T H_z
\end{aligned}
\tag{3.4}
$$

where the cutoff wavenumber $k_c$ is given by:

$$k_c^2 = \omega^2 \epsilon\mu - \beta^2 = \frac{\omega^2}{c^2} - \beta^2 = k^2 - \beta^2 \tag{3.5}$$

The quantity $k = \omega/c = \omega\sqrt{\epsilon\mu}$ is the wavenumber for a uniform plane wave travelling in a medium with relative permittivity $\epsilon$ and permeability $\mu$. Using above definitions, we can also define the cutoff frequency as: $\omega_c = ck_c$. Considering the wavelength: $\lambda = 2\pi/k = 2\pi c/\omega$, $\lambda_c = 2\pi/k_c$, and $\lambda_g = 2\pi/\beta$. It follows from $k^2 = k_c^2 + \beta^2$ that

$$\frac{1}{\lambda^2} = \frac{1}{\lambda_c^2} + \frac{1}{\lambda_g^2} \rightarrow \lambda_g = \frac{\lambda}{\sqrt{1 - \lambda^2/\lambda_c^2}} \tag{3.6}$$

Also, the free space wavelength is given as $\lambda_0 = 2\pi c/\omega = c/f$ and the wavelength in a dielectric material of refractive index $n$ is given by $\lambda = \lambda_0/n$.

The transverse impedances for the TE and TM modes can be defined by the definitions [64]:

$$\begin{aligned} \eta_{TE} &= \frac{\omega\mu}{\beta} = \eta\frac{\omega}{\beta c} = \frac{\eta}{\sqrt{1 - \frac{\omega_c^2}{\omega^2}}}, \\ \eta_{TM} &= \frac{\beta}{\omega\epsilon} = \eta\frac{\beta c}{\omega} = \eta\sqrt{1 - \omega_c^2/\omega^2} \end{aligned} \tag{3.7}$$

where $\beta c/\omega = \sqrt{1 - \omega_c^2/\omega^2}$ and the medium impedance is $\eta = \sqrt{\mu/\epsilon}$, so that $\eta/c = \mu$ and $\eta c = 1/\epsilon$. With these definitions, we may rewrite the Maxwell's equations as follows [76]:

$$H_T - \frac{1}{\eta_{TM}}\hat{z} \times E_T = \frac{j}{\beta}\nabla_T H_z$$

$$E_T - \eta_{TE} H_T \times \hat{z} = \frac{j}{\beta}\nabla_T E_z$$

$$\nabla_T \times E_T + j\omega\mu\hat{z}H_z = \frac{j\omega\mu}{k_c^2}\hat{z}(\nabla_T^2 H_z + k_c^2 H_z)$$

$$\nabla_T \times H_T + j\omega\epsilon\hat{z}E_z = -\frac{j\omega\epsilon}{k_c^2}\hat{z}(\nabla_T^2 E_z + k_c^2 E_z) \tag{3.8}$$

$$\nabla_T . E_T - j\beta E_z = -\frac{j\beta}{k_c^2}(\nabla_T^2 E_z + k_c^2 E_z)$$

$$\nabla_T . H_T - j\beta H_z = -\frac{j\beta}{k_c^2}(\nabla_T^2 H_z + k_c^2 H_z)$$

Where $\nabla_T^2$ is the two-dimensional Laplacian operator. The right-hand side of the last four equations in (3.8) require the equivalence of the Helmholtz equations by the longitudinal fields $E_z(x, y), H_z(x, y)$ as follows:

$$\nabla_T^2 E_z + k_c^2 E_z = 0 \tag{3.9}$$

$$\nabla_T^2 H_z + k_c^2 H_z = 0$$

Further the boundary conditions depending on the waveguide type must also be satisfied. After calculating the fields $E_z, H_z$, the transverse fields $E_T, H_T$ can be computed. Result of all the six equations in (3.8) represent the maxwell's equation solution for the waveguide structure.

**Cartesian coordinates**

Using the identity $\hat{z} \times \nabla_T H_z = \hat{y}\partial_x H_z - \hat{x}\partial_y H_z$, we obtain the longitudinal components [76]:

$$\left(\partial_x^2 + \partial_y^2\right)E_z + k_c^2 E_z = 0 \tag{3.10}$$

$$\left(\partial_x^2 + \partial_y^2\right)H_z + k_c^2 H_z = 0$$

and resulting transverse components:

$$E_x = -\frac{j\beta}{k_c^2}\left(\partial_x E_z + \eta_{TE}\partial_y H_z\right)$$

$$E_y = -\frac{j\beta}{k_c^2}\left(\partial_y E_z + \eta_{TE}\partial_x H_z\right)$$

$$H_x = -\frac{j\beta}{k_c^2}\left(\partial_x H_z - \frac{1}{\eta_{TM}}\partial_y E_z\right) \tag{3.11}$$

$$H_y = -\frac{j\beta}{k_c^2}\left(\partial_y H_z + \frac{1}{\eta_{TM}}\partial_x E_z\right)$$

3.2.1 Overview of TEM, TE, and TM mode

The general solution will have nonzero $E_z$ and $H_z$ components representing a hybrid combination of electrical and magnetics components. However, the transverse fields $E_T, H_T$ are always perpendicular to each other and satisfy: $H_T = \frac{1}{\eta_T}\hat{z} \times E_T$ where the transverse impedance

$\eta_T$ varies according to the different mode types such as $\eta$ for TEM, $\eta_{TE}$ and $\eta_{TM}$ for TE and TM cases respectively. The Poynting vector $P_z$ described in terms of the mode transverse impedance shows the total power through a unit cross-sectional area and is given by:

$$P_z = \frac{1}{2} Re(E_T \times H_T^*).\hat{z} = \frac{1}{2\eta_T} |E_T|^2 = \frac{1}{2} \eta_T |H_T|^2 \tag{3.12}$$

3.2.2 TEM mode

In TEM modes, $E_z = H_z = 0$ and the fields are fully transverse, therefore, $k_c^2 = 0, or\ \omega = \beta c$, which further implies $\eta_{TE} = \eta_{TM} = \eta$. The electric field $E_T$ is determined as: $\nabla_T \times E_T = 0$ and $\nabla_T . E_T = 0$.

3.2.3 TE mode

For the TE mode, only the transverse electric field will be equal to zero, therefore, $E_z = 0$ and $H_z \neq 0$. From Maxwell's equations, $E_T = \eta_{TE} H_T \times \hat{z}$. The wave impedance is now $\eta_{TE}$. The field components and Poynting vector for TE mode are given as follows [76]:

$$\begin{gathered} \nabla_T^2 H_z + k_c^2 H_z = 0 \\ H_T = -\frac{j\beta}{k_c^2} \nabla_T H_z \\ E_T = \eta_{TE} \hat{z} \times H_T \end{gathered} \tag{3.13}$$

$$P_z = \frac{1}{2}Re(E_T \times H_T^*).\hat{z} = \frac{1}{2\eta_{TE}}|E_T|^2 = \frac{1}{2}\eta_{TE}|H_T|^2 = \frac{1}{2}\eta_{TE}\frac{\beta^2}{k_c^4}|\nabla_T H_z|^2$$

The cartesian coordinate version is:

$$\begin{gathered}
\left(\partial_x^2 + \partial_y^2\right)H_z + k_c^2 H_z = 0 \\
H_x = -\frac{j\beta}{k_c^2}\partial_x H_z, H_y = -\frac{j\beta}{k_c^2}\partial_y H_z \\
E_x = \eta_{TE} H_y, \qquad E_y = -\eta_{TE} H_x
\end{gathered} \tag{3.14}$$

3.2.4 TM mode

TM modes have $H_z = 0$ and $E_z \neq 0$. From the Maxwell's equations, $H_T = \eta_{TM}^{-1}\hat{z} \times E_T$. The wave impedance is now $\eta_{TM}$. The field components and the pointing vector equations for the TM mode are similar to the TE mode equations and are given as [76]:

$$\begin{gathered}
\nabla_T^2 E_z + k_c^2 E_z = 0 \\
E_T = -\frac{j\beta}{k_c^2}\nabla_T E_z \\
H_T = \frac{1}{\eta_{TM}}\hat{z} \times E_T \\
P_z = \frac{1}{2}Re(E_T \times H_T^*).\hat{z} = \frac{1}{2\eta_{TM}}|E_T|^2 = \frac{1}{2\eta_{TM}}\frac{\beta^2}{k_c^4}|\nabla_T E_z|^2
\end{gathered} \tag{3.15}$$

From the above discussion, we can infer that for the transmission of the electromagnetic energy, waveguides can be carefully designed to support the selected number of modes propagating through them. However, with the advent of technology, structures like tunnels [77] and underground mines, and lift shafts, radio frequency identification (RFID) systems operating inside marine structures and HVAC ducts are considered as waveguiding structures and used as propagation communication medium. In contrast with the carefully designed waveguides, these structures, which are not designed to be RF waveguides in practice, behave as highly over-moded waveguides. Therefore, in order to model the HVAC duct channel, it is useful to know the number of propagating modes.

### 3.3 Comparison between HVAC Duct and Free Space

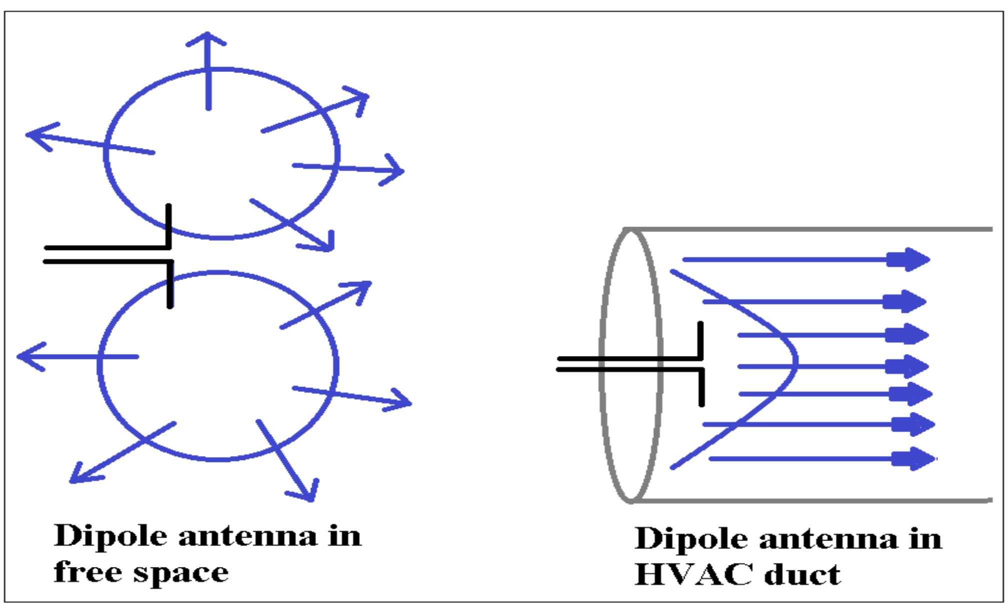

Figure 3.1. Comparison of radiation by dipole antenna in free space and HVAC

There are significant differences between the mm-wave signal radiated in free-space through an antenna and the signal being transmitted through the HVAC duct serving as the waveguide communication channel [62]. The main differences between this environment and free-space are as given in Fig 3.1 and Table 3.2.

Table 3.2. Comparison between free-space and HVAC duct channel

| Free Space | HVAC Duct |
|---|---|
| Waves can propagate in any direction. | Waves propagate only along the length. |
| Continuous mode distribution. | $N$ discrete modes. |
| The propagating field is a sum of rays transmitted through the free space. | The propagating field is a sum of all the normal modes. |
| Can be analyzed using geometrical optics such as ray-tracing. | Can be analyzed using modal theory. |
| Antennas used can be characterized by their directive gain. | HVAC duct as a waveguide can be characterized by its mode sensitivity gain. |
| Directivity $D \leq \infty$. | Sensitivity $S \leq N$ (number of modes). |

### 3.4 Rectangular Waveguide

Consider a rectangular waveguide with length and breadth dimensions as $a$ (wide) and $b$ (narrow). For this waveguide, the mode cutoff frequencies can be given as [67]:

$$f_c^{rect} = \frac{c}{2}\sqrt{\left(\frac{m}{a}\right)^2 + \left(\frac{n}{b}\right)^2} \tag{3.16}$$

where for TE modes either $m$ or $n$ must be positive, and for TM modes both $m$ and $n$ must be positive. The modes whose cutoff frequencies are below the operating frequency $f$ will be excited ($f_c^{rect} \leq f$).

### 3.5 Circular Waveguide

To calculate the number of modes propagating in an HVAC duct of circular cross-section of radius $R$, the mode cutoff frequencies for transverse electric (TE) and transverse magnetic (TM) modes are given as follows [66]:

$$f_c^{circ} = \frac{c}{2\pi R}\begin{cases} p'_{mn} & ,TE \\ p_{mn} & ,TM \end{cases} \tag{3.17}$$

where $p'_{mn}\ and\ p_{mn}$ are the $m^{th}$ nulls of $J'_n(x)\ and\ J_n(x)$, respectively, with $J_n(x)$ denoting the Bessel function of the first kind of order $n$. Furthermore, $c$ denotes the speed of light.

Table 3.3 below gives the number of modes that can propagate in the duct of various dimensions at 60 GHz. However, not all the modes are significant in this scenario.

Table 3.3. Number of modes propagating in HVAC duct

| Duct | Diameter | # Modes at 58.5 GHz | #Modes at 60 GHz | #Modes at 62.5 GHz |
|---|---|---|---|---|
| Cylindrical | 12.7 cm | 1506 | 1576 | 1712 |
| Cylindrical | 30.5 cm | 8622 | 9071 | 9832 |
| Rectangular | 12.7 cm x 6 cm | 17936 | 18858 | 20466 |
| Rectangular | 30.5 cm x 15 cm | 10752 | 11308 | 12294 |

The power carried by each mode is directly proportional to the mode radiation resistance and is given as [78]:

$$p_u = \frac{R_u}{\sum_{u=1}^{N} R_u} \tag{3.18}$$

where $R_u$ is the mode radiation resistance [78] and $N$ is the total number of propagating modes.

### 3.6 Sensitivity Gain

The directive gain is equivalent to mode sensitivity gain in case of waveguides, as the propagating field can be expressed as a finite sum of normal modes. The electromagnetic radiation modes which have the maximum effect on the received signal, determine the mode sensitivity for the receiving antenna and directly govern the reception quality of the communication system. Sensitivity can be defined as [78]:

$$S = \max S(n) \tag{3.19}$$

where mode sensitivity gain is

$$S(n) = \frac{P(n)}{P/N} \tag{3.20}$$

with $P(n)$ denoting the power radiated into mode $n$, normalized by the total radiated power $P/N$, and the number of modes $N$, respectively. Antennas are used to couple, transmit and receive the signal through the HVAC duct waveguide. In free space, an antenna is characterized by the far-field radiation pattern, however, in waveguides, the mode distribution excited by the antenna is used to characterize the antenna. The coupling is determined by the antenna impedance; therefore, it is important to determine both antenna impedance and the excited mode distribution.

### 3.7 Antenna impedance and current distribution

The impedance $Z_a$ of a general antenna is given in terms of its resistance $R_a$ and its reactance $X_a$, as $Z_a = R_a + jX_a$. For a multimode waveguide, the different modes can be thought of as being produced due to the interaction of the electromagnetic energy with several independent loads. Therefore, the antenna is viewed as a series network of these independent loads, with each load resulting in the generation of a specific mode [61].

The load impedance results because of the presence of the antenna current and its interaction with electric field. Therefore, the total antenna impedance $Z_a$ is a summation of the radiation resistance $R_u$ of mode $u$ and the radiation reactance $X_u$ of the mode $u$ for the antenna, $Z_a = \sum_{u=1}^{U} R_u + j \sum_{u=1}^{U} X_u$. The radiation resistance $R_u$ is calculated in terms of the power associated with mode $u$. Assuming that the mode $u$ carries power $P_u$ , then the total power carried by mode $u$ can be expressed as

$$\frac{1}{2} I_0^2 R_u = 2P_u = 2p_u |C_u|^2 \tag{3.21}$$

The mode radiation resistance $R_u$ can be defined using the definition of interaction integral $I_u$ and normalized power density $p_u$ as $R_u = |I_u|^2/4p_u$. As the HVAC duct is a practical structure which was not designed specifically for wireless communication purpose, therefore, the communication through it can suffer attenuation due to non-ideal conducting metal walls. Attenuation due to the metallic wall resistance $R_s$ can be defined as [63]:

$$R_s = \sqrt{\frac{\omega\mu}{2\sigma}} \tag{3.22}$$

Where $\mu$ is the magnetic permeability of the waveguide walls, and $\sigma$ is the electrical conductivity of the walls. The wave number $k$ is:

$$\beta = \sqrt{k^2 - g^2} \tag{3.23}$$

Where $g$ is the cutoff wave number and $k$ is the free-space wave number. The free-space wave number can be expressed as

$$k = \frac{\omega}{c} = \frac{2\pi}{\lambda} \tag{3.24}$$

Where $c$ is the speed of light and $\lambda$ is the free-space wavelength. The mode cutoff frequency $\omega_c$ is given by

$$\omega_c = cg \tag{3.25}$$

3.7.1 Rectangular Waveguide Parameters

The cutoff wave number is given by

$$g = \sqrt{\left(\frac{m\pi}{a}\right)^2 + \left(\frac{n\pi}{b}\right)^2} \tag{3.26}$$

The attenuation constant of a mode is [78], [79]

$$\alpha = \frac{2R_s}{\eta b}\frac{k}{\beta} \times \begin{cases} \left(1 + \frac{b}{a}\right)\frac{\omega_c^2}{\omega^2} + \frac{b}{a}\left(\frac{\chi_n}{2} - \frac{\omega_c^2}{\omega^2}\right)\left(\frac{m^2ab + n^2a^2}{m^2b^2 + n^2a^2}\right) & if\ TE \\ \frac{m^2b^3 + n^2a^3}{m^2b^2a + n^2a^3} & if\ TM \end{cases} \tag{3.27}$$

Where $\chi_n$ is

$$\chi_n = \begin{cases} 1\ n = 0 \\ 2\ n > 0 \end{cases} = 1 + sign(n) \tag{3.28}$$

The normalized mode power averaged over time is the same for TE and TM modes and is given by:

$$p = \frac{k\beta ab}{2\chi_m\chi_n g^2\eta} \tag{3.29}$$

The characteristic wave impedance of a mode is

$$Z = \eta\frac{E_x}{H_y} = -\eta\frac{E_y}{H_x} = \eta \times \begin{cases} \frac{k}{\beta}\ if\ TE \\ \frac{\beta}{k}\ if\ TM \end{cases} \tag{3.30}$$

3.7.2 Cylindrical Waveguide Parameters

For a cylindrical waveguide, the cutoff wave numbers are given by roots of the Bessel function of the first kind of order $m$ $J_m(x)$ and its first derivative $J'_m(x)$:

$$g = \begin{cases} \dfrac{p'_{mn}}{a} \ if\ TE \\ \dfrac{p_{mn}}{a} \ if\ TM \end{cases} \tag{3.31}$$

where $p'_{mn}$ and $p_{mn}$ are the $n$-th nulls of equations $J'_m(x) = 0$ and $J_m(x) = 0$.

The attenuation constant of a mode is:

$$\alpha = \frac{R_s}{\eta a}\frac{k}{\beta} \times \begin{cases} \dfrac{\omega_c^2}{\omega^2} + \dfrac{m^2}{(p'_{mn})^2 - m^2} & if\ TE \\ 1 & if\ TM \end{cases} \tag{3.32}$$

The normalized mode power averaged over time is given by:

$$p = \frac{k\beta\pi}{4g^4\eta} \times \begin{cases} J_m^2(p'_{mn})[(p'_{mn})^2 - m^2] & if\ TE \\ J_m'^2(p_{mn})p_{mn}^2 & if\ TM \end{cases} \tag{3.33}$$

However, unlike rectangular waveguide, the mode power is different for TE and TM modes. The characteristic wave impedance of a mode is:

$$Z = \eta\frac{E_r}{H_\phi} = -\eta\frac{E_\phi}{H_r} = \eta \times \begin{cases} \dfrac{k}{\beta} \ if\ TE \\ \dfrac{\beta}{k} \ if\ TM \end{cases} \tag{3.34}$$

The above equations show the calculation for normalized power density $p_u$ for rectangular and cylindrical waveguides. To incorporate the specific antenna characteristics, an interaction integral $I_u$ for the same needs to be calculated. By default, a sinusoidal current distribution can be assumed on a PCB antenna:

$$\vec{J}(\zeta) = I_0 \frac{\sin k(l - \zeta)}{\sin kl} \vec{\zeta} \tag{3.35}$$

Where $I_0$ is the current amplitude at the feed point of the antenna, $k = \omega/c$ is the free space wave number, $l$ is the antenna length, and $\zeta$ is the coordinate along antenna length $(0 \leq \zeta \leq l)$.

### 3.8 Selective mode excitation

The capacity of the HVAC duct channel is severely impacted due to the presence of the multimode dispersion as it leads to a significant increase in the inter-symbol interference (ISI). With the knowledge of the excited mode distribution, modes with higher power can be selectively excited, leading to an effective reduction in the dispersion. Selective mode excitation can be performed using antenna arrays and can mean either a single mode is excited, or a preferred mode distribution is excited. In order to design an antenna which excites the preferred mode distribution, we need to examine the power radiated in the different excited modes. The power carried by mode $u$ is proportional to the radiation resistance $R_u$. Then, the mode power coefficient is given in terms of the power carried by the mode that has maximum radiation resistance normalized by the power carried by all the modes excited by the antenna:

$$P = \frac{\max R_u}{\sum_{u=1}^{U} R_u} \tag{3.36}$$

If a very large number of excited modes have similar % of power, then the value of $P$ will be near to 0, whereas if most of the power is carried by one mode then the value of $P$ will be 1. An alternative parameter that can be used is called the next mode rejection ratio. The parameter is calculated based on sorting the modes in terms of their radiation resistance which relates to the times the mode is excited. Assuming the mode that is excited most is modeA and the mode that is excited second to modeA is modeB. Then next mode rejection ratio is defined as a ratio of the power carried by modeA to the power carried by modeB. In order to deliver the maximum power from the transmitter to the antenna, it is importance to have proper impedance matching. The impedance mismatch is characterized in terms of the reflection coefficient $\Gamma$ which is defined in terms of the antenna impedance $Z_a$ and the transmitter impedance $Z_0$ as follows:

$$\Gamma = \frac{Z_a - Z_0}{Z_a + Z_0} \tag{3.37}$$

Power transmission coefficient $T$ indicates the quality of the impedance match and is defined as [78]:

$$T = 1 - |\Gamma|^2 \tag{3.38}$$

The parameter $T$ varies similar to the parameter $P$. In order to achieve optimum performance, we want to maximize mode power coefficient as well as transmission coefficient, therefore we define a linear cost function $C$ [78]:

$$C = W_P P + W_T T \tag{3.39}$$

where weights $W_P$ indicates the power delivered to a single mode propagating inside the duct and $W_T$ indicates the sum of the relative power of all the modes . In order to design an optimal antenna, we need to maximize the cost function and therefore, choose the weights accordingly.

### 3.9 Monopole antenna

As we are considering a PCB monopole antenna, the entire transceiver system can be assembled on the same PCB. Further the small size of the system due to the small wavelength of the mm-wave, makes it possible to implement the entire system on the walls of the HVAC duct. In order to provide the least obstruction due to the presence of the antenna in the HVAC duct, a PCB antenna will be the best suited. The dimensions of the PCB monopole antenna are same as a typical monopole antenna that has the arm length equal to quarter-wavelength. The antenna when used for communication in free space has an impedance which can be easily matched to a 50 Ω load. The current varies in a sinusoidal fashion being zero at the end of the arm of monopole and maximum at the connection between the antenna and the source. The metallic walls of the HVAC duct act as the ground for the monopole antenna and leads to a change in its radiation characteristics.

### 3.9.1 Radiation Resistance due to Monopole in Rectangular Waveguide

Consider a rectangular waveguide with a PCB monopole antenna placed inside it as shown in Figure 3.2. The antenna is characterized by its length $l$, width $w$ and its distance from the waveguide wall $d$. However, since the current on the PCB monopole antenna varies along its length, we can consider that the coordinate $\zeta$ along the length of the antenna is $\zeta = y$. Therefore, the interaction integral of interest $I$ is:

$$I = \int_0^l \epsilon_y(y)|_{x=d} \frac{\sin k(l-y)}{\sin kl} dy \qquad (3.40)$$

Where $k$ is the free space wave number.

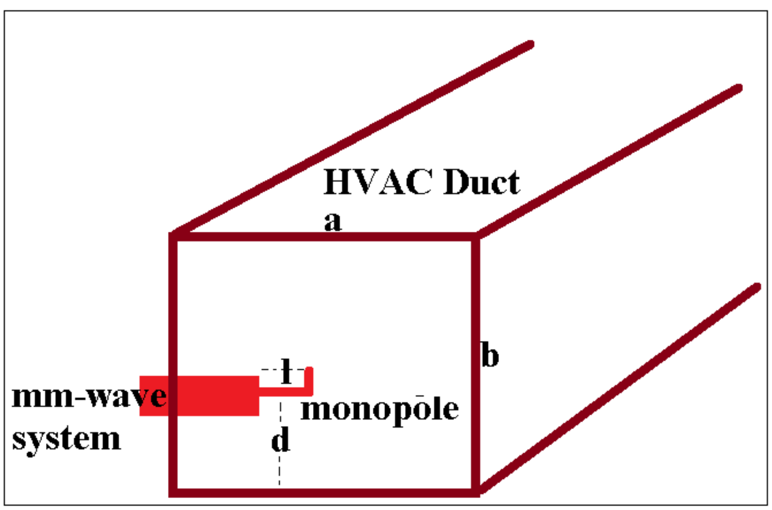


Figure 3.2. Mm-wave system with a monopole antenna inside a rectangular HVAC duct

We calculate an intermediate result in order to compute the mode radiation resistance:

$$D = \int_0^l \cos\frac{m\pi y}{a}\sin k(l-y)\,\partial y = \frac{1}{k}\left[\frac{\cos\frac{m\pi l}{a} - \cos kl}{1-\left(\frac{m\pi}{ka}\right)^2}\right] \tag{3.41}$$

Using the interaction integral and the intermediate result, the mode radiation resistance can be found as [60]

$$R = \eta\frac{\pi^2 D^2 \chi_m \chi_n}{2\beta a b g^2 \sin^2 kl}\sin^2\frac{m\pi d}{a} \times \begin{cases} \frac{km^2}{a^2} & if\ TE \\ \frac{\beta n^2}{b^2} & if\ TM \end{cases} \tag{3.42}$$

Where $\chi_m$ is given by Equation (3.28).

### 3.9.2 Radiation Resistance due to Monopole in Cylindrical Waveguide

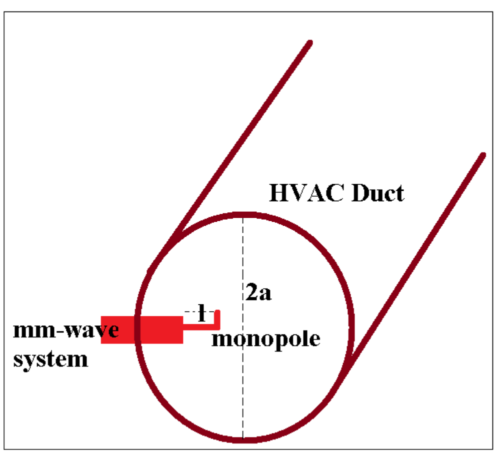


Figure 3.3. Mm-wave system with a monopole antenna inside a circular HVAC duct

Figure 3.3 above shows the monopole antenna coupled in a cylindrical waveguide, mentioning the duct dimension and the antenna length. Similarly, mode radiation resistance due to a monopole antenna for the cylindrical duct can be calculated as [60]

$$if\ TE, l \leq a: \qquad R = \frac{\eta k m^2}{\pi \sin^2 kl\, \beta}\left[\int_{1-\frac{l}{a}}^{1} \frac{J_m(ga\zeta) \sin ka\left(\frac{l}{a} - 1 + \zeta\right)}{J_m^2(ga)(g^2a^2 - m^2)\zeta} \partial\zeta\right]^2$$

$$if\ TE, \&\ l > a: R$$

$$= \frac{\eta k m^2}{\pi \sin^2 kl\, \beta J_m^2(ga)(g^2a^2 - m^2)}\left[\begin{array}{c} \displaystyle\int_0^1 \frac{J_m(ga\zeta)\sin ka\zeta}{\zeta}\partial\zeta \\ \displaystyle -(-1)^n \int_0^{\frac{l}{a}-1} \frac{J_m(ga\zeta)\sin ka\left(\frac{l}{a} - 1 + \zeta\right)}{\zeta}\partial\zeta \end{array}\right]^2$$

$$if\ TM, l \leq a: \qquad R = \frac{\eta\beta}{\pi k J_m'^2(ga)\sin^2 kl}\left[\int_{1-\frac{l}{a}}^{1} J_m'(ga\zeta)\sin ka\left(\frac{l}{a} - 1 + \zeta\right)\right]^2$$

$$if\ TM, l > a: R = \frac{\eta\beta}{\pi k J_m'^2(ga)\sin^2 kl}\left[\begin{array}{c} \displaystyle\int_0^1 J_m'(ga\zeta)\sin ka\zeta\,\partial\zeta \\ \displaystyle -(-1)^n \int_0^{\frac{l}{a}-1} J_m'(ga\zeta)\sin ka\left(\frac{l}{a} - 1 - \zeta\right)\partial\zeta \end{array}\right]^2 \tag{3.43}$$

As the current on the PCB monopole antenna varies along its length $l$, therefore, using the antenna inside the HVAC duct gives us two variable parameters: antenna length $l$ and its distance to the wall $d$. We can consider two different dimensions of the rectangular duct (i) 30.5 cm x 15 cm (ii) 12.7 cm x 6 cm. Further as the monopole length is usually considered to be $\lambda/2$

and $\lambda/4$, therefore we will consider two different antenna lengths to be 2.5 mm and 1.25 mm and both these antennas will be used for the two duct dimensions mentioned. Figure 3.4 shows the mode distributions excited by monopole antenna in case of a rectangular duct of dimension 30.5 cm × 15 cm. 3.4a shows the mode distribution when the antenna length $l = 2.5$ mm and as the duct is of dimension 30.5 cm × 15 cm, it allows us to vary the position of the antenna inside the duct by distance $d = 15$ cm. Figure 3.4b shows the mode distribution when the antenna length $l = 1.25$ mm and $d = 15$ cm. Despite the change in the antenna length $l$ , the mode distribution as well as the power of the mode $TE_{53,54}$ remains the same. and $l = 1.25$ mm, $d =$ 6 cm is shown in Figure 3.5A and Figure 3.5B, respectively. Compared to the antenna length $l = \lambda/2$, the second antenna length $l = \lambda/4$ which is the more optimized antenna has better mode excitation characteristics. Namely, more than 15 percent of total power is now transmitted into mode $TE_{21,22}$.

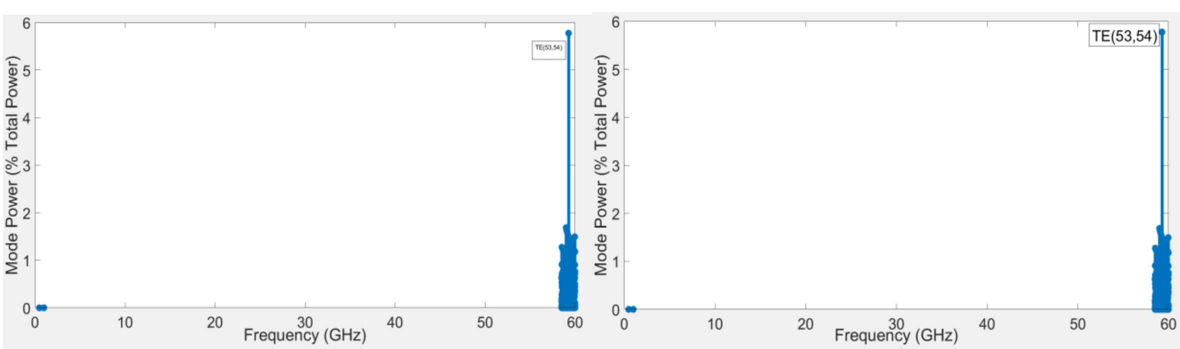

(a) (b)

Figure 3.4. Modes in rectangular duct by monopole of (a) $l$ = 2.5 mm and, (b) $l$ = 1.25 mm

Figure 3.5 shows the mode distributions excited by monopole antenna in case of a rectangular duct of dimension 12.7 cm × 6 cm. Figure 3.4a and 3.4b show the mode distribution when the antenna length $l = 2.5$ mm and $l = 1.25$ mm respectively, with $d = 6$ cm. Despite the change in the antenna length $l$, the mode distribution as well as the power of the mode $TE_{21,22}$ remains the same. Compared to the antenna length $l = \lambda/2$, the second antenna length $l = \lambda/4$ which is the more optimized antenna has better mode excitation characteristics. Namely, more than 15 percent of total power is now transmitted into mode $TE_{21,22}$.

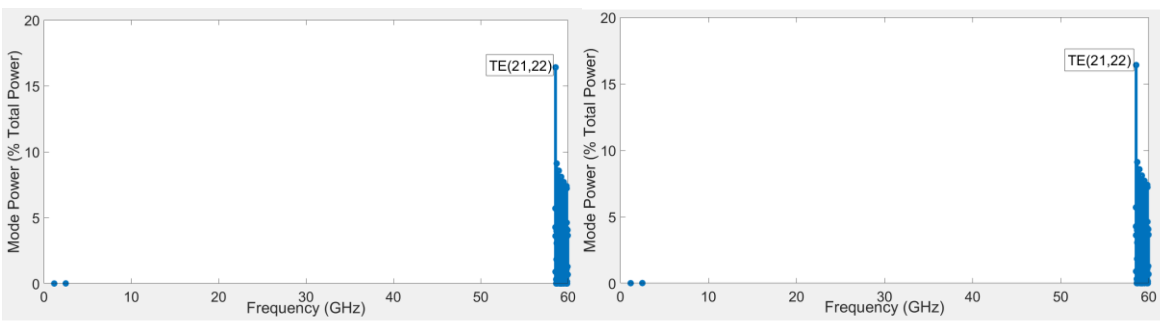


(a) (b)

Figure 3.5. Modes in rectangular duct by monopole of (a) $l$ = 2.5 mm and, (b) $l$ = 1.25 mm

Consider a cylindrical waveguide with a PCB monopole antenna placed inside it. In case of the cylindrical duct, we can consider the two dimensions for diameter $d = 30.5$ cm and $d = 12.7$ cm. Again, as the monopole length is usually considered to be $\lambda/2$ and $\lambda/4$, therefore we will consider two different antenna lengths to be 2.5 mm and 1.25 mm and both these antennas will be used for the two duct dimensions mentioned. Figure 3.6a and 3.6b show the mode distribution for a cylindrical duct of diameter $d = 30.5$ cm which is excited by a monopole antenna with $l = 2.5$ mm and $l = 1.25$ mm respectively. Compared to the antenna length $l = \lambda/2$, the second antenna length $l = \lambda/4$ is the more optimized antenna therefore has better mode excitation characteristics as more % of total power is attributed to the four $TE$ modes.

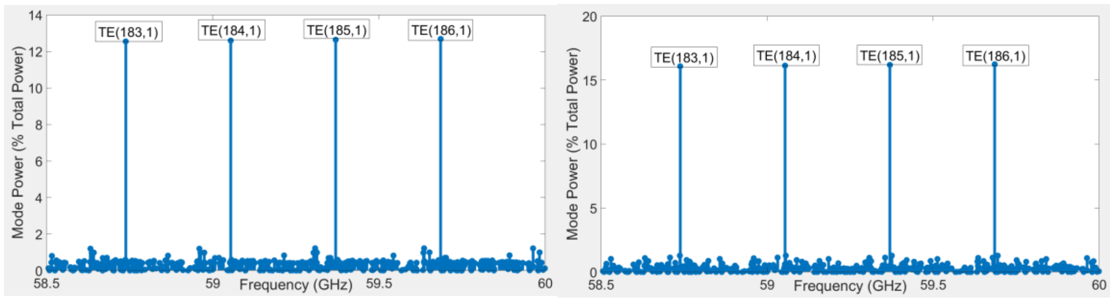


(a) (b)

Figure 3.6. Modes in a cylindrical duct by monopole of (a) $l$ = 2.5 mm and, (b) $l$ = 1.25 mm

Figure 3.7a and 3.7b show the mode distribution for a cylindrical duct of diameter $d = 12.7$ cm which is excited by a monopole antenna with $l = 2.5$ mm and $l = 1.25$ mm respectively. Compared to the antenna length $l = \lambda/2$, the second antenna length $l = \lambda/4$ is the more optimized antenna therefore has better mode excitation characteristics as more % of total power is attributed to the two $TE$ modes. However, compared to the Fig. 3.6 where the total power gets divided between four $TE$ modes, in the present case when the duct diameter is smaller, the total power gets divided between only two $TE$ modes. Similar to the rectangular HVAC duct, the antenna length $l = \lambda/4$ is the more optimized antenna and therefore, more than 75 percent of total power is now transmitted into two modes $TE_{75,1}$ and $TE_{76,1}$. However as compared to the rectangular duct where only 17% of the total power was going into one mode $TE_{21,22}$, we observe that in case of cylindrical duct, the total power is divided mostly between the two modes $TE_{75,1}$ and $TE_{76,1}$.

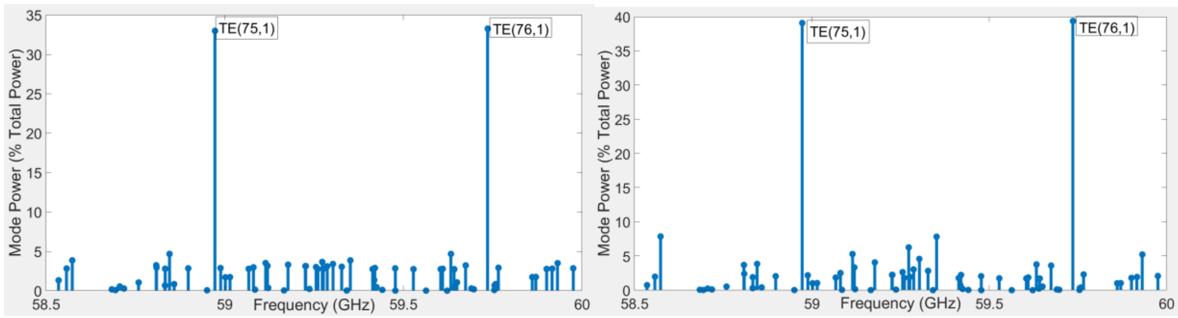


(a) (b)

Figure 3.7. Modes in a cylindrical duct by monopole of (a) $l$ = 2.5 mm and, (b) $l$ = 1.25 mm

## 3.10 Dipole antenna

As the radiation pattern of a dipole antenna is vertically symmetric compared to a monopole antenna, for which the radiation pattern depends on the orientation of the ground plane, a PCB dipole antenna will generate more mode distributions thereby increasing mode selectivity compared to a monopole antenna. Also, the dipole antenna has a symmetrical radiation pattern, which leads to limited current interaction, hence decreasing the number of waveguide modes. However, as the two arms of a dipole antenna are out-of-phase from each other, a balanced-to-unbalanced (balun) device is required to provide the impedance matching.

### 3.10.1 Radiation Resistance due to Dipole in Rectangular Waveguide

Similar to the PCB monopole antenna, we will begin with a rectangular waveguide and a PCB dipole antenna placed inside it as shown in Figure 3.9. We can adjust the height $h$, the arm length $l$, and the position $d$ of the dipole antenna from the duct walls. The coordinate $\zeta$ along the antenna is $\zeta = |x - d|$. The interaction between the current induced on the antenna and the electric field generated as a result, is calculated in terms of the interaction integral $I$ as follows:

$$I = \int_{d-l}^{d} \epsilon_x(x)|_{y=h} \frac{\sin k(l + x - d)}{\sin kl} \partial x + \int_{d}^{d+l} \epsilon_x(x)|_{y=h} \frac{\sin k(l - x + d)}{\sin kl} \partial x \tag{3.44}$$

In order to calculate the radiation resistance, we can calculate the intermediate result given as:

$$D = \int_{d-l}^{d} \cos\frac{m\pi x}{a} \sin k(l + x - d)\, \partial x + \int_{d}^{d+l} \cos\frac{m\pi x}{a} \sin k(l - x + d)\, \partial x \tag{3.45}$$

Similar to a PCB monopole antenna placed inside a rectangular waveguide, a PCB dipole antenna design can also be optimized using parameters $P$ and $T$, calculated using the interaction $I$ between the antenna current and the resultant electric field. The mode radiation resistance for a rectangular waveguide can be found as [60]:

$$R = \eta \frac{\chi_m \chi_n D}{2k^2 \beta ab} \frac{\pi^2 \sin^2 \frac{n\pi h}{b}}{g^2 \sin^2 kl} \times \begin{cases} \frac{kn^2}{b^2} \; if\ TE \\ \frac{\beta m^2}{a^2} \; if\ TM \end{cases} \tag{3.46}$$

3.10.2 Radiation Resistance due to Dipole in Cylindrical Waveguide

As mostly a cylindrical HVAC duct is preferred compared to a rectangular HVAC, we should also look at the radiation resistance of a PCB dipole antenna placed inside a cylindrical waveguide. Consider a mm-wave transceiver system with embedded dipole antenna attached vertically on the walls of the cylindrical HVAC duct as shown in Figure 3.8.

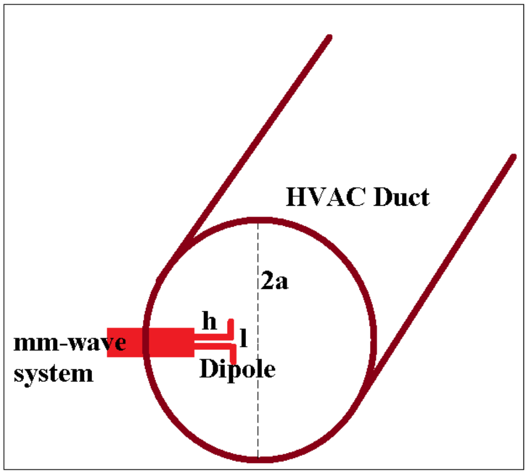

Figure 3.8. Mm-wave system with a dipole antenna inside a circular HVAC duct

Due to the symmetricity of the cylindrical HVAC duct, the dipole placed inside it will have the height $h$ and the arm length $l$ as the variable parameters. We can also consider alternative parameters such as the circumferential dipole radius (arc radius) $r_d = a - h$ and the arm angle $\phi_l = l/(a - h)$. The interaction between the current induced on the dipole antenna and the electric field associated with it is defined in terms of the integral as follows:

$$I = \int_{-\phi_l}^{\phi_l} \frac{\sin k(l - r_d|\phi|)}{\sin kl} \varepsilon_\phi(\phi)\Big|_{r=r_d} r_d \partial\phi \tag{3.47}$$

Where the interaction is calculated along the antenna coordinate $\zeta = r_d|\phi|$. An intermediate result needed for computation of radiation resistance is:

$$D = \int_0^{\phi_l} \sin k(l - r_d\phi) \cos n\phi \, \partial\phi$$

$$= \frac{kr_d \cos kl}{m^2 - k^2 r_d^2} + \frac{1}{2}\left[\frac{\cos kl \cos \phi_l (m - kr_d)}{m - kr_d} + \frac{\sin kl \sin \phi_l (m - kr_d)}{m - kr_d} + \frac{\cos kl \cos \phi_l (m + kr_d)}{m + kr_d} + \frac{\sin kl \sin \phi_l (m + kr_d)}{m + kr_d}\right] \quad (3.48)$$

Using the above two results, the mode radiation resistance for a circular waveguide can be found as [60]:

$$R = \eta \frac{D^2}{\pi \sin^2 kl} \times \begin{cases} \dfrac{k}{\beta} \dfrac{g^2 r_d^2 J_m'^2(gr_d)}{J_m^2(ga)[(ga)^2 - m^2]} & if\ TE \\ \dfrac{\beta}{k} \dfrac{m^2 J_m^2(gr_d)}{g^2 a^2 J_m'^2(ga)} & if\ TM \end{cases} \quad (3.49)$$

# CHAPTER 4

# HVAC CHANNEL FREQUENCY RESPONSE

## 4.1 Introduction to HVAC Duct Channel

For a wireless communication system, the most crucial aspect is to understand the channel through which the signal is going to propagate and the same is the case for the HVAC duct channel. The overall capacity of the wireless communication system will be determined by the HVAC duct channel characteristics. Therefore, it is of foremost importance to have a theoretical model for the HVAC duct channel and understand its properties in relation to the various wireless communication parameters such as bit-rate, signal to noise ratio, received signal strength indicator and bit-error-rate.

In the simplest form, the HVAC duct channel is comprised of large hollow cylindrical or rectangular waveguide, with the transmitting and the receiving antennas coupled to it for introduction of the electromagnetic signal. As any communication channel is characterized by its frequency response, therefore we need to calculate the frequency response of the HVAC duct channel. The analytical frequency response must be valid for ducts of different cross-sections and should account for different antenna geometries, transmitter-receiver separation distance, material of the duct and the temperature and moisture of the air flowing through the HVAC duct.

Figure 4.1 shows the block diagram of the HVAC duct communication system. At the transmitter side, the transmitting antenna which is coupled to the HVAC duct, which excites the electromagnetic modes that propagate through the duct. The modes are received by the receiving antenna and finally distributed to the users through the receiver.

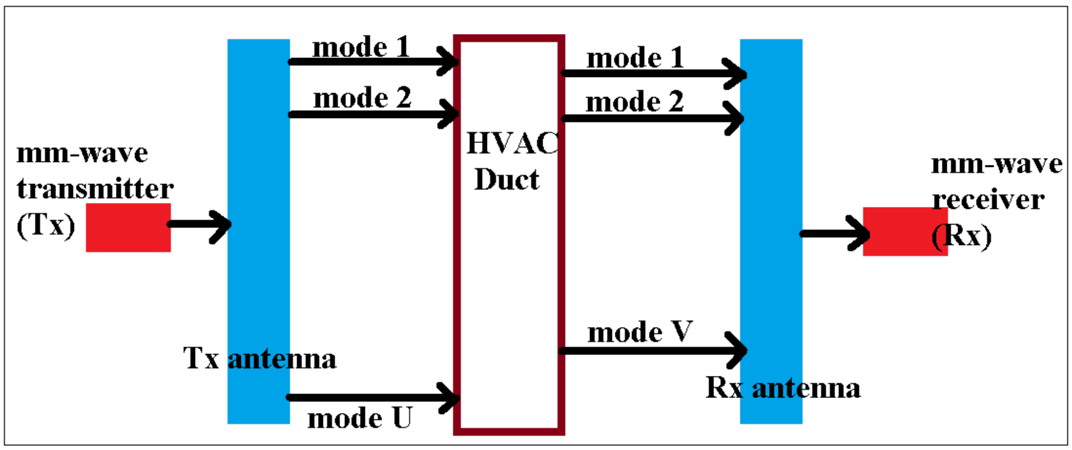

Figure 4.1. Block diagram of a mm-wave communication system using HVAC ducts

### 4.2 Arbitrary duct system

The HVAC duct installed in the different residential and commercial buildings can take various shapes and architectures. In order to understand the duct system, we can begin by limiting ourselves to a straight section of the duct, which is coupled on the two ends by the transmitting and the receiving antenna. The transmitting antenna is inside the HVAC duct and therefore excites the electromagnetic modes due to the radiation in the HVAC duct. On the other end, the receiving antenna present inside the HVAC duct collects the electromagnetic signal and transfers it to the receiver system. Therefore, the transfer matrix for the HVAC duct system describes the transformation of the incoming modes into the outgoing mode distribution due to the interaction with the metallic waveguide walls as shown in Figure 4.2.

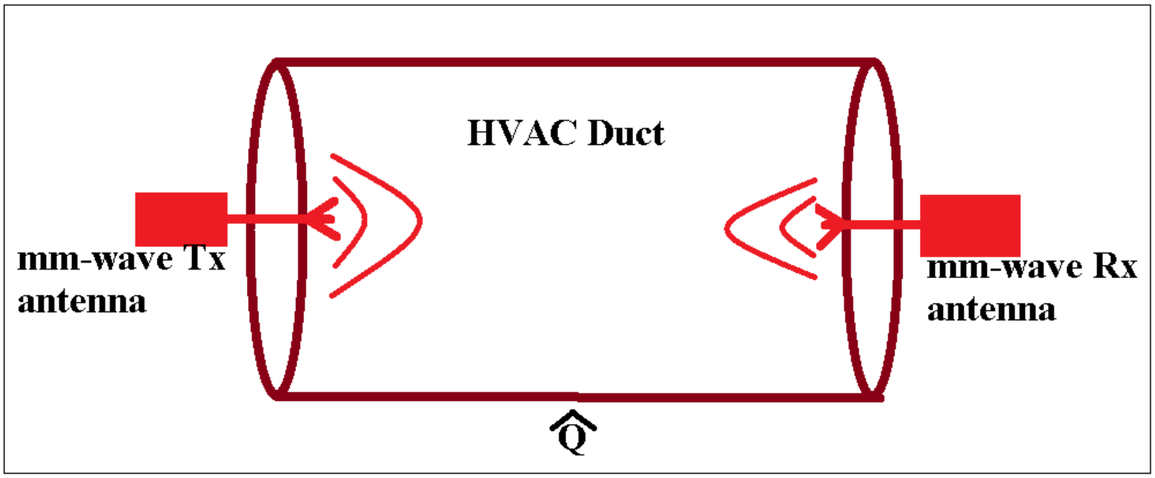

Figure 4.2. Transmitting and receiving antennas in an arbitrary duct system

The transfer matrix for the system is represented by $\hat{T}$. The total number of modes which will be propagating is calculated based on the structure of the waveguide and the frequency of operation. The electric field $\vec{E}$ in a waveguide with specific dimensions is calculated as summation of the total number of modes $U$ propagating through the waveguide as [78]

$$\vec{E} = \sum_{u=1}^{U} \vec{E}_u = \sum_{u=1}^{U} C_u \overrightarrow{\epsilon_u} e^{\pm \gamma_u z} \tag{4.1}$$

Where $u$ is representing the mode, $\vec{E}_u$ is electric field generated due to mode $u$ in the waveguide, $C_u$ is the mode coefficient, $\overrightarrow{\epsilon_u}$ is normalized electric field, $\gamma_u$ is the propagation constant, and $z$ is the waveguide's coordinate along which propagation takes place. Mode coefficient $C_u$ volts per meter (V/m) is calculated from amplitude of the electric field. To derive the response of the HVAC duct channel, we need to have knowledge about the amplitude of all the modes which are excited by the antenna at the transmitter. The amplitude of the modes excited by an antenna can be calculated in terms of the mode coefficients $C_u$ which depends on the power density flow conservation rule. The rule states that the power present on the transmitting antenna will be equal to the mode power in the direction of receiver [78]:

$$P_u = -\frac{1}{2}\int \vec{E}_u.\vec{J}\,\partial S = |C_u|^2 p_u \tag{4.2}$$

Where $P_u$ is the mode $u$ power averaged over time in one direction, $\vec{J}$ amperes per meter (A/m) is the surface current density on the transmitting antenna and we calculate the integration over the surface area A of the transmitting antenna. Further, the time average can also be represented in terms of $p_u$ which is the normalized power carried by mode $u$. The surface current density on the transmitting antenna can be represented as [78]

$$\vec{J} = I_0\vec{j} \tag{4.3}$$

Where $I_0$ is the amplitude of the current present on the terminals of the antenna and $\vec{j}$ is the distribution of the normalized surface current density. The transmitting antenna excites the mode coefficients which can be given as [78]

$$C_u = -\frac{I_0}{4p_u}\int \overrightarrow{\epsilon_u}.\,\vec{j}\,\partial S \tag{4.4}$$

We can write the same equation for the mode coefficient for the receiver due to the time reversal [68] and reciprocity principles [56], [69], [70].

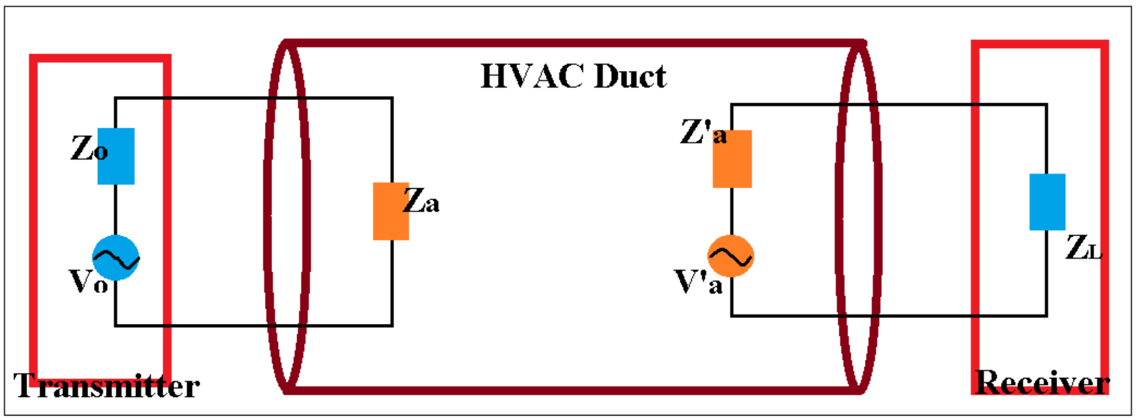

Figure 4.3. Circuit model of the HVAC duct communication system

Figure 4.3 shows the circuit model of the HVAC communication system, where $V_0$ is the voltage on the transmitter antenna, $Z_0$ is the internal impedance, $Z_a$ is the transmitting antenna impedance, $Z'_a$ is the receiving antenna impedance, $V'_a$ is the voltage on the receiver antenna, and $Z_L$ is the internal impedance of the load. The current induced in the HVAC duct through the transmitting antenna can be given as

$$I_0 = \frac{V_0}{Z_a+Z_0} \tag{4.5}$$

Based on our assumption that the total current induced in the HVAC duct is equal to the current induced by the independent sources which excite the individual electromagnetic modes $v$ which traverse through the duct. Therefore, the total voltage on the receiving antenna can be represented as

$$V_a' = \sum_{v=1}^{V} V_v' \tag{4.6}$$

Where $V_v' = I_v' Z_v'$ and $V$ is the total number of the modes received at the antenna. The sum of these voltage follow a linear trend as the waveguide modes are orthogonal. Similar to the current induced by the transmitting antenna, the total current delivered to the load at the receiving end is given as

$$I_L = \frac{V_a'}{Z_a' + Z_L} \tag{4.7}$$

The channel frequency response should be comparable to a reference system when we connect the transmitter and the receiver directly with a cable. Therefore, we define the channel frequency response in terms of the load voltage and the voltage $V_{REF}$ of the reference system [78]:

$$H(\omega) = \frac{V_L}{V_{REF}} = \frac{(Z_0 + Z_L)V_a'}{(Z_a' + Z_L)V_0} = \frac{Z_0 + Z_L}{(Z_0 + Z_a)(Z_a' + Z_L)} \sum_{v=1}^{V} - \frac{4p_v' Z_v' C_v}{I_0 \int \vec{\epsilon}_v . \vec{J}' dS'} \tag{4.8}$$

Where $V_{REF} = V_0 Z_L / (Z_0 + Z_L)$ .

The amplitude of the mode coefficient which is excited by the transmitter antenna is represented by $\vec{C}$ and it is related to the mode coefficient $\vec{C}'$ which is excited by the receiver antenna as follows:

$$\vec{C}' = \hat{Q}\vec{C} \tag{4.9}$$

Where $\hat{Q}$ is the system transfer matrix, that describes the relationship between the mode content at the transmitter and at the receiver. Using the interaction integral equation defined in the last chapter, we can describe the frequency response as follows [78]

$$H(\omega) = \frac{Z_0 + Z_L}{(Z_0 + Z_a)(Z_a' + Z_L)} \sum_{v=1}^{V} \frac{Z_v' p_v'}{I_v'} \sum_{u=1}^{U} \frac{Q_{vu} I_u}{p_u} \tag{4.10}$$

Where $Q_{vu}$ are the elements of the transfer matrix $\hat{Q}$

### 4.3 Straight Duct

Due to the modal nature of the HVAC duct channel, it can be analyzed using the transfer matrix theory and can be characterized by its frequency response which presents a clear relation between the different duct geometry parameters such as length, radius and conductivity of duct material etc., antenna geometry and the mm-wave signal characteristics. Consider a straight HVAC duct of rectangular or circular cross-section, which is made of metal and connected to the transmitting and receiving antenna (with antenna impedance $Z_a$) on either end, see Figure

4.4. Such a duct acts as a multimode waveguide with the number of propagating modes $N$ depending on the signal frequency and dimensions of the duct. The duct can be terminated by metal caps on its end 1 and 2 having respective reflection coefficients $G_1$ and $G_2$. The distance between the transmitter and the receiver is $L$, and the respective distances to the terminated ends are $L_1$ and $L_2$.

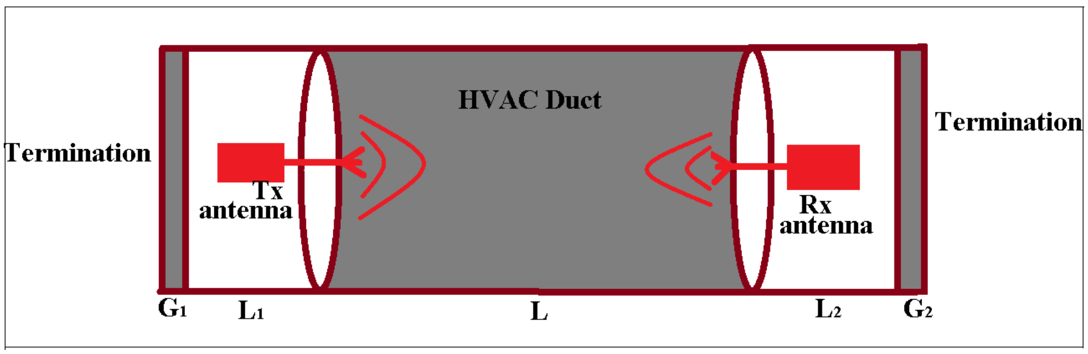


Figure 4.4. Transmitting and receiving antenna in a straight HVAC duct

For such a system, the transfer matrix will comprise of following square and diagonal matrices:

$$
\begin{aligned}
P_{uv} &= e^{-\gamma_u L_1}\delta_{uv} \\
Q_{uv} &= e^{-\gamma_u L}\delta_{uv} \\
R_{uv} &= e^{-\gamma_u L_2}\delta_{uv} \\
F_{uv} &= G_1\delta_{uv} \\
G_{uv} &= G_2\delta_{uv} \qquad (4.11)
\end{aligned}
$$

Where $\delta_{uv}$ is the Kronecker delta. Using the above four matrices we can find the complete transfer matrix and therefore, the frequency response of a straight HVAC duct is given as follows [67], [80]

$$H(\omega) = \frac{2Z_0}{(Z_0 + Z_a)} \sum_{v=1}^{V} Z_v e^{-\gamma_v L} \frac{(1 + G_1 e^{-2\gamma_v L_1})(1 + G_2 e^{-2\gamma_v L_2})}{1 - G_1 G_2 e^{-2\gamma_v (L + L_1 + L_2)}} \tag{4.12}$$

where $Z_0$ is the internal impedance of the transmitter and the receiver. $Z_v$ is the mode impedance and $\gamma_v$ is the mode propagation constant. $H(\omega)$ depends on the type of the antenna being used, its geometry, and the antenna placement in the duct through the parameters $Z_a$ and $Z_n$.

Channel gain $\big(A(f)\big)$ defines the drop in the power of the signal propagating through the channel and is used to calculate RSSI reported by the receiver. RSSI predicts the overall coverage distance and evaluate the signal quality at that distance. The channel attenuation in [dB] is:

$$A(f) = -10 \log|H(\omega)| \tag{4.13}$$

Using the above equation, we can calculate the channel gain for the two types of HVAC ducts: cylindrical and rectangular. Further in order to examine the effect of using the optimized antenna which would lead to better coupling with the HVAC duct channel, we look at two different antenna lengths: $\lambda/4$ and $\lambda/2$. Figure 4.5 shows the channel gain (dB) calculated for the cylindrical waveguide with antenna length $l = \lambda/2 = 2.5$ mm and for four HVAC duct length (a) $L = 1$ m, (b) $L = 2$ m, (c) $L = 4$ m and (d) $L = 8$ m. We observe that the channel gain changes from an average of $-16$ dB to $-22$ dB as the duct length is increased but shows almost similar frequency selective fading characteristics.

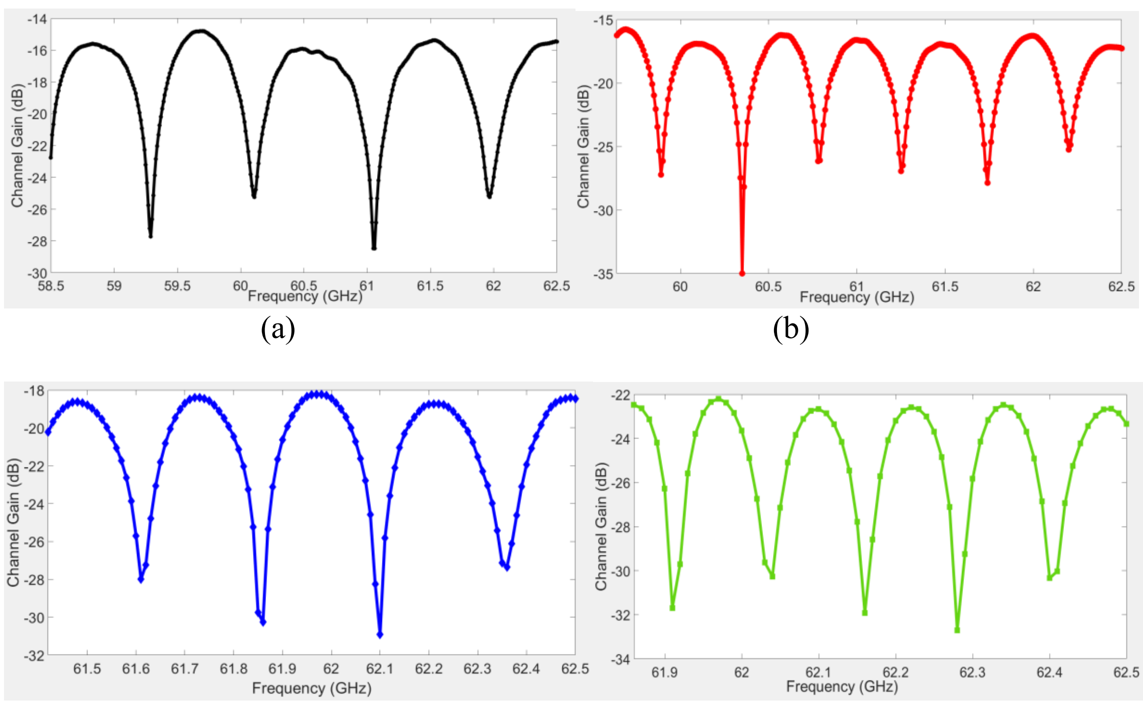


(a) (b) (c) (d)

Figure 4.5. Channel gain due to antenna $l = 2.5$ mm in cylindrical duct length $L =$ (a) 1 m, (b) 2 m, (c) 4 m and (d) 8 m

Figure 4.6 shows the channel gain (dB) calculated for the cylindrical waveguide with antenna length $l = \lambda/4 = 1.25$ mm and for four HVAC duct length (a) $L = 1$ m, (b) $L = 2$ m, (c) $L = 4$ m and (d) $L = 8$ m. We observe that the channel gain changes from an average of $-8$

dB to $-14$ dB, therefore with a better antenna design, the channel attenuation can be reduced sufficiently.

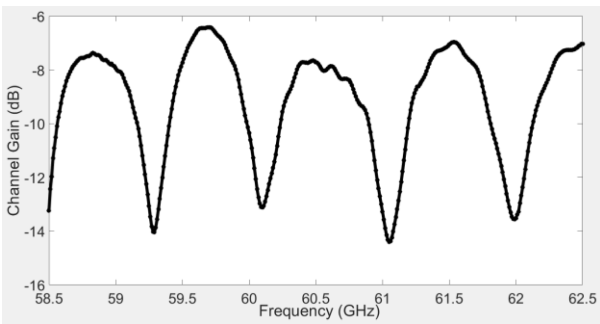


(a)

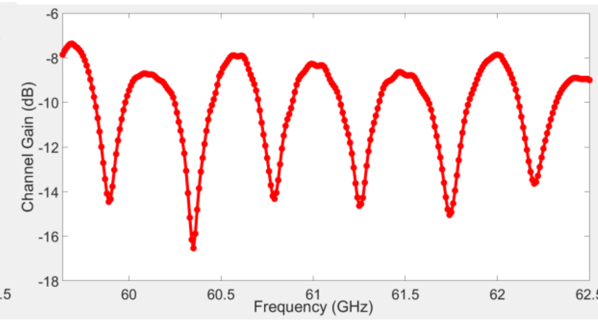


(b)

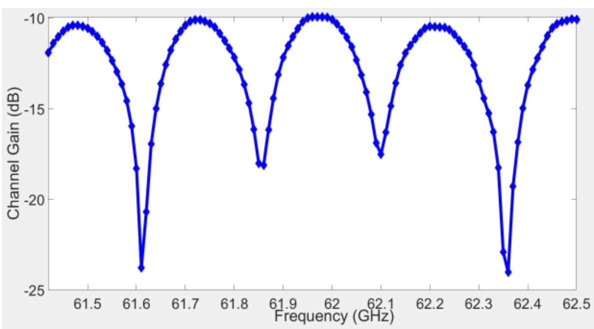


(c)

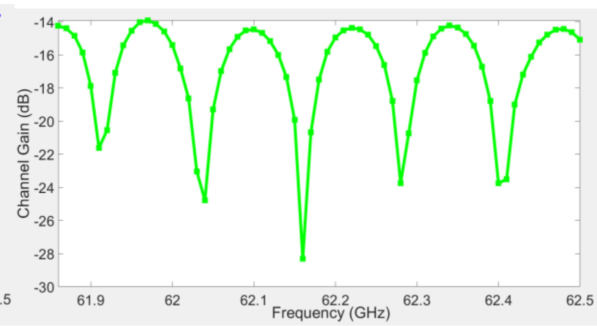


(d)

Figure 4.6. Channel gain due to antenna $l = 1.25$ mm in cylindrical duct length $L =$ (a) 1 m, (b) 2 m, (c) 4 m and (d) 8 m

Figure 4.7 shows the channel gain (dB) calculated for the rectangular waveguide with dimension 12.7 cm x 6 cm and antenna length $l = \lambda/2 = 2.5$ mm and for four HVAC duct length (a) $L = 1$ m, (b) $L = 2$ m, (c) $L = 4$ m and (d) $L = 8$ m. We observe that the channel gain for the rectangular duct is low as compared to the cylindrical duct by around -35 dB. However, the channel gain remains almost constant at $-53$ dB irrespective of the increase in the duct length from $L = 1$ m to 8 m.

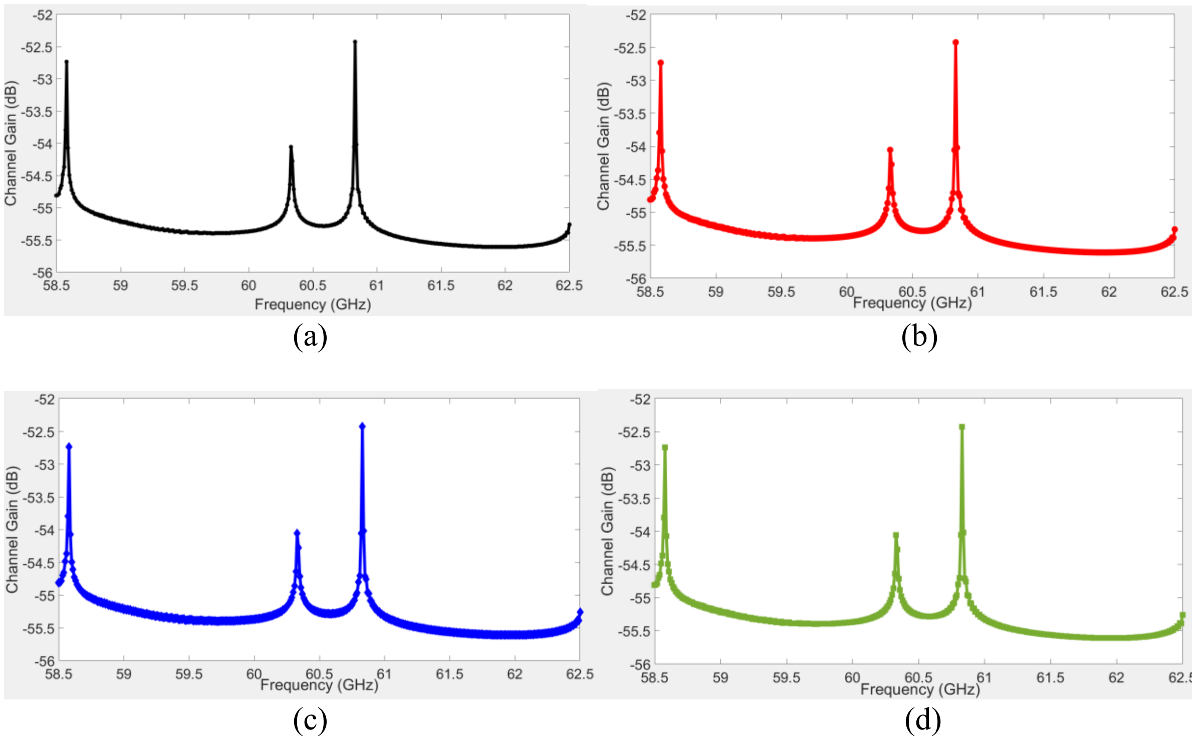


Figure 4.7. Channel gain due to antenna $l = 2.5$ mm in rectangular duct length $L =$ (a)1 m, (b) 2 m, (c) 4 m and (d) 8 m

Figure 4.8 shows the channel gain (dB) calculated for the rectangular waveguide with dimension 12.7 cm x 6 cm and antenna length $l = \lambda/4 = 1.25$ mm and for four HVAC duct length (a) $L = 1$ m, (b) $L = 2$ m, (c) $L = 4$ m and (d) $L = 8$ m. We observe, in contrast to the cylindrical duct with a more optimized antenna, the antenna length in the rectangular duct has no significant effect in reducing the channel attenuation. However, similar to the rectangular duct with antenna length $l = \lambda/2$, the channel gain remains constant at $-61$ dB on increasing the length of the duct.

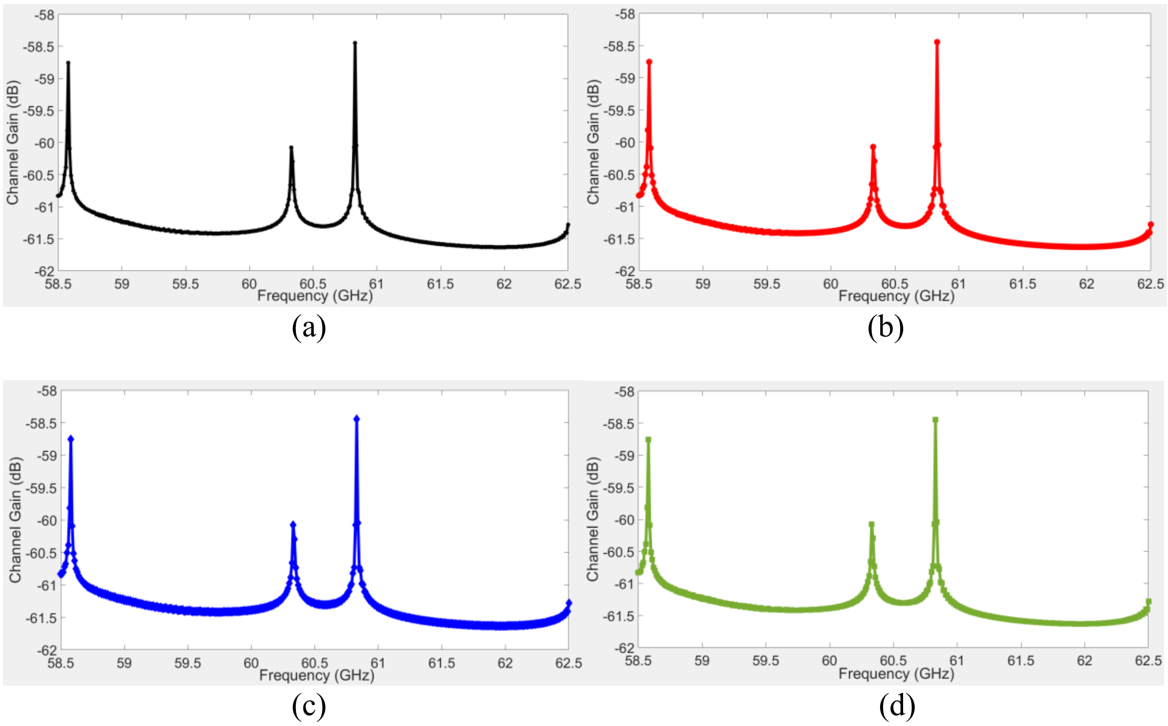

Figure 4.8. Channel gain due to antenna $l = 1.25$ mm in rectangular duct length $L =$ (a) 1 m, (b) 2 m, (c) 4 m and (d) 8 m

The transmitted signal power is usually referred to as the effective isotropic radiated power (EIRP). The RSSI will depend on it according to the link budget expression:

$$RSSI\ [dBm] = EIRP\ \pm A(f) + G_{RX}(f) + G_{TX}(f) \tag{4.14}$$

Where $G_{RX}(f)$ and $G_{TX}(f)$ is the frequency-dependent gain of the receiver and transmitter, respectively. But for now, it is assumed as flat.

# CHAPTER 5

# HVAC DUCT SYSTEM

## 5.1 Introduction to Transfer Matrix Theory

In order to calculate the response of a complex HVAC duct system, we need to calculate the frequency response of the end-to-end HVAC duct channel. Since we have framed the equation of the channel frequency response in terms of the system transfer matrix, therefore, we apply transfer matrix theory to calculate the overall response of the HVAC duct system. We can consider the HVAC duct system as a two-port network, for which the propagation path is from the transmitter to the receiver. Other than the transfer matrix parameters, other equivalent parameters such as impedance matrix $Z$, admittance matrix $Y$, hybrid matrix $h$, chain matrix $ABCD$, scattering matrix $S$, can be used to describe an arbitrary two-port network. For a multimode device, the elements of the aforementioned matrices are sub-matrices [81], [82]. In case of HVAC duct element, the transfer matrix for the individual elements needs to be calculated only once and can be used for subsequent propagation computations. In this Chapter, we will analyze the various shapes and components of the HVAC duct which includes straight sections, bends, tapers, and T-junctions. In order to calculate the frequency response of the entire HVAC system, we will derive the analytical transfer matrices which when used collectively form the transfer matrix of the system. We will analytically derive transfer matrices for straight sections, bends, and tapers. We will also give the experimental results obtained for the different duct components. Rectangular components can be analyzed similarly.

## 5.2 General Transfer Matrix

The HVAC duct system is a complex network of interconnected individual ducts that have rectangular or circular cross-sections, and these hollow metal pipes act as waveguides. This complex waveguide network contains various inconsistencies due to differences in the shapes of individual ducts, such as bends, tapers and T-junctions, as seen in the example of Figure 5.1. The HVAC duct system in a building is a multimode waveguide structure. Efficient modelling of propagation in such a complicated network is a challenging task. From the point of view of radio propagation, this system consists of multiple cascaded elements, where each element can be considered as a mm-wave device with one physical input and one physical output. This system can be characterized by its transfer matrix, which can provide a good frequency-domain description of wave propagation in a cascaded system.

Figure 5.1. HVAC duct of diameter 12.7 cm having straight and bent sections

The matrix $\hat{Q}$ is a function of the element geometry and is given as [68]

$$\hat{Q} = \begin{bmatrix} Q_{11} & Q_{12} & \cdots & Q_{1U} \\ Q_{21} & Q_{22} & \cdots & Q_{2U} \\ . & . & \cdots & . \\ Q_{V1} & Q_{V2} & \cdots & Q_{VU} \end{bmatrix} \tag{5.1}$$

where $U$ and $V$ represent the total modes entering port 1 and exiting port 2 respectively. Based on the matrix $\hat{Q}$, we can deduce that the HVAC duct structure is a linear system.

## 5.3 Cascaded system

A transfer matrix method helps us in determining the response of an entire system consisting of several cascaded components, provided that we know the transfer matrices of the individual components. Consider an arbitrary HVAC duct system shown in Fig. 5.2. The HVAC duct system is made up of different sections of individual ducts (straight and a $45°$ bend, as shown in Fig. 5.2) and each individual duct element $k$ can be characterized by its transfer matrix $\hat{Q}_k$. As the individual duct elements are connected to each other linearly, using the superposition principle of linear systems, the end-to-end transfer matrix of the HVAC duct system present between transmitter and receiver can be written as the products of the individual duct transfer matrices [68]

$$\hat{Q} = \hat{Q}_k \hat{Q}_{k-1} \ldots \hat{Q}_1 \tag{5.2}$$

The shapes of the ducts have distinct impacts on the signal transmission. The general transfer matrix for a section of a duct is given by

$$Q_{mn} = \sqrt{\frac{\beta_a}{\beta_a}} e^{-\gamma_i L_i} \delta_{mn} \tag{5.3}$$

where $\beta_a$ and $\beta_b$ are the phase constants of sections with radii $a$ and $b$ respectively. $\gamma_i$ and $L_i$ are the complex propagation constants and length of the $i^{th}$ section of the duct. $\delta_{mn}$ is the Kronecker delta function. In case of a duct with tapers, the radii $a$ and $b$ are different, and the length $L_i$ refers to the length of the straight section in between the two tapered ends. The order of multiplication of the transfer matrices is important and non-diagonal elements of each matrix represent coupling between different modes.

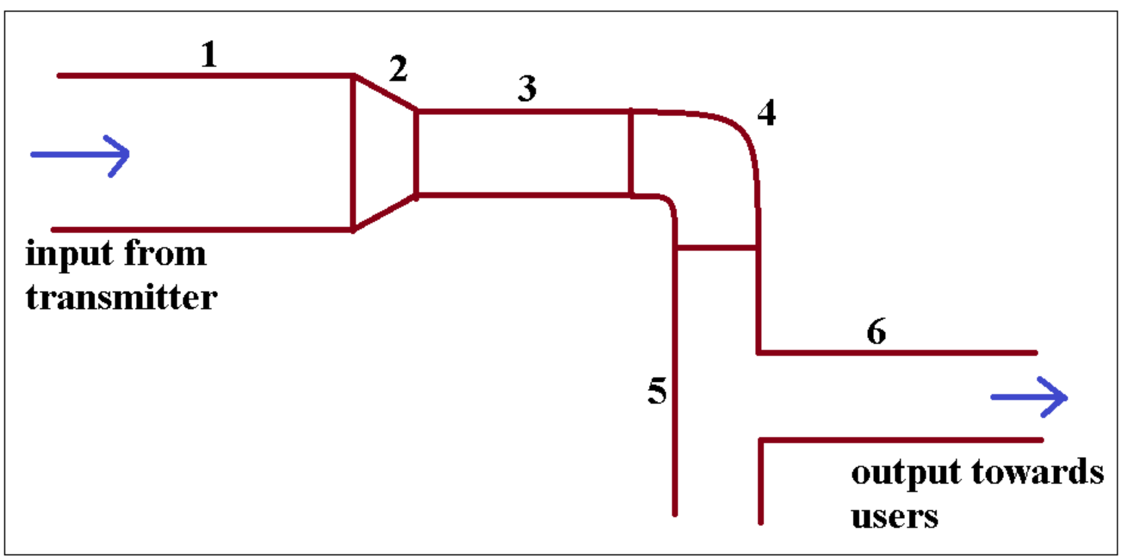

Figure 5.2. HVAC duct system made up of different duct sections

**Straight Sections**

Figure 5.3 shows a straight cylindrical section which forms one of the HVAC duct elements. The section can be described by the length of the straight duct $L_s$ and the radius of the cylindrical section $a$.

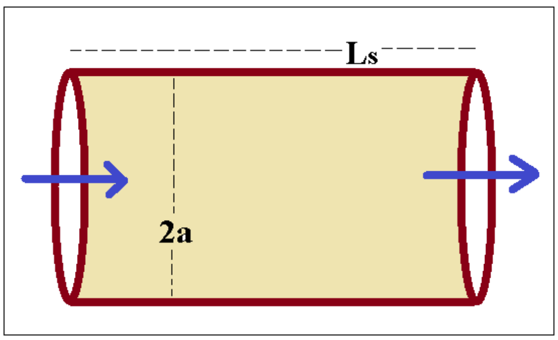


Figure 5.3. Straight HVAC duct section of diameter 2a and length $L_s$

Modes propagating through a straight HVAC duct do not interact with each other as they travel in a straight line, therefore the transfer matrix for such a section can be described as [68]

$$\hat{Q}_S = \begin{bmatrix} e^{-\gamma_1 L_S} & 0 & \dots & 0 \\ 0 & e^{-\gamma_2 L_S} & \dots & 0 \\ . & . & \dots & . \\ 0 & 0 & \dots & e^{-\gamma_U L_S} \end{bmatrix} \tag{5.4}$$

Where $\gamma_u$ is the complex propagation constant of mode $u$ and $U$ is the total number of modes.

In the case of straight sections, the radii $a$ and $b$ are equal and $L_i$ is the length of the duct. Straight sections of ducts do not cause any coupling between the propagating modes and the complex propagation constant is given as $\gamma_i = \alpha_i + j\beta_i$.

**Bends**

Figure 5.4 shows the cylindrical HVAC duct with a bend in it and the parameters used to define it are the curvature radius $R$, the inner radius of the cylindrical duct $a$ and the angle of the bend $\phi_B$.

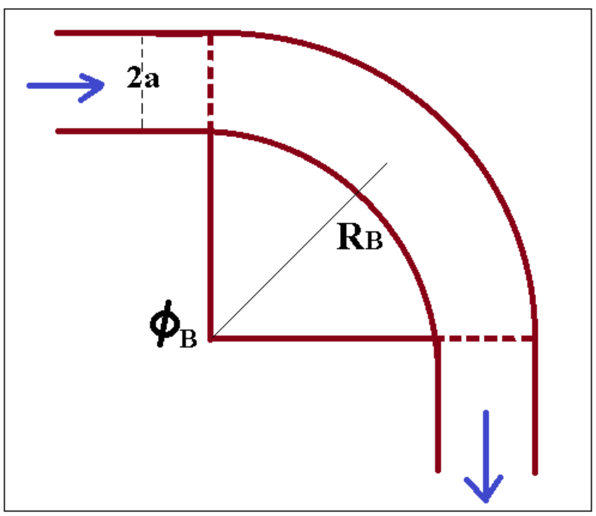

Figure 5.4. Cylindrical HVAC duct with a bend section

Propagation in bends can be modelled using the method of moments [83], dyadic Green's functions [84], or numerical techniques [85]. A circular bend can be treated as a section of toroid, however due to the bend, the electromagnetic fields will be distorted if the bend is too sharp. In case of HVAC duct, the bend is very gentle as $a/R < 1$, therefore it simplifies the consideration of the geometry as a toroid, as the cutoff wave number for each mode in case of bend duct is only slightly different from the wave number in a straight duct. The cutoff wave number $g^B$ of a toroidal mode in a bend is given by [78]:

$$g^B = g\sqrt{1 + \frac{3}{4g^2R^2}} \tag{5.5}$$

Where $g$ is the cutoff wave number of an equivalent $TE$ or $TM$ mode in a cylindrical waveguide. The mode propagation constant $\gamma^B$ in a bend is a function of the cutoff wave number and can be computed directly as

Using the above value of $\gamma^B$, the approximate transfer matrix of a bend can be computed as follows:

$$\hat{Q}_B = \begin{bmatrix} e^{-\gamma_1^B R\phi_B} & 0 & \dots & 0 \\ 0 & e^{-\gamma_2^B R\phi_B} & \dots & 0 \\ . & . & \dots & . \\ 0 & 0 & \dots & e^{-\gamma_U^B R\phi_B} \end{bmatrix} \tag{5.6}$$

Where $U$ is the maximum number of propagating modes. Through the propagation constant, characteristic impedance of the modes can be calculated which reflects the amount of reflection that mode will suffer.

A duct with a bend of angle $\phi$ can be considered as a section of a toroid. Therefore, the complex propagation constant in a bend $\gamma_n^B$ can be expressed via cutoff wavenumbers of toroid eigenmodes. As the ratio of waveguide radius and the bend radius will always be less than one, the bend can be considered as a gentle bend and the mode conversion effects can be neglected. Again, the radii $a$ and $b$ are equal, but the length $L_i$ is now replaced by $L_i = R\phi$ where $\phi$ is the angle of the bend and $R$ is its center radius. The duct of shape U can be considered as a special case of a duct with an angle $\phi$ where $\phi = 180°$.

**Tapers**

Figure 5.5 shows the cylindrical HVAC duct with a tapered element. The parameters of the taper are length $L_{T_p}$ and the two end radii: $a$ and $b$.

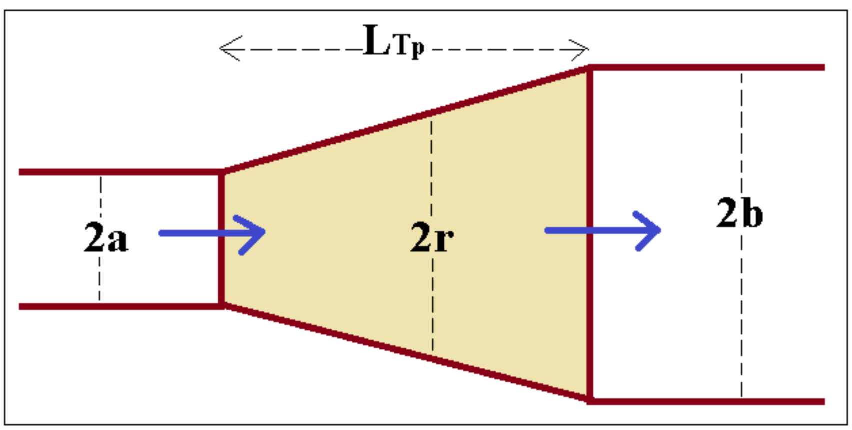

Figure 5.5. Cylindrical duct with a tapered duct element in between two straight duct sections

A gentle taper can be considered as cylindrical waveguide with a changing radius. Due to the change in the radius, the fields might gradually change, however due to the gentle taper, no mode coupling takes place.

If the diameter changes gradually in comparison to the guide wavelength $\lambda_g$ of the mode, then the taper will be considered as a gentle taper. Consider that the signal is introduced in the duct from the side where the radius $a$ is smaller, then the number of modes that travel towards the section with the larger radius $b$ is the same as the number of modes entering through radius $a$. Using the power conservation rule, the total power flowing into the smaller radius must be equal to the total power coming out through the larger radius:

$$p_u^a |C_u^a|^2 = p_u^b |C_u^b|^2 \tag{5.7}$$

It follows that:

$$a^4 \beta_u^a |C_u^a|^2 = b^4 \beta_u^b |C_u^b|^2 \tag{5.8}$$

Where $\beta_u^a$ and $\beta_u^b$ are the phase propagation constants for mode $u$ propagating through a waveguide of radii $a$ and $b$, respectively. Using the above equation, we can calculate the change in the amplitude of the mode coefficient when the mode is propagating through the taper:

$$|C_u^b| = \frac{a^2}{b^2} \sqrt{\frac{\beta_u^a}{\beta_u^b}} |C_u^a| \tag{5.9}$$

Further, each mode also suffers the amplitude and phase attenuation while going through the waveguide. The propagation constant $\beta_u$ for mode $u$ is a function of the radius $r, 0 \leq r \leq a$, of a cylindrical waveguide as

$$\beta_u(r) = k\sqrt{1 - \frac{g^2a^2}{k^2r^2}} \tag{5.10}$$

Where $g$ is the mode cutofff wave number. The attenuation constant $\alpha_u$ of mode $u$ depends on the radius $r$ of a cylindrical waveguide as [68]

$$\alpha_u(r) = \frac{R_s}{\eta a}\frac{k}{\beta_u(r)} \times \begin{cases} \frac{c^2g^2a^2}{\omega^2r^2} + \frac{n^2}{g^2a^2 - n^2} & if\ TE \\ 1 & if\ TM \end{cases} \tag{5.11}$$

The radius of the taper varies linearly with respect to the position $z\ \left(0\ \leq z \leq L_{T_P}\right)$ of the taper in the duct:

$$r(z) = a + (b - a)\frac{z}{L_{T_P}} \tag{5.12}$$

The total complex propagation constant for each mode $u$ can be found by integrating the complex sum of the attenuation and phase constant calculated over the length of the taper as:

$$\gamma_u^T = \frac{1}{L_{T_P}} \int_0^{L_{T_P}} \gamma_u(z) \partial z = \frac{1}{b-a} \int_a^b \gamma_u(r) \partial r \tag{5.13}$$

Where $\gamma_u = \alpha_u + j\beta_u$ is the propagation constant for a mode $u$ in a cylindrical duct. Using the definitions mentioned above, we can define the transfer matrix of a taper as [68]

$$\hat{Q}_{T_P} = \frac{a^2}{b^2} \begin{bmatrix} \sqrt{\frac{\beta_1^a}{\beta_1^b}} e^{-\gamma_1^T L_{T_P}} & 0 & \dots & 0 \\ 0 & \sqrt{\frac{\beta_2^a}{\beta_2^b}} e^{-\gamma_2^T L_{T_P}} & \dots & 0 \\ . & . & \dots & . \\ 0 & 0 & \dots & \sqrt{\frac{\beta_U^a}{\beta_U^b}} e^{-\gamma_U^T L_{T_P}} \end{bmatrix} \tag{5.14}$$

Where $U$ is the maximum number of propagating modes.

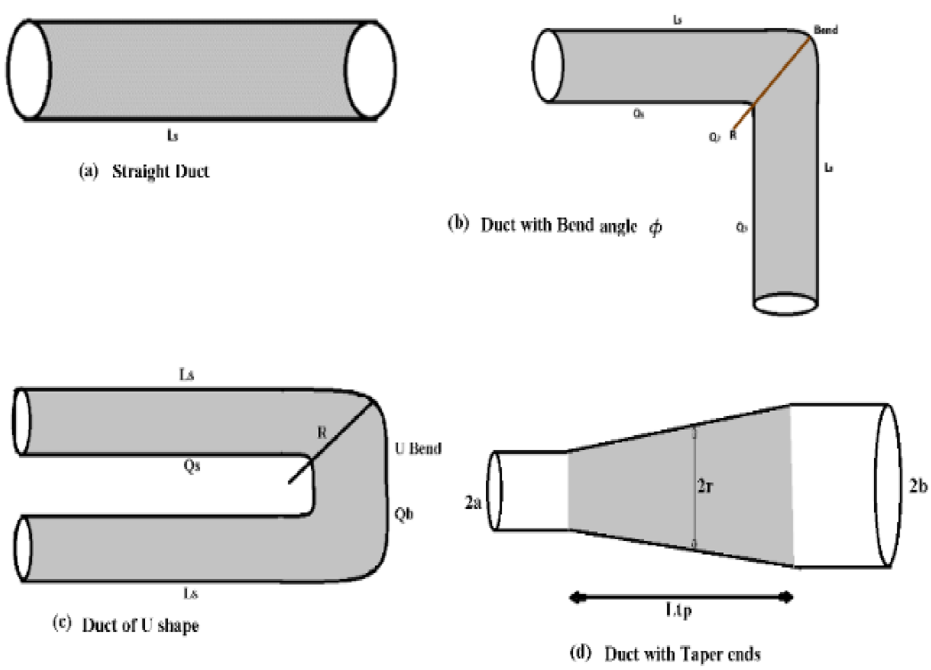


Figure 5.6. HVAC Duct (a) straight (b) with bend angle $\phi$ (c) shape U (d) with taper ends

In order to characterize the HVAC duct channel, it is important to know its frequency response and the received signal associated with it. Figure 5.7 and Figure 5.8 depict the theoretical RSSI values obtained using (5.1) and (5.3) for ducts of lengths 4 m and 8 m respectively with bend angles 0° (straight),45°,90°,180° (U shape) and with matched loads on both ends ($\Gamma$=0), a diameter of 12.7 cm, and when the duct is excited by an antenna of dimension $l \approx$ 1mm ($\lambda/4$).

In Figure 5.7 we can see that the RSSI varies with the shape of the ducts and is maximum (around -32 dBm) for a straight duct and subsequently decreases for the different bend angle. However, the loss in the received signal strength due to the severe bends as in the U shape is also around -40 dBm.

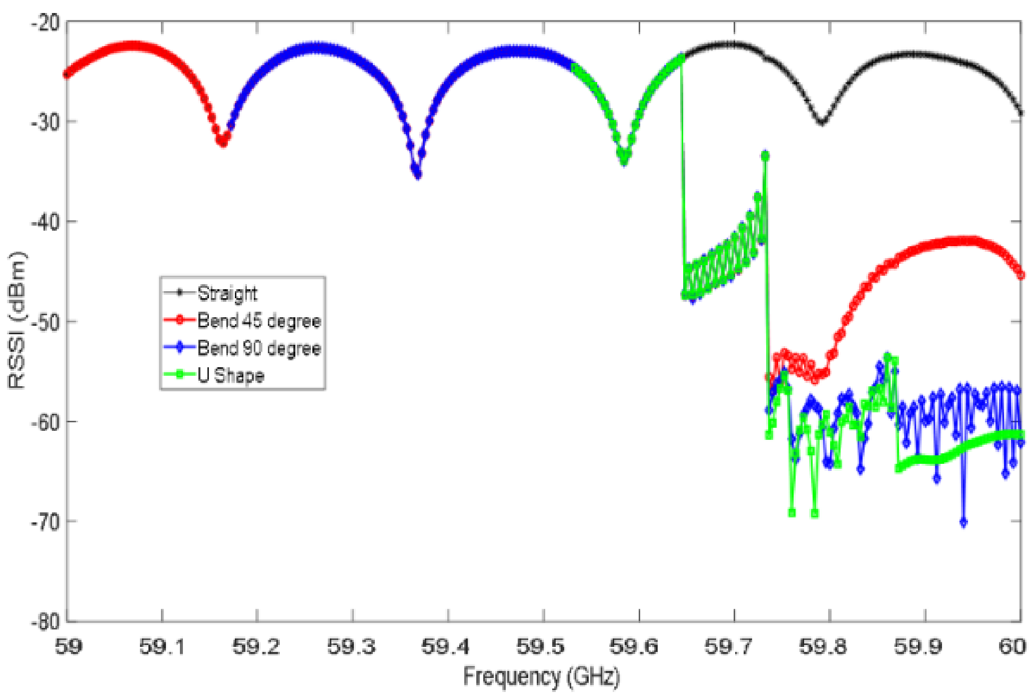

Figure 5.7. Theoretical RSSI for cylindrical HVAC duct of diameter 12.7 cm and length 4 m

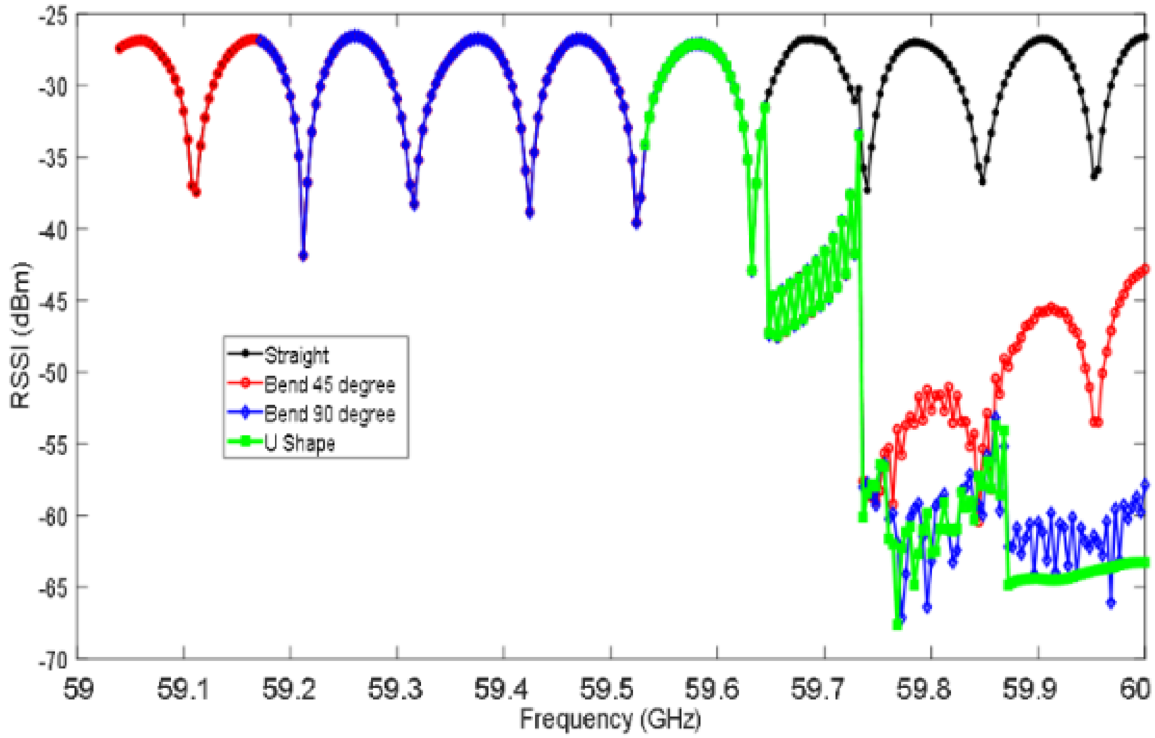

Figure 5.8. Theoretical RSSI for cylindrical HVAC duct of diameter 12.7 cm and length 8 m

In Figure 5.8 we can see a slight decrease in the RSSI values for all the duct shapes. However, when comparing these results to the free space path loss (72 dB), we observe that the results are around 30 dB higher for the maximum bend angle 180° (U shape). The drastic change in the theoretical RSSI values for the bent HVAC ducts of different shapes, is due to the effect of the bend angle on the propagation constant at the cut-off frequency.

# CHAPTER 6

# IMPULSE RESPONSE AND POWER DELAY PROFILE

Authors – Esha Bangar, Nima Taherkhani, Kamran Kiasaleh

The Department of Electrical and Computer Engineering, EC33

The University of Texas at Dallas

800 West Campbell Road

Richardson, Texas 75080-3021

“Reproduced from [E. Bangar, N. Taherkhani and K. Kiasaleh, "Characterization of Indoor Heating, Ventilation and Air Conditioning Duct System as a Communication Channel at 60 GHz," 2020 IEEE Texas Symposium on Wireless and Microwave Circuits and Systems (WMCS), 2020, pp. 1-7, doi: 10.1109/WMCS49442.2020.9172409.]”

## 6.1 Introduction to Dispersion in HVAC

As the HVAC duct channel's propagation characteristics depend on the duct dimensions, duct material, antenna parameters, coupling of the antenna, and the propagation frequency. Therefore, these parameters also affect the channel's transfer function and impulse response. These fundamental parameters can be grouped as coupling, dispersion and attenuation present in the HVAC duct. As the different dimensions of the antenna and the HVAC duct leads to the difference in the excited mode distribution and in the reception of the excited modes, which affect the impulse response. The attenuation results due to the finite conductivity of the duct walls and losses due to each reflection from the non-uniformities in the duct system. Also, since the different components of the electromagnetic radiation signal travel different paths therefore reach at the receiver at different times, which results in dispersion. There are three different types of dispersion in the HVAC duct system: intramodal, intermodal, and multipath dispersion. As the impulse response for a free space mm-wave channel has been studied, in this chapter we want to look at the impulse response of the HVAC duct channel and compare it to that of the free space channel's impulse response and the power delay profile. The chapter also includes the details on the other physical mechanisms that affect the impulse response of an arbitrary HVAC duct system.

## 6.2 Impulse Response of HVAC Channel

Once the channel frequency response $H(f)$ is obtained, we can get the channel impulse response (CIR), $h(\tau)$, by using the inverse discrete Fourier transform, as $h(\tau) = IFFT(H(f), N)$ where $\tau$ is the delay of the received signal, and $N$ is the number of the measured frequency points [69]. For a time-invariant channel, such as the HVAC duct channel, the bandlimited channel impulse response can be obtained using [36], [56], [71]

$$h(\tau) = \sum_{n=1}^{N} A_n \delta(\tau - \tau_n) \exp(-j\psi_n) \tag{6.1}$$

where $\delta(.)$ is the Dirac-delta function. Furthermore, $A_n$, $\psi_n$ and $\tau_n$ denote the amplitude, phase, and delay of the $n^{th}$ path, respectively.

## 6.3 Power Delay Profile

A multipath channel can be characterized by power delay profile which relates the power strength of the different multipath signals along with their arrival times. Detecting the different multipath signals and recording their exact arrival times in time domain will require 60 GHz mm-wave devices of very high sampling frequency and are very expensive. An alternative way is to transform the channel frequency response to the impulse response using inverse fast Fourier transform (IFFT) and calculate the power delay profile through the impulse response.

Power delay profile $p(\tau)$ is related to the channel impulse response $h(\tau)$ as [56], [70], [71], [86]:

$$p(\tau) = |h(\tau)|^2 \tag{6.2}$$

The power delay profile can be described in terms of the frequency-dependent radiation resistance and the mode attenuation constants due to the geometry of the antenna and the dimension of the HVAC duct. The attenuation constants for the waveguide modes are calculated based on the attenuation due to the duct walls, therefore, mode attenuation constants depend on the mode type ($TE$ or $TM$), mode indices ($n$ and $m$), and frequency. Further, attenuation defines the rate at which the modes decay during the propagation. In a straight duct, the mode power reduces exponentially with the distance that the mode travels. Therefore, the path length can be related to the time via mode velocity and obtain an upper bound of the power delay profile shape for mode $n$ as [59]

$$p_n(t) = p_n(t_0)e^{-2\alpha_n v_n (t-t_0)} \tag{6.3}$$

Where $t_0$ is the time of the first arrival and $v_n$ is the group velocity of mode $n$ in the HVAC duct.

## 6.4 RMS Delay Spread

We can determine RMS delay spread from the power delay profile, which is one of the important parameters to characterize the temporal dispersive properties of multipath channels. The RMS delay spread is the power weighted standard deviation of the mean excess delays and is given by the square root of the second central moment of the power delay profile. RMS delay spread is a representative parameter for the analysis of time dispersion and provides a measure of the variability of the mean delay. It can be computed as [56], [57]

$$\tau_{RMS} = \sqrt{\overline{\tau^2} - \bar{\tau}^2} \tag{6.4}$$

Where $\bar{\tau}$ is the mean excess delay and is given as $\bar{\tau} = \frac{\sum_i \tau_i \cdot p(\tau_i)}{\sum_i p(\tau_i)}$, and $\overline{\tau^2} = \frac{\sum_i \tau_i^2 \cdot p(\tau_i)}{\sum_i p(\tau_i)}$, $\tau_i$ and $p(\tau_i)$ are the delay and power of the $i^{th}$ path respectively. RMS delay spread is typically computed using only values above a certain threshold with respect to the maximum signal level in the impulse response. In our analysis, we use a threshold of -20 dB, which is typically used in the literature. It is important to understand the relation between the HVAC duct parameters, such as $(L, L_1, L_2, \Gamma)$, on the RMS delay spread, especially for long HVAC ducts. However, given the size of commercial HVAC ducts, collecting experimental data for long distances is difficult. The impulse response model, however, allows prediction of the RMS delay spread behavior for any distance. Usually in indoor communication, the RMS delay spread increases linearly with the distance and is further impacted by the presence of the multipath. However, in the case of HVAC ducts, the specific slope of the RMS delay spread curve strongly depends on the modes travelling through the duct.

### 6.5 Dispersion

Dispersion is one of the important mechanisms that affect the HVAC duct channel impulse response. The amount of dispersion encountered depends on the number and relative amplitudes of propagating modes and usually is nonlinear with respect to frequency. Dispersion in single mode waveguides is called intramodal dispersion, which arises because the phase velocity of the mode travelling through the waveguide varies nonlinearly with the wavelength. The mode group velocity is given by [71]

$$v_n = c\sqrt{1-\left(\frac{\omega_c}{\omega}\right)^2} \tag{6.5}$$

The arrival time delay for distance $L$ can be calculated as $t_a = L/v_n$. To analyze the intramodal dispersion, we have assumed that only one mode, *i.e.,* $\mathrm{TM}_{3,17}$, is propagating through the HVAC duct. We have chosen this mode as it has the maximum percentage of total power of all the modes travelling through the duct. We have also assumed that there are no multipath reflections from the terminated loads while calculating intramodal dispersion.

The dispersion in multimode waveguides is called intermodal dispersion. It arises due to the fact that the different modes in the waveguide are frequency dependent, and, therefore, travel with different velocities. To analyze the intermodal dispersion, we assume that all the modes present in the waveguide at 60 GHz are travelling through the HVAC duct and that there are no multipath reflections from the terminated ends.

Multipath dispersion is because the signal gets reflected several times from the nonuniformities on the duct surface. In presence of strong multipath reflections, there will be distinct periodic peaks in the power delay profile. Further the intramodal dispersion will lead to spreading of these peaks. Therefore, at a short distance, multipath dispersion contributes most to the RMS delay spread. RMS delay spread decreases on decreasing the reflection coefficients of the ends. On the other hand, on increasing the distance, intermodal dispersion becomes the dominant contributor.

Figure 6.1 shows the calculated power delay profile using (6.2) in case of a single mode TM3,17 being transmitted through the HVAC duct. Therefore, the power delay profile in Figure 6.1 accounts for intramodal dispersion present in the HVAC duct of the length 5 m and diameter 12.7 cm. We have used TM3,17 mode as it consists of 80% of the total power present in all the modes, and, therefore, the dispersion suffered by this mode will be the largest. From Figure 6.1, we can see that the RMS delay spread when only one mode is travelling through the HVAC duct is 4.56 ns, which is considerably small for a distance of 5 m at 60 GHz.

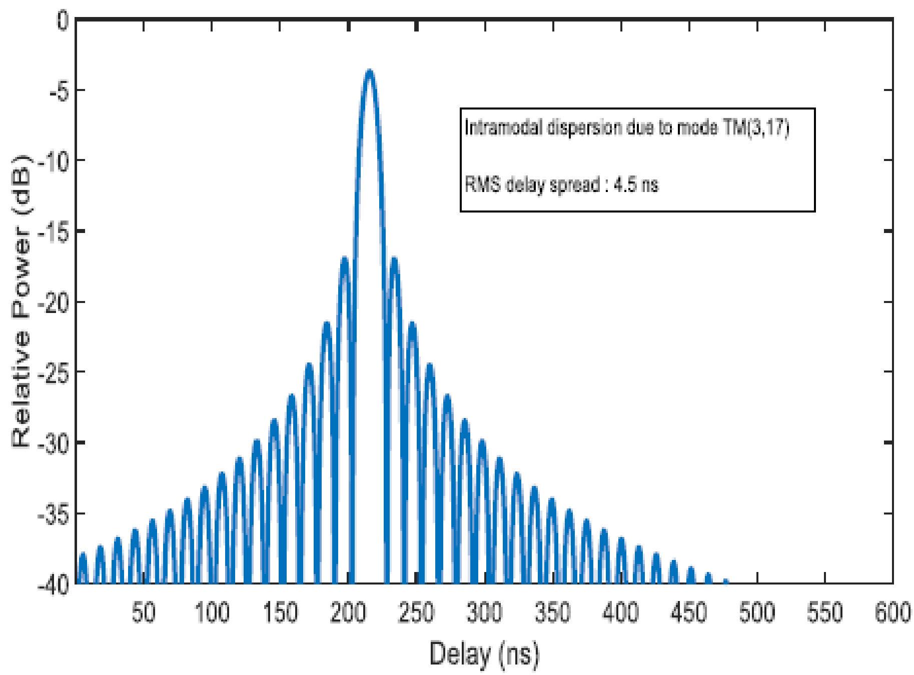

Figure 6.1. Theoretical PDF for cylindrical HVAC duct of length 5 m

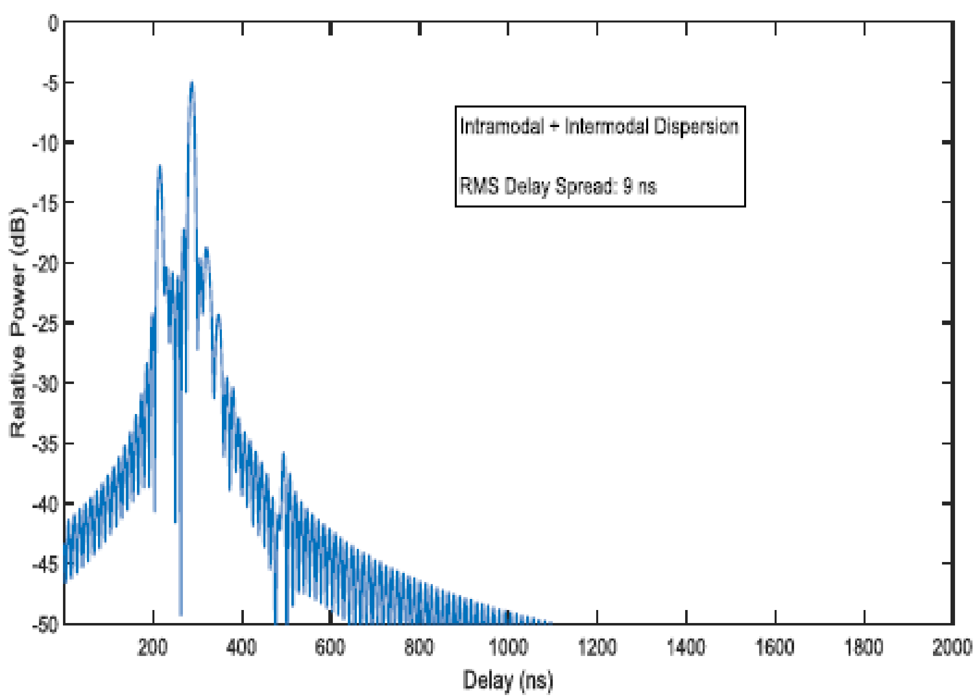

Figure 6.2. PDF for straight HVAC of length 5 m with no end reflections, i.e., $\Gamma_1 = \Gamma_2 = 0$

Figure 6.2 shows the calculated power delay profile (PDF) using (6.2) and considering that all the modes present in the waveguide are transmitted through the HVAC duct. Figure 6.2 shows the intermodal and intramodal dispersions which arise due to the difference in the velocities of all the modes present in the HVAC duct of length 5 m and diameter 12.7 cm. The RMS delay spread for this case is around 9 ns. As compared to the RMS delay spread values, *i.e.,* 20 ns obtained in similar dimension [55]-[57] these results show that HVAC ducts have 50% less delay spread, as there are absolutely no obstructions in the signal path when travelling through the ducts.

Figure 6.3 shows the power delay profile calculated using (6.2) and shows the combined effects of the intermodal, intramodal and multipath dispersion present in the HVAC duct of the length 5 m and diameter 12.7 cm. The results are obtained by considering that all the modes are travelling through the duct and that heavy reflections ($\Gamma_1 = \Gamma_2 = -0.9$) is present due to the loads. The RMS delay spread for this case is around 240 ns. The results show that due to the reflections, the number of paths increases leading to a large delay spread. Since the end loads present such high reflection coefficients, the results shown here depict the worst-case scenario.

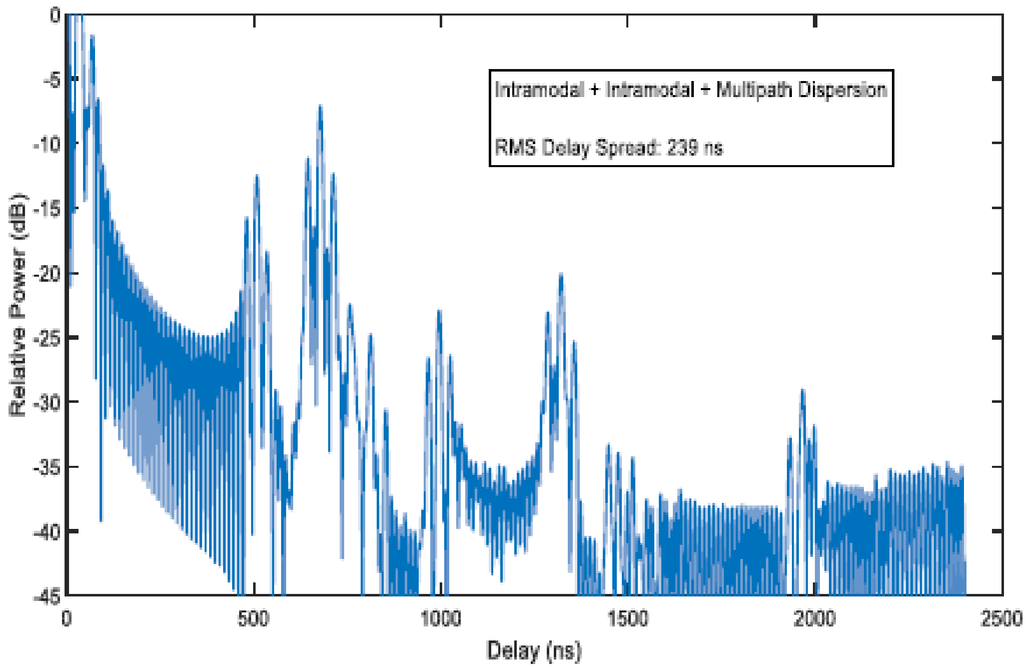

Figure 6.3. PDF for straight HVAC of length 5 m with end loads, i.e., $\Gamma_1 = \Gamma_2 = -0.9$

Figure 6.4 shows the variation of RMS delay spread calculated using (6.4) with the length of the HVAC duct. The RMS delay spread increases linearly for short distances but then becomes flat as the distance increases. At distances less than 35 m, a large number of modes travel through the HVAC duct, which leads to increased intramodal and intermodal dispersions. Subsequently, we get a large delay spread. Between 35 m to 55 m, very few modes travel through the duct (channel attenuation is around 35 dB), which leads to a decrease in the intermodal dispersion (hence, smaller delay spread increase). However, a further increase in the distance leads to a channel attenuation of 45 dB. The intramodal dispersion in the modes and intermodal dispersion between the remaining modes increases, thereby leading to an increase in the delay spread.

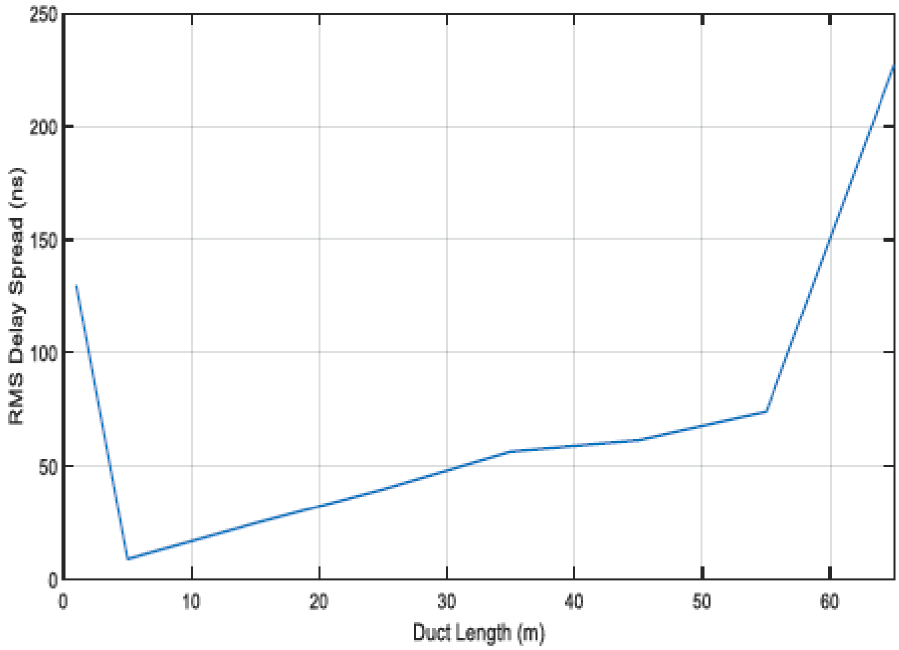

Figure 6.4. RMS delay spread of HVAC duct with no end reflections, i.e., $\Gamma_1 = \Gamma_2 = 0$

## 6.6 Coherence Bandwidth

Coherence bandwidth $B_c$ can be estimated from the RMS delay spread with 50% signal correlation as:

$$B_c = \frac{1}{5\sigma_\tau} \qquad (6.6)$$

## 6.7 Discussion

A simple mechanism for the distribution of mm-wave signals using HVAC ducts in an indoor environment was proposed. It was shown that high data rates were possible using the mm-wave signals that are typically severely attenuated due to physical barriers. Channel frequency responses for the duct system with duct bend angles of 0°,45°,90° and 180° and lengths of 4 m and 8 m were obtained, and the results show RSSI values ranging from -30 dBm to -50 dBm, which are above the receiver's sensitivity (-70 dBm) and are considerably high as compared to the free space path loss for the same distances. We calculated the dispersion encountered by the duct system and observed RMS delay spreads on the order of 9 ns for a distance of 5 m, which is very low compared to the data (20 ns) in the available literature. Further, the presence of HVAC ducts in every building lead to a low-cost installation of the proposed system, making the presented study viable for many residential and office environments.

# CHAPTER 7

# RAY TRACING

Authors – Esha Bangar, Kamran Kiasaleh

The Department of Electrical and Computer Engineering, EC33

The University of Texas at Dallas

800 West Campbell Road

Richardson, Texas 75080-3021

“Reproduced from [Esha Bangar and Kamran Kiasaleh, "Evaluating Performance of Heating, Ventilation & Air Conditioning Duct Communication Channel at 60 GHz Using Ray Tracing," Progress In Electromagnetics Research C, Vol. 113, 177-195, 2021. doi:10.2528/PIERC21040906]”

## 7.1 Background of Ray-Tracing Techniques

Authors in [88] present a comprehensive review on ray-tracing (RT) techniques, focusing on the fundamental concepts and practical ray tracing algorithms. The paper describes the ray concept, ray propagation phenomenon such as line-of-sight, reflection, transmission, diffusion, and scattering. Different ray-tracing algorithms, such as Fermat's principle, image-method, shooting and bouncing rays and hybrid methods are discussed as part of this review paper. Authors also present the different categories of accelerator algorithms for the ray-tracing, such as space-division, 2-dimensional simplification, and graphic process unit (GPU) acceleration. In [87], researchers used RT simulation to find the channel properties for indoor communications. Authors used the results of RT to define a deterministic channel impulse response. The authors in [90] defined the channel propagation for a tunnel using an RT algorithm and calculated the path-loss (PL) for different shapes of tunnels based on the ray-tracing technique. Due to the similarities in the tunnel and the HVAC duct environment, the results of this paper are used here to analyze an HVAC channel. Channel propagation for a tunnel was also explored by authors in [89] using the Scattering and Bouncing Ray (SBR) algorithm and calculations for electromagnetic loss based on the Fresnel's law and UTD (Uniform Theory of Diffraction) were also performed. The authors described a novel 3D simulator called RayLA using JAVA library and Java open graphics library (JOGL) for the SBR algorithm. The study compares the experimental results to the ray-tracing simulations performed for the tunnel at 2.4 GHz.

The study in [51] evaluated the performance of beamforming techniques in multi-user indoor environment at the mm-wave frequency band using both measurements and RT simulations. Channel impulse response was measured and subsequently power level for the received signals was calculated for different locations of the receiver in a 21 m × 21 m room. Based on these measurement results, various beam forming schemes were adopted, resulting in a beam search algorithm. Further, results of the experiment were compared to the results of a custom 3D ray-tracing simulator. Authors proved that ray-tracing is a reliable directional channel model for beamforming assessment and for real-time assistance in the beam-searching phase.

The paper in [41] investigated the system level performance of mm-wave 60 GHz channels by simulating a realistic living room scenario considering the effects of human shadowing and three different types of antennas. Authors measured the channel impulse response (CIR) using a 3-dimensional (3D) RT method. The results were then fed to a channel simulator to generate the performance figures. Authors showed that it becomes eminently challenging to maintain the communication link due to the obstruction of the LOS or due to the presence of multiple strong reflection paths using an omnidirectional antenna. It was suggested to incorporate directional antenna with high gain capable of performing beamforming for the 60 GHz indoor communication systems. In [23], a millimeter wave quasi-deterministic (Q-D) channel model for an in-room access scenarios was developed with double-directional channel measurements using a custom developed channel sounder at 58.5 GHz. From the measured data, the multi-path components were extracted, and an intra-cluster model was developed based on the actual physical propagation paths to identify the scattering processes explicitly on the rough surfaces. Ray-tracing simulations were performed and compared to the experimental results and authors found them to be similar.

Several other authors [22], [24]-[27], [37], [44], [58], [91]-[93] performed extensive channel sounding experiments for millimeter wave channels in case of indoor communication environments, calculated the channel impulse response, and characterized the path loss for the different transmitter and receiver separations, human blockage, obstructions in the form of walls, cabinets, and furniture. Authors in [44] also considered polarimetric diffuse scattering channel model and recorded the channel measurements at 26 GHz and 60 GHz. As the indoor environment can have several rough surfaces and edges, and when the signal impinges on these surfaces scattering will take place, the authors explored the polarimetric diffuse scattering channel measurements. Phased arrays were utilized by the authors in [25] to estimate the ray paths with the knowledge of beam patterns of the phased arrays. Authors also performed ray-tracing simulation to verify the results at mm-wave frequencies.

Since experimental measurements are not always feasible due to the high cost of mm-wave transceivers, authors in [36], [57], [94]-[102] have also described various ray-tracing simulations based on SBR/IM. Ref. [95] presents the propagation characteristics of mm-wave signals in the indoor radio channel based on the method of shooting and bouncing ray tracing/image method and analyzed the path-loss models, received power and the root-mean-square delay spread. The paper also considers the line-of-sight and non-line-of-sight (NLOS) scenarios and observes a path-loss exponent of 3.87 for NLOS scenario. Authors in [96] performed a research on the transmission coverage area using ray-tracing simulations for a train compartment and an indoor conference room. The transmitter was mounted on the ceiling and the maximum transmitter-receiver separation distance considered was 8 m for which the received signal is recorded to be -100 dBm.

To validate the viability of HVAC duct as a communication channel, a precise study of the radio propagation channel should be performed. One way to evaluate the HVAC duct channel characteristic is to measure the CIR for various duct shapes and lengths. However, the ability to obtain the CIR is limited because these measurements will be specific to the duct structure. Also, measurements can be expensive in the mm-wave band as compared to the electromagnetic simulation approaches, such as RT. RT simulations are widely adopted to estimate radio channels for tunnels, trains, and other indoor environments, alleviating the burden of extensive field measurements. Through the application of a reliable 3D RT approach, we can obtain many useful physical parameters such as the angle of arrival, angle of departure, complex amplitude and delay of each multipath component. Acquiring such parameters through experimental measurements are generally tedious. Moreover, the antenna pattern and mutual coupling effects can be easily incorporated in the RT simulation. These capabilities make the RT approach a powerful tool to predict channel path-loss and to calculate parameters such as SNR, EVM, and BER. Two major methods of implementing 3D RT are image theory and SBR. For uniform structures such as HVAC ducts, RT via image theory will be easier to implement, and will lead to a reduction in the simulation time.

In this study, we developed a RT simulator based on image theory using MATLAB to study the mm-wave HVAC duct communication channel. Our simulator incorporates antenna beam-width to estimate the accurate number of rays being launched. We also include an attenuation component to represent atmospheric losses due to the temperature and moisture present in the air flowing through the HVAC ducts. The consideration of the printed half-wave dipole antenna is motivated by the fact that such antennas provide large gain over a wide bandwidth and lend themselves to easy system integration. The simulation accuracy is verified with the comparison between simulated and measured experiment data using the Tensorcom WiGig compliant chipsets. The simulator is designed to specifically work only for mm-wave frequencies and for symmetrical structures to reduce the simulation time considerably.

### 7.2 Ray-Tracing using Image Method

The RT method adopted in this paper is based on the ray optics which aim at solving Maxwell's equations with the assumption of operation limited to the mm-wave frequency band. This assumption has a crucial effect due to the large dimension of the HVAC duct compared to the wavelength of the mm-wave band. The RT image theory method uses less computer memory due to the symmetrical structure of the HVAC duct. We note that the number of incident rays and the angle of incidence depends on the beam-width of the printed dipole antenna. We consider the transmitter with a printed half-wave dipole antenna with a beam-width of $\pm 30^{\circ}$. The circular opening of the HVAC duct is divided into a 2D mesh with equidistant points and the distance of the transmitter from the duct opening is fixed as $\delta_{Tx}$ as this distance is going to be very small compared to the length of the HVAC duct ($\delta_{Tx} \cong 0$). Assume that a cone of angle 60° is drawn with the transmitter at the vertex of the cone and the vertex is a distance of $\delta_{Tx}$ from the base (see Figure 7.1). Then, the points on the mesh which lie inside the cone base will be individual ray points.

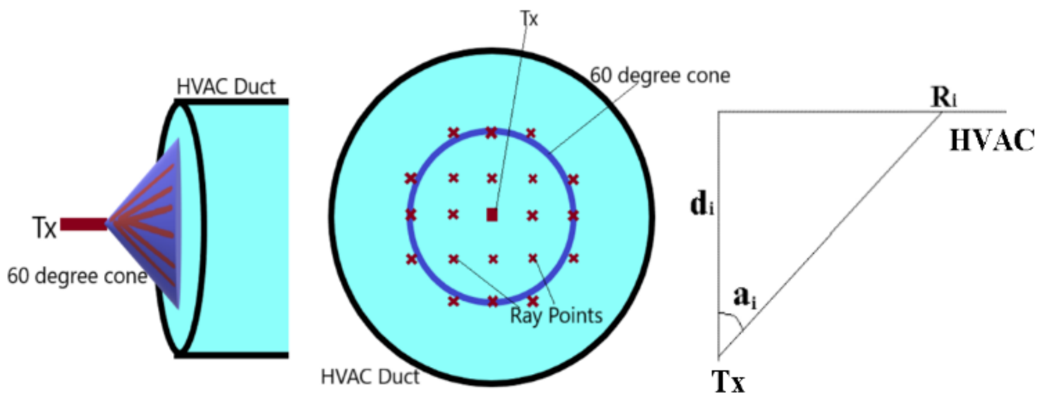

Figure 7.1. Mesh and ray points on HVAC duct with transmitter antenna beamwidth

For the MATLAB program, we draw a mesh on the circular opening of the HVAC duct and assign angles to each mesh point as ($-30°: 1^{\circ}: 30^{\circ}$). Each mesh point is also associated with the vertical distance from the HVAC duct walls. Using the angle $a_i$ and the distance $d_i$ (the vertical distance between the mesh point $i$ and the HVAC duct wall), the reflection point $R_i$ on the HVAC duct walls is calculated as $R_i = d_i \tan(a_i)$. As the beamwidth of the antenna and the distance of the transmitter from the HVAC duct is fixed, we form a look-up-table for the individual rays consisting of the ray's incident angle and the distance of the ray's first reflection point from the transmitter. Making use of the symmetry of the HVAC duct, we can say that the incident and the reflected angles made by any ray will always be same.

The trajectory of the reflected rays is determined through the image method and Fermat's principle of the least time. The Fermat's principle states that a ray will travel from the transmitter to the receiver through a path, which will require the least possible time. Further using image method, we consider that a ray launched by the transmitter $T_x$ will reach the receiver $R_x$ after reflection from the duct boundary if the image of the transmitter $T_x^i$ (superscript "$i$" represents the transmitter image outside the HVAC duct) can be connected to the receiver through a straight line, as shown in Figure 7.2. In this case, the image $T_x^i$ is considered as a new transmitter. The same process can be applied to find the ray path with multiple reflections. The recursive procedure is implemented efficiently using MATLAB. All the rays launched by the transmitter will always reach the receiver due to the symmetrical structure of the HVAC duct. However, the rays will have different path lengths, phase angles, and delays. Moreover, the electric field strength is reduced due to the reflection from the HVAC duct walls as the ray progresses. Therefore, the magnitude of the reflected field is determined by Fresnel's equation whereas the propagation direction is determined by the law of reflection. Unlike theoretical and empirical models, the RT method does not provide simple formulas for the calculation of path loss. Hence, one has to resort to theoretical calculation of path loss based on the value of the average pointing vector obtained from ray-tracing simulation and the effective area of the transmitting and receiving antenna.

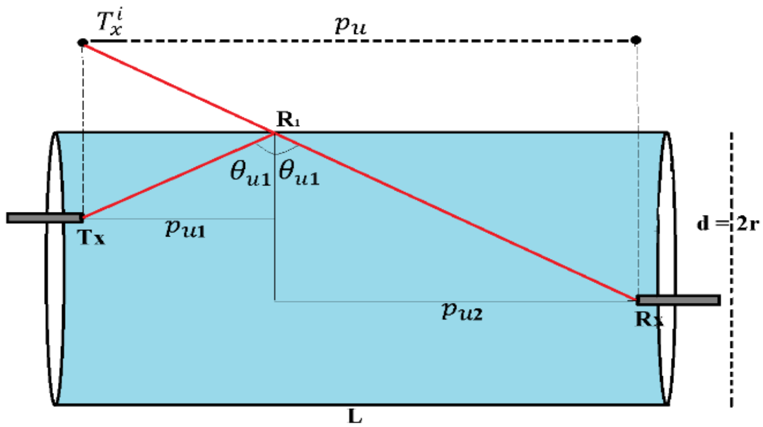


Figure 7.2. Ray tracing with image method for HVAC duct

### 7.3 Implementation of Ray-Tracing Algorithm

We consider a HVAC duct of diameter $d$ (radius $r = d/2$) and the length $L$ for the implementation of ray tracing. Let the coordinates of $T_x$ and $R_x$ be $(x_T, y_T, z_T)$ and $(x_R, y_R, z_R)$, respectively. In order to calculate the distance of the subsequent reflection points (reflections made by the rays after the first reflection) from the transmitter and the angles which will be made at these reflection points, we designed the following process. The projection of the direct path from the transmitter to the receiver on the upper duct wall is represented by $p_u$ and on the lower duct wall is represented by $p_l$. In the case of a straight HVAC duct, $p_u = p_l$. Consider a ray which has one reflection point $R_1$ between the transmitter $T_x$ and the receiver $R_x$. The distance between the transmitter image $T_x^i$ and $R_1$ is assumed to be $p_{u1}$ and the distance between $R_1$ and the receiver $R_x$ is assumed to be $p_{u2}$. Therefore, $p_u = p_{u1} + p_{u2}$. The incident and reflected angles which the ray makes with the upper duct wall will be the same and is given as

$$\theta_{u1} = \arctan\left(\frac{p_{u1}}{d - z_T}\right) = \arctan\left(\frac{p_{u2}}{d - z_R}\right) \quad (7.1)$$

From (7.1), we get,

$$\tan(\theta_{u1}) = \frac{p_u}{2d - z_T - z_R} \approx \frac{p_u}{2d - 2z_T} \quad (7.2)$$

The circular dimension of the HVAC duct will be very small compared to the length of the duct. However, the wavelength of the mm-wave is even smaller when compared to the circular dimension of the HVAC duct. Therefore, the difference between the height of the transmitter and the receiver inside the duct will be fairly small, *i.e.*, $z_T - z_R = \delta$ can be ignored[1].

If a ray is reflected twice, once from the upper wall at $R_1$ and then from the lower wall at $R_2$, then $p_u$ can be divided into three parts as $p_u = p_{u1} + p_{um} + p_{u2}$ (following the same approach as one reflection case, see Figure 7.3).

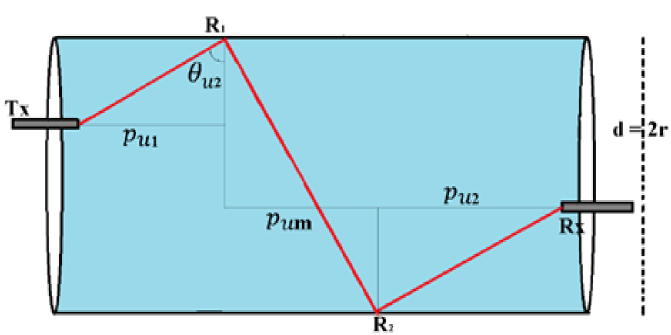


Figure 7.3. Ray tracing with two reflections inside the HVAC duct

[1] Here, the distance of the point $R_1$ from the transmitter is given by the denominator as $r_1 = 2d - 2z_T$.

The angle which the transmitted wave makes with the normal to the upper duct wall is represented as $\theta_{u2}$. Further this angle will be the same as the angle which the reflected wave will make with the normal to the lower duct wall and so on. Therefore, the tangent of the angle $\theta_{u2}$ for the distance $p_{u1}$ between the transmitter $T_x$ and the reflection point $R_1$ is given by

$$\tan(\theta_{u2}) = \frac{p_{u1}}{d - z_T} = \frac{p_{um}}{[d - z_R + z_R]} = \frac{p_{u2}}{z_R} \tag{7.3}$$

From (7.3), we get,

$$\tan(\theta_{u2}) = \frac{p_u}{2d - z_T + z_R} \approx \frac{p_u}{2d} \tag{7.4}$$

The last part of (7.4) is calculated using $z_T - z_R = \delta \ll d$. Following the above approach, we calculate the incident angle for a ray that gets reflected $n$ times. We consider that an upward-directed ray makes an angle $\theta_{un}$ and a downward-directed ray makes an angle $\theta_{ln}$ at each reflection point. Then, the tangent of these angles is given, respectively, as

$$\begin{aligned} tan(\theta_{un}) &= \frac{p_u}{r[1 + 2n - (-1)^n] + \mathrm{z}[(-1)^n - 1]} \\ tan(\theta_{ln}) &= \frac{p_l}{r[-1 + 2n + (-1)^n] + \mathrm{z}[(-1)^{n+1} + 1]} \end{aligned} \tag{7.5}$$

The distance of the $n^{th}$ order reflection point from the transmitter is given by the denominator of (7.5). Similar calculations have been done earlier in case of the tunnels, but there are several differences between these two studies. The frequency considered in [5] is 1

MHz which presents a completely different situation than the frequencies in the mm-wave band. Secondly, the materials used in the construction of the tunnel have a relative permittivity which is not encountered in the case of HVAC duct as these are made up of galvanized steel in general. Thirdly, the distance between the transmitter and the receiver considered in the case of tunnels is in kilometers, whereas the work in this paper is particularly targeting indoor communication restricting the distance to a few meters. Lastly, HVAC ducts will always have smooth wall surface and symmetric shapes compared to the tunnels, which justifies the use of geometric optics to calculate the angles made by the different incident rays. Note – due to the smooth and polished interior surface of the HVAC duct, the propagation-mechanism scattering will be limited and therefore, is not considered as a crucial hindrance in this study.

Another important parameter is the loss in the electric field energy due to the reflection at the duct walls. In general, Fresnel law defines the reduction in the EM wave's energy after every reflection in terms of the Fresnel reflection coefficients. However, since the HVAC ducts are made using galvanized steel, so the reflection coefficient simplifies to $-1$. Consider a total of $M$ rays with each ray getting reflected $N$ times. The $\theta$ component of the radiated electric field amplitude in the spherical coordinate system from a half-wave dipole antenna can be written as

$$E_{\theta}(r,\theta) = \frac{j\eta I}{2\pi r}\frac{\cos\left(\frac{kl}{2}\cos(\theta)\right)}{\sin(\theta)}e^{-jkr} \tag{7.6}$$

where $I$ is the input current in the antenna, $\eta = \sqrt{\mu_0/\epsilon_0}$ is intrinsic impedance of the vacuum with $\mu_0$ and $\epsilon_0$ denoting the permeability and permittivity of free space, respectively,

$k = 2\pi/\lambda$ is the wavenumber, $l$ is the length of the antenna, which is approximately $\lambda/2$ for a half-wave dipole, and $r$ is the distance between the transmitter and the point of observation in the far-field zone. $r$ will be very small (4 cm) and close to the transmitting antenna because of the antenna size and the frequency of operation. For a half-wave dipole, the electric field in the $r$ and $\phi$ directions in the spherical coordinate system are zero. Hence, we focus on the electric-field in the $\theta$ direction. The electric field will be the same at every point at a distance $r$ and at an angle $\theta$ from the antenna. The radiation intensity $U(\theta,\phi)$ can be calculated as

$$U(\theta,\phi) = \frac{r^2}{2\eta}|E_\theta(r,\theta)|^2 = \frac{\eta I^2}{8\pi^2}\frac{\cos^2\left(\frac{\pi}{2}\cos(\theta)\right)}{\sin^2(\theta)} \approx \frac{\eta I^2}{8\pi^2}\sin^3(\theta) \tag{7.7}$$

The above approximation is considered for $\theta \in [0,\pi]$, which is the range of interest. The average Poynting vector $W_T$ can be calculated from the radiation intensity as

$$W_T = \frac{U}{r^2} = \frac{1}{2\eta}|E_\theta(r,\theta)|^2 \approx \frac{\eta I^2}{8\pi^2 r^2}\sin^3(\theta) \tag{7.8}$$

The total radiated power is

$$P_T = \int_0^{2\pi}\int_0^{\pi} r^2 W_T \sin(\theta)\, d\theta d\phi = \int_0^{2\pi}\int_0^{\pi} U(\theta,\phi)\sin(\theta)\, d\theta d\phi = \frac{2.43\eta|I|^2}{8\pi} \tag{7.9}$$

From (7.8) and (7.9), we can see the directivity $D_T$ of the half-wave dipole antenna is given by $D_T = 4\pi \max(U)/P_T = 4\pi\eta|I|^2/8\pi^2 P_T \approx 1.65$. Further, for the transmitting antenna, $D_T = G_T/\varsigma_T$, where $G_T$ is the antenna gain and $\varsigma_T$ is the radiation efficiency. Hence, we have

$$W_T = \frac{P_T \sin^3(\theta)}{2.435\pi \mathrm{r}^2} = \frac{P_{in}\zeta_T \sin^3(\theta)}{2.435\pi \mathrm{r}^2} = \frac{P_{in}G_T}{4\pi r^2} \tag{7.10}$$

Where $\theta = 90^{\circ}$ is assumed due to the antenna's orientation. When the antenna introduces the electric field in the HVAC duct, the field rays either reach the receiver directly or by reflection from the HVAC duct walls. The number of rays which will contribute to the received electric field depend on the type of the antenna and its beamwidth. For a ray $r_d$ which reaches the receiver directly, the radiated electric field will be given as $E_d(r_d, \theta) = E_\theta e^{-jkL}/L$ The average Poynting vector for this component of the field is,

$$W_d = \frac{1}{2\eta}|E_d|^2 = \frac{1}{2\eta}\left|\frac{E_\theta}{L}e^{-jkL}\right|^2 \tag{7.11}$$

The distance $r_d$ will be equal to the length of the HVAC duct, *i.e.*, $r_d = L$. For the rays which suffer one reflection before reaching the receiver, the radiated electric field can be given as $E_1(r_1, \theta) = \frac{-E_\theta}{r_1}e^{-jkr_1}$ Hence,

$$W_1 = \frac{1}{2\eta}|E_1|^2 = \frac{1}{2\eta}\left|\frac{E_\theta}{r_1}e^{-jkr_1}\right|^2 \tag{7.12}$$

In (7.5), we substitute $n = 1$ to get the distance $r_1$ as $r_1 = r[1 + 2 - (-1)] + \mathrm{z}[(-1) - 1]$. Similarly, for the $m^{th}$ ray which suffers $n$ reflections, the radiated electric field is given as $E_m(r_n, \theta) = (-1)^n \frac{E_\theta}{r_n} e^{-jkr_n}$. Furthermore,

$$W_m = \frac{1}{2\eta}|E_m|^2 = \frac{1}{2\eta}\left|\frac{E_\theta}{r_n}e^{-jkr_n}\right|^2 \tag{7.13}$$

where $r_n = r[1 + 2n - (-1)^{\mathrm{n}}] + \mathrm{z}[(-1)^{\mathrm{n}} - 1]$. The total electric field received at the receiver from all the $M$ rays can be given as

$$E_r = E_d + \sum_{m=1}^{M} E_m = \frac{E_\theta}{L}e^{-jkL} + \sum_{m=1}^{M}(-1)^m \frac{E_\theta}{r_m}e^{-jkr_m} \tag{7.14}$$

$M$ is calculated by assuming a ray point at each angle of the beamwidth of the antenna. For this work, we consider the mesh size in the Cartesian coordinates to be 60×60 as $M$=60×60 is the maximum number of rays for the beamwidth considered here. Consequently, the maximum power $P_R$ received at the receiver is given in terms of the average Poynting vector and the maximum effective area of the receiving antenna $A_{R,e}$ as

$$P_R = \frac{|E_r|^2}{2\eta}A_{R,e} = \frac{E_\theta^2}{2\eta}\left|\frac{e^{-jkL}}{L} + \sum_{m=1}^{M}\frac{e^{-jkr_m}}{r_m}\right|^2 A_{R,e} \tag{7.15}$$

In general, the different rays arrive at different angles, resulting in the effective receiving area that is depending on the angle of arrival of each multipath. In this paper, however, we consider the maximum possible effective area. As will be shown in the Results sections, for the practical parameters, the above approximation yields fairly accurate results. From (7.8) and (7.10), we can substitute $W_T = |E_\theta|^2/2\eta$ in (7.15), which results in,

$$P_R = W_T \left| \frac{e^{-jkL}}{L} + \sum_{m=1}^{M} \frac{e^{-jkr_m}}{r_m} \right|^2 A_{R,e} = \frac{P_{in}\mathrm{G_T}}{4\pi \mathrm{r}^2} \left| \frac{e^{-jk(L+r)}}{L} + \sum_{m=1}^{M} \frac{e^{-jk(r_m+r)}}{r_m} \right|^2 A_{R,e} \qquad (7.16)$$

The effective area of the receiving antenna is given as $A_{R,e} = \lambda^2 D_R / 4\pi$ where $\lambda$ is the wavelength and $D_R$ denotes the directivity of the receiving antenna. For the receiving antenna when radiation efficiency $\varsigma_R \approx 1$ is considered and the receiving antenna has the gain $G_R$, we have, $A_{R,e} = \lambda^2 G_R / 4\pi$. Therefore, using the value of $A_{R,e}$ in (16), the maximum total received power $P_R$ can be written as

$$P_R = \frac{\lambda^2 P_{in} G_T G_R}{16\pi^2} \left| \frac{e^{-jk(L+r)}}{L} + \sum_{m=1}^{M} \frac{e^{-jk(r_m+r)}}{r_m} \right|^2 \qquad (7.17)$$

Moreover, an important factor while characterizing the HVAC duct as a viable communication link is the consideration of the temperature and the density of the moisture vapor present in the air flowing through the duct. The attenuation due to the atmospheric gases flowing inside the HVAC duct is given by $\phi_g = \phi_d + \phi_m$ , where $\phi_d$ and $\phi_m$ represent the attenuation caused due to the dry air and the moisture vapor, respectively. The attenuation caused by dry air is due to its pressure and the atmospheric temperature. For, $57\text{ GHz} \leq f \leq 63\text{ GHz}$, this parameter is given by [5]

$$\phi_d = \gamma_{57} \frac{(f-60)(f-63)}{18} - 1.66 r_p^2 r_t^{8.5} (f-57)(f-63) + \gamma_{63} \frac{(f-57)(f-60)}{18} \qquad (7.18)$$

where $\gamma_{57}$ and $\gamma_{63}$ are zero for 57 GHz $\leq f \leq 63$ GHz. However, for $f \leq 57$ GHz,

$$\gamma_{57} = \frac{0.0073 f^2 r_p^2 r_t^3}{f^2 + 0.351 r_p^2 r_t^2} + \frac{0.0075 f^2 r_p^2 r_t^2}{(f-57)^2 + 2.44 r_p^2 r_t^5} \tag{7.19}$$

while $\gamma_{63} = 0$. For 63 GHz $\leq f \leq 350$ GHz, and $\gamma_{57} = 0$

$$\gamma_{63} = \frac{f^2 r_t^{3.5} r_p^2}{5 \times 10^6} - \frac{r_t^{3.5} f^{3.5} r_p^2}{4.2 \times 10^{15}} + \frac{0.004 f^2 r_t^2 r_p^2}{(f-63)^2 + 1.5 r_p^2 r_t^5} + \frac{0.00028 f^2 r_t^4 r_p^2}{(f-118.75)^2 + 2.84 r_p^2 r_t^2} \tag{7.20}$$

In the above, $f$ [GHz] is the frequency, $r_p = p/1013$, $r_t = 288/T$, $p$ [hPa] is dry atmospheric pressure, and $T$ is the atmospheric temperature in Kelvin. The attenuation coefficient of moisture vapor depends on the density of moisture vapor $\rho\ in\ g/m^3$ and is given by [5]

$$\phi_m = \frac{r_t^2 r_p f^2 \rho}{3\times10^5} + \frac{\rho^2 r_t^8 f^2}{6\times10^6} + \frac{r_t r_p f^{2.5} \rho}{1.3\times10^7} + \frac{0.0004 r_t r_p f^2 \rho}{(f-22.235)^2 + 9.81 r_p^2 r_t} + \frac{0.001 r_t^2 r_p f^2 \rho}{(f-183.31)^2 + 11.85 r_p^2 r_t} +$$

$$\frac{4.01\times10^{-4} r_t^2 r_p}{(f-325.153)^2 + 10.44 r_p^2 r_t} \tag{7.21}$$

The received power $P_R$ at the receiving antenna incorporating the attenuation due to the temperature, pressure, and the moisture content of the gases flowing through the HVAC duct is given by,

$$P_R = \frac{\lambda^2 P_T G_T G_R}{16\pi^2 \phi_g} \left| \frac{e^{-jk(L+r)}}{L} + \sum_{m=1}^{M} \frac{e^{-jk(r_m+r)}}{r_m} \right|^2 \tag{7.22}$$

The path loss is defined as $PL(dB) = 10\log_{10}(P_T/P_R)$. The received signal strength indicator (RSSI dBm) takes into account the path loss suffered by the rays while traveling through the HVAC duct and is given as [54]

$$RSSI = EIRP - PL(dB) \tag{7.23}$$

where $EIRP$ is the effective isotropic radiated power from the transmitter and measured in dBm.

### 7.4 Ray-Tracing applied to HVAC Duct

We consider a rectangular HVAC duct for the 3D ray-tracing simulation, as the ray-tracing effects for the cylindrical and the rectangular HVAC duct will be similar due to the dimension of the HVAC duct compared to the wavelength of the mm-wave traveling through it. The dimension of the HVAC duct considered for the simulation is 9 cm × 9 cm. Figure 7.4 shows the HVAC duct with the transmitter and the receiver at the two ends of the duct. As the receiver can be placed anywhere in the duct to capture the signal, a section in the center of the HVAC duct is considered as the receiver. We can observe the different LOS rays as well as rays experiencing multiple reflections from the duct walls traveling between the transmitter and the receiver. The beamwidth of the transmitter antenna decides the number and the incident angle of the rays.

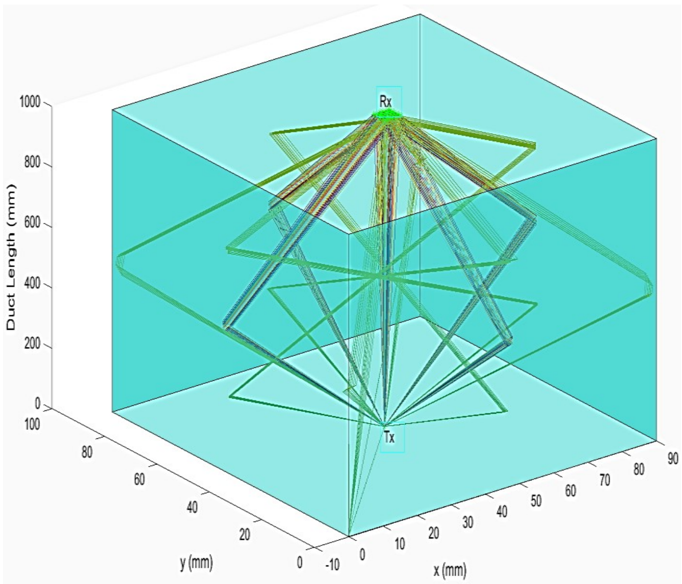

Figure 7.4. 3D RT inside HVAC duct with transmitter and receiver

Figure 7.5 shows the variation of received signal strength indicator (RSSI) for HVAC duct of length 1 m. In Figure 7.5a, RSSI due to the LOS rays is considered. As the HVAC duct considered for the 3D RT simulation is straight, most of the incident rays reach the receiver without suffering any reflection. The RSSI level for the LOS case is around -23 dBm. Figure 7.5b and 7.5c show the resulting RSSI due to the rays suffering one and two reflections before reaching the receiver present on the other end of the HVAC duct. The rays are launched at an angle that is confined to $\pm 30^{\circ}$ around the transmitter antenna. Therefore, the rays will have different incident angles and will follow the path accordingly. The RSSI level for the one reflection case is around -24 dBm and for the two-reflection case is around -25.5 dBm. We assume that the transmitter effective isotropic radiated power (EIRP) is 7 dBm.

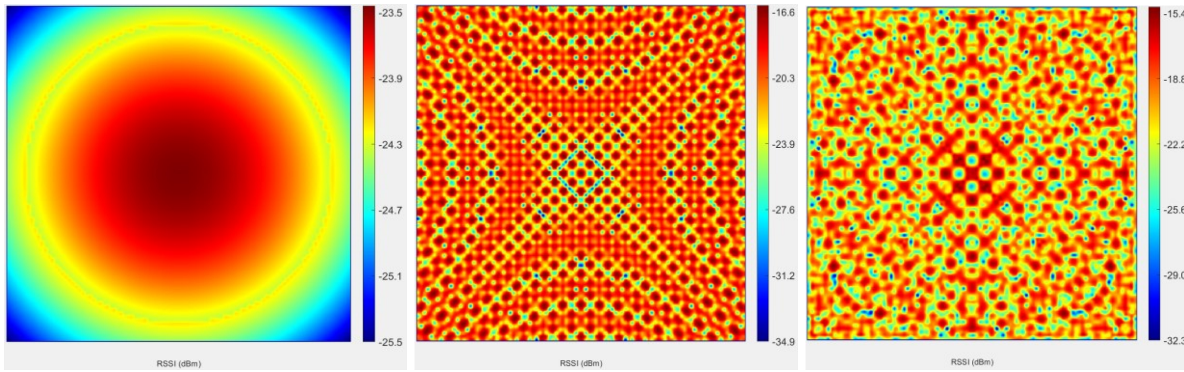


(a) (b) (c)

Figure 7.5. RSSI for HVAC duct $L$ =1 m (a) LOS (b) First reflection, (c) Second reflection

Figure 7.6 shows the comparison between the RSSI obtained through the experiment (Exp) and the ray-tracing simulation (RT Sim) as described in this dissertation. In [53], we performed the experiments with a circular HVAC duct of diameter 12.7 cm and made of galvanized steel. For the experiment we used the Tensorcom chipsets TC60G-USB3-EVB as the transmitter and receiver with the $\pi/2$-BPSK and $1/2$ coding rate with a bandwidth of 2.16 GHz. The chipsets come with a Linux based speed test application which we used to evaluate the RF performance of HVAC ducts as well as free space. Using the 3D ray-tracing simulations and calculating RSSI, we have verified the theoretical and experimental results [53], [54]. We obtain RSSI values of -27 dBm, -30 dBm, -35 dBm and -40 dBm for a straight HVAC duct of length 1 m, 2 m, 4 m, and 8 m, respectively. We note that the 3D ray-tracing and the equations presented in the previous section are for the maximum possible received power. Hence, the observed RSSI over the frequency range remains below the simulation results. The difference proves to be only a few dB for most frequencies considered. In general, the results prove the validity and efficacy of the 3D ray-tracing method described in calculating the value of RSSI.

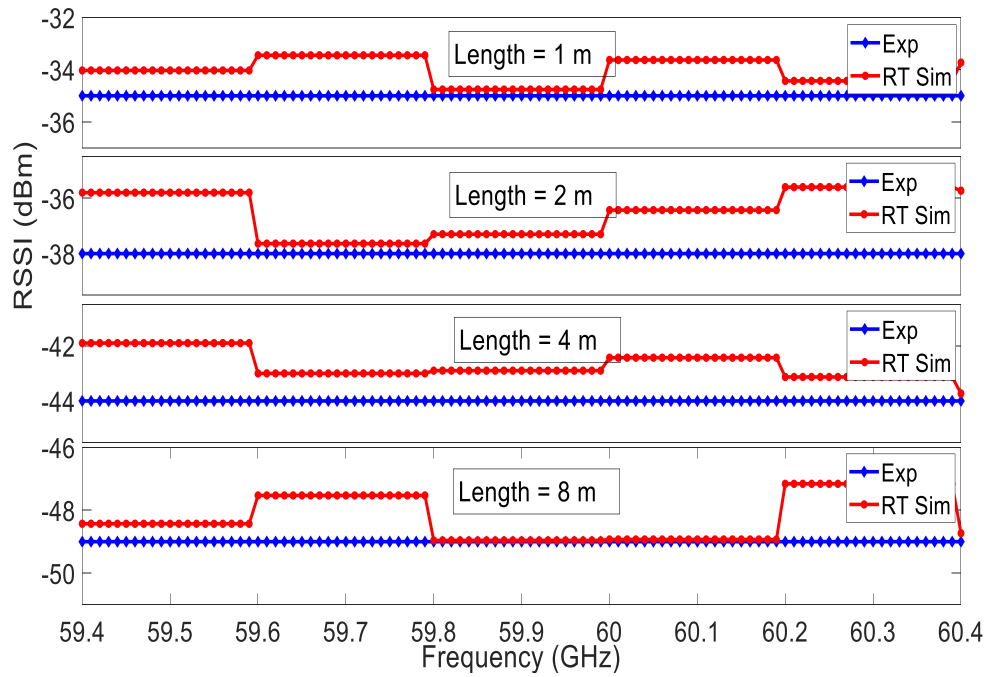

Figure 7.6. Comparison of experimental and RT RSSI results for HVAC duct

As the total number of rays launched in the HVAC duct for the 3D ray-tracing simulation depend on the beam-width of the antenna used. On varying the antenna beamwidth, the total number of rays launched will vary and will lead to different values of RSSI obtained. However, in most practical antenna designs, the goal is to find a balance between the beamwidth and the directivity of the antenna because as the beamwidth increases, the directivity of the antenna decreases. The antenna used in the experimental work [53], [54] has a beamwidth of $\pm 30^{\circ}$. However, to show the effect of the beamwidth or the total number of rays launched, we compare the RSSI values obtained by ray-tracing simulation for three different beamwidths of $\pm 30^{\circ}, \pm 60^{\circ}$ and $\pm 90^{\circ}$ for HVAC duct of length 1 m in Figure 7.7. We observe that, in this case, as we consider the broader beamwidth, a larger number of rays reach the receiver and thereby we observe an increased RSSI.

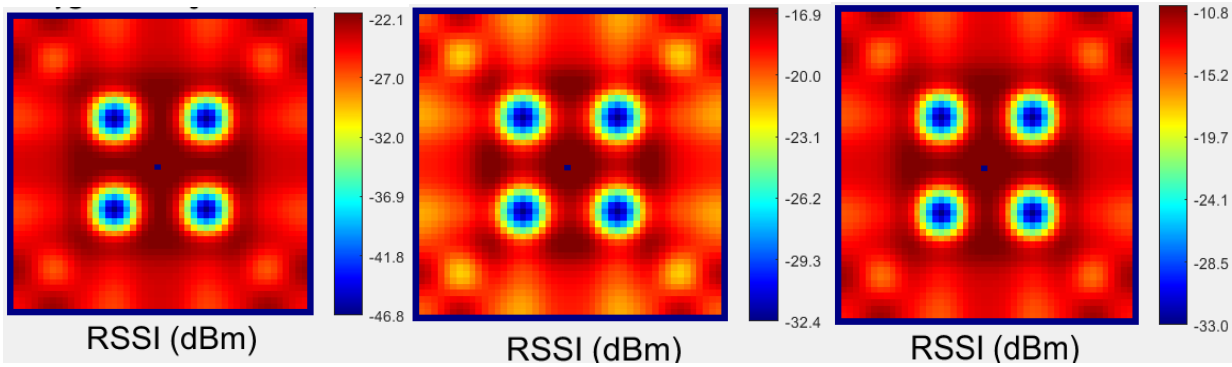


(a) (b) (c)

Figure 7.7. First reflection RSSI with antenna beamwidth (a) $\pm 30°$, (b) $\pm 60°$ and (c) $\pm 90°$

The experiment is done using HVAC ducts which are not installed in the buildings, due to which the RSSI results do not account for the temperature and moisture content of the air flowing through the HVAC duct. In Figure 7.8, we present a comparison of the ray-tracing results in terms of RSSI values computed with the assumption of no air flowing through the HVAC duct (without T) and the RSSI obtained using (7.23) which incorporates temperature and pressure of the air flowing the HVAC duct through the parameter $\phi_g$. Air pressure is calculated based on the standards for the air flowing through the HVAC ducts for a given temperature. RSSI values obtained for a temperature range of T = 288.15 K to T = 303.15 K are shown in Figure 7.8 and compared with the RSSI values obtained without considering any temperature or pressure of the air flowing through the HVAC duct. Further, the results are also compared to the free space path loss (FSPL), which takes place at 60 GHz for different path lengths.

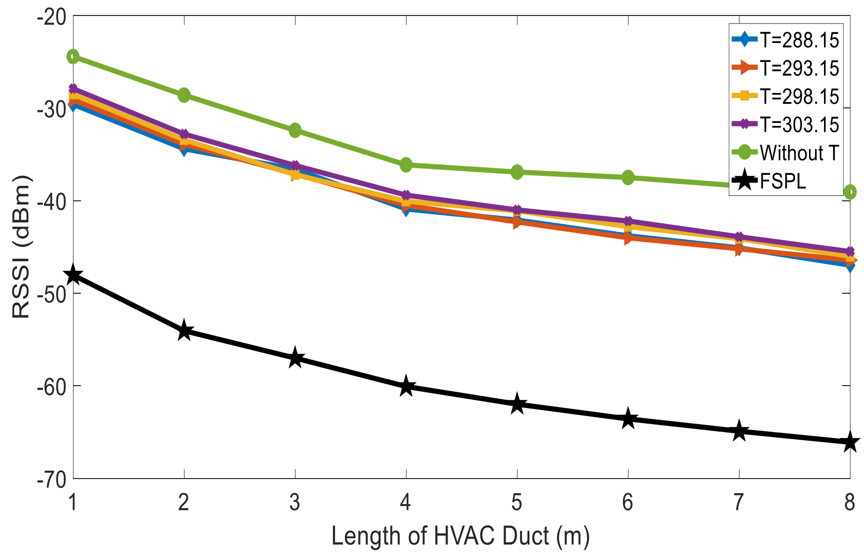

Figure 7.8. RSSI obtained with and without atmospheric temperature and pressure

We can see from the Figure 7.8 that the RSSI values for the different values of temperature are almost similar, concluding that the variation in temperature does not have a significant effect on RSSI. However, on comparing the RSSI results obtained by considering the temperature effects to the case when we ignore the effect of temperature and pressure of the air flowing through the duct, we observe that the latter is decreased by around 3 dBm for distances of up to 4 m and 6 dBm for 8 m. It can also be concluded from Figure 7.8 that the RSSI values obtained for the HVAC duct are much higher than those obtained through free space, thereby justifying the use of the HVAC ducts to distribute mm-wave signals.

Figure 7.9 shows the ray-tracing results in terms of comparison of the RSSI values obtained by considering the moisture vapor density ($g/m^3$) of the air flowing through the HVAC duct using (7.23) and the RSSI values computed with the assumption of no air flowing through the HVAC duct (without moisture). The moisture vapor density is varied between Density = 1140

$g/m^3$ to Density = 1200 $g/m^3$ and the RSSI values are calculated for different duct length varying between 1 m to 8 m. Contrary to Figure 7.8 where temperature had minimal effect on the RSSI values, moisture vapor density shows significant effect on the values of RSSI obtained for different lengths of HVAC duct. On comparing the RSSI results obtained by considering the moisture vapor density to the case where we ignore the presence of the moisture vapor, we observe that the RSSI is decreased by 11 dBm for distances of up to 4 m and 14 dBm for 8 m in the presence of moisture. However, the results obtained are around 10 dBm above those obtained when considering free space propagation. The point to note in Figure 7.9 is that, while we did the theoretical analysis of RSSI values obtained while considering the air with moisture vapors present in it, in most practical scenarios, HVAC ducts will not be carrying the air with moisture vapor. So, it suffices to say that HVAC duct outperforms the free space propagation in every situation.

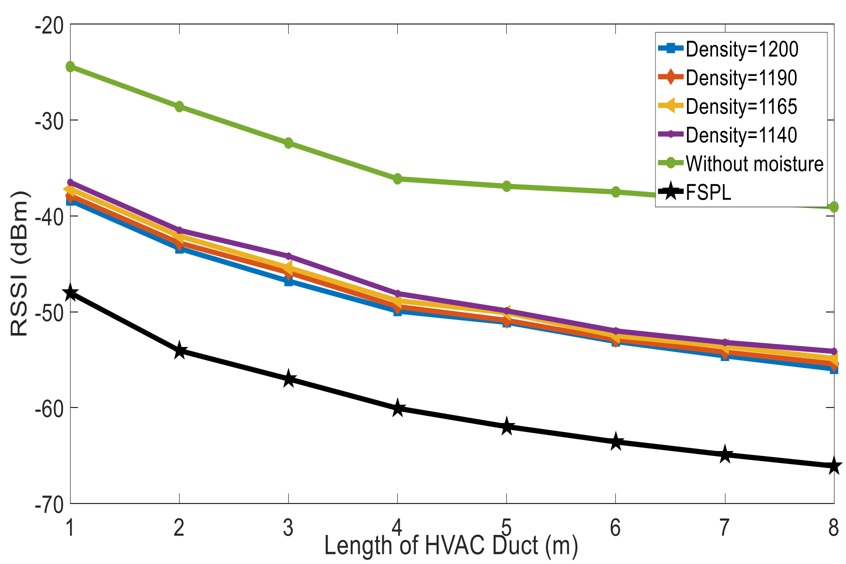


Figure 7.9. RSSI obtained by considering air with moisture vapor

Table 7.1. Comparison of performance of HVAC duct with other methodologies

| Ref. | Dist. | Freq. (GHz) | Technique Used | Measurement | Ray-Tracing | RSSI (dBm) |
|---|---|---|---|---|---|---|
| [51] | 2 m | 70 | Beam-forming | Custom mm-wave CS | Custom 3D | -91 |
| [41] | 5 m | 60 | Directional high gain antenna with max. ray beamforming | - | Ray launching RT | -80 |
| [23] | 6 m | 58.5 | Q-D channel with fading | Custom channel sounder | Clustering and diffuse scattering model | -70 |
| [22] | 4.5 m | 60 | Biconical omnidirectional antennas | Custom channel sounding system | - | -85 |
| [44] | 4 m | 60 | Polarimetric diffuse scattering channel model | Custom channel sounding system | - | -85 |
| [25] | 4 m | 60 | Ray path inference by beam pattern of phased array | SiBeam Phased array | Scenargie RT simulator | -50 |
| [91] | 5.4 m | 60 | Beam-forming | Custom mm-wave CS | - | -90 |
| [24] | 10 m | 60 | - | Hittite HMC6000LP711E | - | -100 |
| [92] | 6 m | 60 | Omnidirectional antenna SAGE 5836230230-15-S1 | | Custom 3D in MATLAB | -85 |
| FSPL | 8 m | 60 | - | - | - | -68 |
| HVAC | 8 m | 60 | Without air | Custom mm-wave CS | Custom 3D IM in MATLAB | -47 |
| HVAC | 8 m | 60 | Air at a temp. of 288.15 K | Custom mm-wave CS | Custom 3D IM in MATLAB | -47 |
| HVAC | 8 m | 60 | Air with moisture of density $1200 g/m^3$ | Custom mm-wave CS | Custom 3D IM in MATLAB | -57 |

Table 7.1 gives an overview of the performance comparison of HVAC ducts with some of the other recent methodologies and studies done for millimeter wave communication.

### 7.5 Discussion

A 3-dimensional (3D) ray-tracing tool to justify the use of HVAC ducts for the distribution of mm-wave signals was proposed. The 3D ray tracing tool is subjected to the condition of operation in mm-wave frequency band and for symmetrical structures, which lead to the reduction in the time and memory required to run the simulation. We incorporated the attenuation parameters due to the dry air and moisture vapor flowing through the HVAC duct. The results obtained from the ray-tracing were further utilized to calculate RSSI. With transmitter EIRP of 7 dBm, we obtain RSSI which varies between -24 dBm to -38 dBm for dry atmospheric pressure and temperature of 1013.25 hPa and 294.26 K, respectively, and duct lengths of up to 8 m at 60 GHz. The results were compared with the experimental results and we observe that the 3D ray tracing results match closely the experimental results, which further justifies the use of HVAC ducts for the distribution of mm-wave signals in an indoor environment. Future work will include extending the 3D ray tracing simulation for the HVAC ducts with different shapes and bends.

In order to arrive at the general expression of the angle of incident, we consider a situation where three reflections has occurred. For a ray which undergoes three reflections, $p_u$ can be divided into six parts as $p_u = p_{u1} + p_{u2} + p_{u3} + p_{u4} + p_{u5} + p_{u6}$ as shown in Figure 7.10. The angle which the transmitted wave makes with the normal to the upper duct wall is represented as

$\theta_{u3}$. Therefore, the distances between the transmitter $T_x$, different reflection points and the receiver $R_x$, the tangent of the angle $\theta_{u3}$ can be represented as

$$\tan(\theta_{u3}) = \frac{p_{u1}}{d - z_T} = \frac{p_{u2}}{d - z_R} = \frac{p_{u3}}{z_R} = \frac{p_{u4}}{z_R} = \frac{p_{u5}}{d - z_R} = \frac{p_{u6}}{d - z_R} = \frac{p_u}{d - z_T + 3d - z_R}$$

$$\cong \frac{p_u}{4d - 2z} \tag{7.24}$$

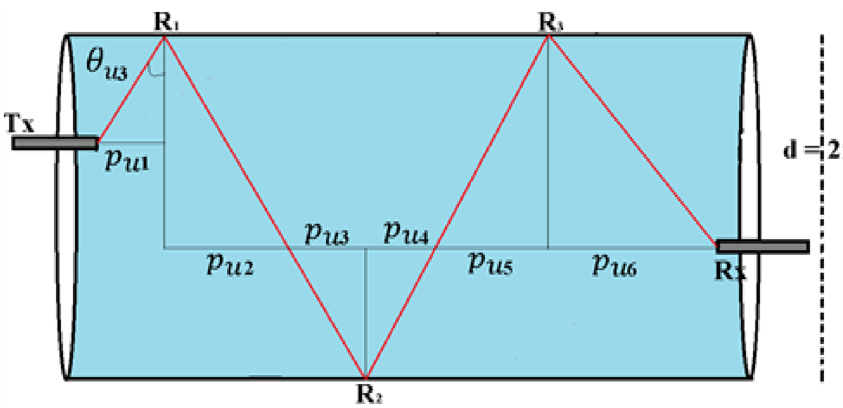

Figure 7.10. Ray tracing with three reflections inside the HVAC duct

The last part of (7.24) is calculated using $z_T \cong z_R$. Also, using the process described above, we can calculate the perpendicular distance between the reflection points and the projections for a ray that undergoes $n$ odd or even number of reflections. For a ray that makes odd number of reflections, the total perpendicular distance will be equal to

$$(d - z_T) + n(d - z_R) + (n - 1)z_R \tag{7.25}$$

Similarly, for a ray that makes even number of reflections, the total perpendicular distance will be equal to

$$(d - z_T) + (n-1)(d - z_R) + nz_R \qquad (7.26)$$

Using (7.25), (7.26), and assuming that $z_T \cong z_R$, we arrive at the denominator in (7.9).

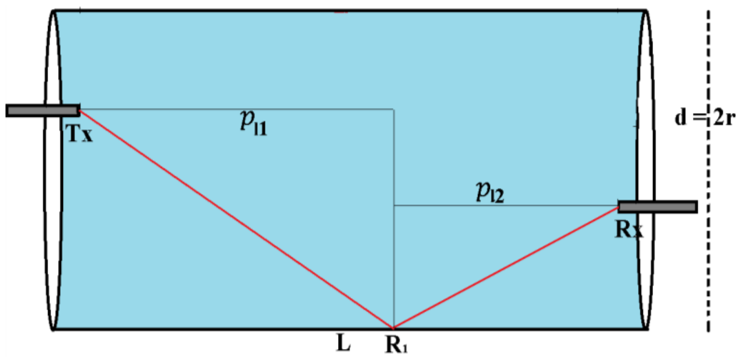


Figure 7.11. Ray tracing with one reflection inside the HVAC duct

For the rays which are directed in the downward direction, we perform similar steps as that for the upward directed rays to arrive at (7.10). For a ray which has one reflection point $R_1$ on the lower duct wall, $p_l = p_{l1} + p_{l2}$. The tangent of the angle which the ray makes with the lower duct wall is given in terms of $p_l$ as

$$\tan(\theta_{l1}) = \frac{p_{l1}}{z_T} = \frac{p_{l2}}{z_R} = \frac{p_l}{z_T + z_R} \approx \frac{p_l}{2z_T} \qquad (7.27)$$

If a ray is reflected twice (Figure 7.12), once from the lower wall $R_1$ and then from the upper wall $R_2$, then $p_l$ can be divided into four parts as $p_l = p_{l1} + p_{l2} + p_{l3} + p_{l4}$. The angle which the transmitted wave makes with the normal to the lower duct wall is represented as $\theta_{l2}$.

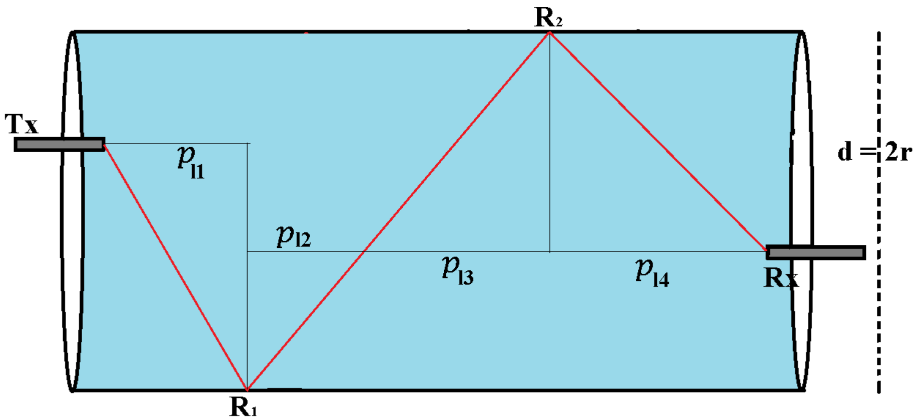

Figure 7.12. Ray tracing with two reflections inside the HVAC duct

Therefore, the tangent of the angle $\theta_{l2}$ can be represented as

$$\tan(\theta_{l2}) = \frac{p_{l1}}{z_T} = \frac{p_{l4}}{d-z_R} = \frac{p_{l3}}{d-z_R} = \frac{p_{l2}}{z_R} = \frac{p_l}{z_T+2(d-z_R)+z_R} \approx \frac{p_l}{2d} \qquad (7.28)$$

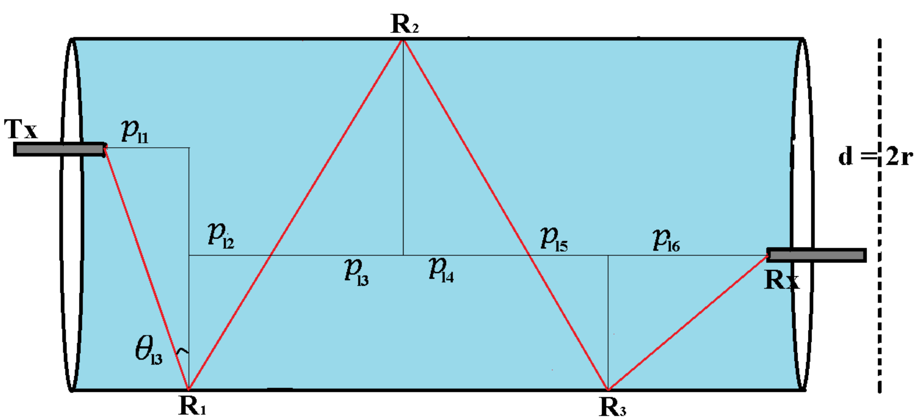

Figure 7.13. Ray tracing with three reflections inside the HVAC duct

If a ray is reflected three times (Figure 7.13), twice from the lower wall $R_1$ and $R_3$ and once from the upper wall $R_2$, then $p_l$ can be divided into six parts as $p_l = p_{l1} + p_{l2} + p_{l3} + p_{l4} + p_{l5} + p_{l6}$. The angle which the transmitted wave makes with the normal to the lower duct wall is represented as $\theta_{l3}$. Therefore, the tangent of the angle $\theta_{l3}$ can be represented as

$$\tan(\theta_{l3}) = \frac{p_{l1}}{z_T} = \frac{p_{l2}}{z_R} = \frac{p_{l3}}{d - z_R} = \frac{p_{l4}}{d - z_R} = \frac{p_{l5}}{z_R} = \frac{p_{l6}}{z_R} = \frac{p_l}{z_T + 2(d - z_R) + 3z_R}$$
$$= \frac{p_l}{2d + z_T + z_R} \approx \frac{p_l}{2d + 2z} \tag{7.29}$$

The last part of (7.29) is calculated using $z_T \cong z_R$. For a ray that makes odd number of reflections, the total perpendicular distance will be equal to

$$z_T + (n - 1)(d - z_R) + nz_R \tag{7.30}$$

Similarly, for a ray that makes even number of reflections, the total perpendicular distance will be equal to

$$z_T + n(d - z_R) + (n - 1)z_R \tag{7.31}$$

Using (7.30), (7.31), and assuming $z_T \cong z_R$, we arrive at (7.10).

# CHAPTER 8

# PATCH ANTENNA

## 8.1 Background for Patch Antenna

The emerging high-data-rate wireless mobile services, such as wireless high-definition transmissions, wireless personal area networks, and the $5^{th}$-generation technology, require high-capacity wireless communication media to operate. One such medium is millimeter wave (mm-wave) channels, which also enable WiGig systems. Frequency bands of particular interest in the mm-wave spectrum are the unlicensed bands at 60 GHz (57 GHz-66 GHz) and 70 GHz (71 GHz-76 GHz), which can be exploited for short-range wireless communications and close-range automotive radar sensor applications. Antennas are one of the major components of the transceiver systems used for the deployment of these applications. As the various technologies are moving towards the micro-size dimensions, the service providers and the application users demand wireless units with antennas that are compact, cost-effective, and low profile. In addition, to compensate for the large path-loss at mm-wave frequencies, antennas with high gain and wide bandwidth are needed to provide reliable communication.

There are several single element antennas and antenna arrays with different technologies to enhance the bandwidth and gain at 60 GHz [113]-[148]. Microstrip patch antenna on a printed circuit board (PCB) substrate is widely used at low frequencies because it can be implemented with low profile, low weight, and low cost [131]. But at mm-wave frequencies, it shows poor performance due to high substrate losses and low radiation efficiency [131].

Researchers have proposed several patch antennas and patch array antennas for use in the mm-wave frequencies. In order to achieve better antenna performance in terms of gain, bandwidth, radiation efficiency, antenna dimensions, and complexity of the design further research in the field is justified. In [148], a circularly polarized antenna with a single layer structure is proposed. The asymmetric inset technique is utilized to increase the bandwidth of the antenna. However, the feeding technique increases the complexity of the design and the bandwidth of the antenna is comparatively smaller than some other recent patch antenna designs. The authors in [131] describe an antenna design in which the patch is suspended in air through supporting and feeding posts and is fed using a coplanar waveguide feed. In spite of using a glass substrate and increasing the height of the antenna by suspension in air, the authors report only 6.67% of bandwidth for the single element patch antenna. A multilayer structure with a complicated feeding technique was proposed by the authors in [132]. Due to the several layers of substrate and radiating elements and the drilling of the vias, the fabrication of the design will be a tedious process. Moreover, for the single element, the maximum gain achieved is only 6 dBi with a bandwidth of 11%. A very interesting design with $4 \times 1$ parasitic patch antenna array in shape of letter 'E' was proposed in [134]. The shape of the element antenna and the array pattern resulted in a large antenna size but managed to provide a satisfactory 21% bandwidth and 14 dBi total gain. In [135], the authors compromised the size in order to get more bandwidth and to increase the gain. However, with the recessed ground technique, which increased the height of the antenna, the bandwidth reported for $2 \times 1$ patch antenna array was only 10.2% whereas the gain was 7 dBi.

In this chapter, we optimize the performance of the microstrip patch antenna by utilizing several crucial factors. We use LTCC dielectric with high dielectric constant, as the first layer of the substrate, to reduce the dielectric losses. We utilize Styrofoam dielectric to form the second layer of the substrate, which adds to the height of the antenna, thereby increasing the bandwidth and gain of the antenna. Moreover, we also use asymmetric inset microstrip feed line which produces two resonance frequencies, thereby increasing the bandwidth further. The proposed patch antenna is also circularly polarized with axial ratio (AR) of less than 3 dB and a bandwidth of 4.9 GHz or 8.2%. With the utilization of these techniques, we propose a simple design with varying dimensions, which provide high gain and wide bandwidth at mm-wave frequencies. The performance of the proposed antenna is compared with other microstrip patch antennas and arrays at 60 GHz in terms of bandwidth, return loss, efficiency, gain, and design complexity. The remainder of this paper is organized as follows. The proposed antenna structure is described in Section II. The simulation results are presented in Section III. Finally, conclusions regarding the proposed structure are presented in Section IV.

### 8.2 Proposed Antenna Structure

The basic configuration of the proposed multilayer substrate 60 GHz patch antenna is shown in Figure 8.1. A single patch antenna is directly connected to an asymmetric inset microstrip feed line. Therefore, the proposed antenna has a compact size and low cost and can easily be integrated with monolithic microwave integrated circuits (MMIC), such as voltage-controlled oscillators (VCO) and power amplifiers. To increase a high bandwidth and to reduce the dielectric losses, the multilayer substrate technique is used. The first layer of the substrate above the ground plane is made up of Ferro A6M with a dielectric constant of 5.9 and a loss tangent of 0.002 and a thickness of 0.16 mm. Styrofoam 103P7 with a dielectric constant of 1.03 and a loss tangent of 0.0001 is used as the second dielectric material. The two designs that are shown in this letter differ only in the patch and substrate dimensions but are designed based on the same basic configuration of the proposed patch antenna. We note that the bandwidth of the antenna is determined by the antenna height, the dielectric constant of the substrate, and the feeding mechanism. Due to the extremely low dielectric constant of the Styrofoam dielectric, which behaves as an insulator, the bandwidth of the antenna is significantly broadened. The proposed antenna is designed and optimized with a three–dimensional (3-D) Altair CAD Feko software.

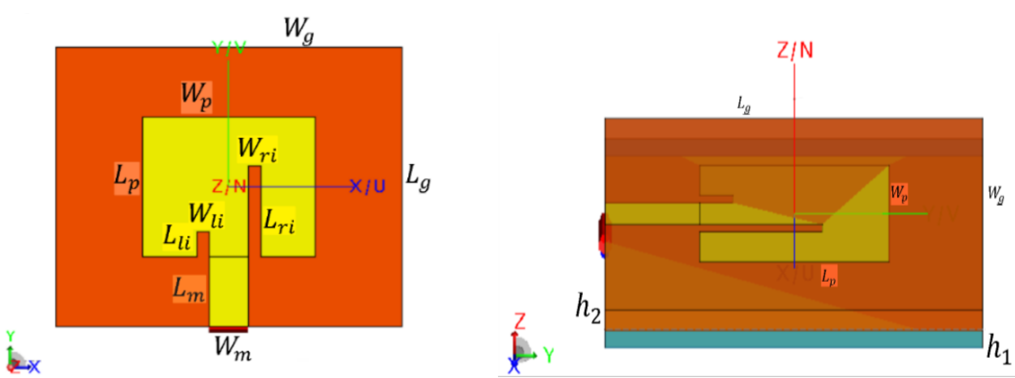


Figure 8.1. (a) The top view (b) The side view of the proposed antenna

As shown in Figure 8.1, the antenna is also comprised of an asymmetric inset microstrip feed line. The asymmetric inset microstrip feed performs better than the general microstrip line at mm-wave frequencies. The dimension of the inset feed line can be optimized for better impedance matching of the patch. Furthermore, the asymmetric structure helps in producing two resonance frequencies at 60 GHz and 67 GHz leading to an increase in the bandwidth. Due to the extremely low dielectric constant of the Styrofoam, the geometry of the microstrip transmission line can be easily modified, leading to a variable characteristic impedance and better impedance matching. Also, the proposed antenna is implemented on a Styrofoam, and, thus, the alignment of the two layers of the substrate will be very convenient. Therefore, it can easily become a better candidate in the manufacturing of mm-wave antennas for different applications. All the design parameters for the two designed of the proposed patch antenna are given in Table 8.1.

Table 8.1. Design parameters of the multilayer substrate microstrip patch antenna

| Parameter | Design I – Value (mm) | Design II – Value (mm) |
|---|---|---|
| LTCC thickness $h_1$ | 0.16 | 0.16 |
| Styrofoam thickness $h_2$ | 0.2 | 0.32 |
| LTCC dielectric const $\epsilon_{r1}$, Loss tangent $\delta_1$ | 5.99, 0.005 | 5.99, 0.005 |
| Styrofoam dielectric const $\epsilon_{r2}$, Loss tangent $\delta_2$ | 1.03, 0.0001 | 1.03, 0.0001 |
| Patch size $(L_p \times W_p)$ | 2 x 2.48 | 2.145 x 2.48 |
| Microstrip $(L_m \times W_m)$ | 1 x 0.56 | 1.0725 x 0.58 |
| Left Inset $(L_{li} \times W_{li})$ | 0.35 x 0.18 | 0.48 x 0.15 |
| Right Inset $(L_{ri} \times W_{ri})$ | 1.3 x 0.18 | 1.1 x 0.15 |
| Ground plane $(L_g \times W_g)$ | 4 x 4.96 | 4.29 x 4.96 |
| Total Antenna $(L \times W \times h)$ | 4 x 4.96 x 0.36 | 4.29 x 4.96 x 0.48 |

## 8.3 Simulation Results

We performed the simulation of the proposed antenna using Altair CAD Feko commercial software program. Figure 8.2 shows the simulated $|S_{11}|$ result for the proposed antenna for design I (DI). The figure depicts that $|S_{11}|$ is less than -10 dB for the frequency range of 56.7 GHz and 68.66 GHz resulting in a bandwidth of 11.96 GHz or 19.93%. The simulated antenna gain and radiation efficiency of the proposed patch antenna for design I are 9 dBi and 97% at 60 GHz, respectively.

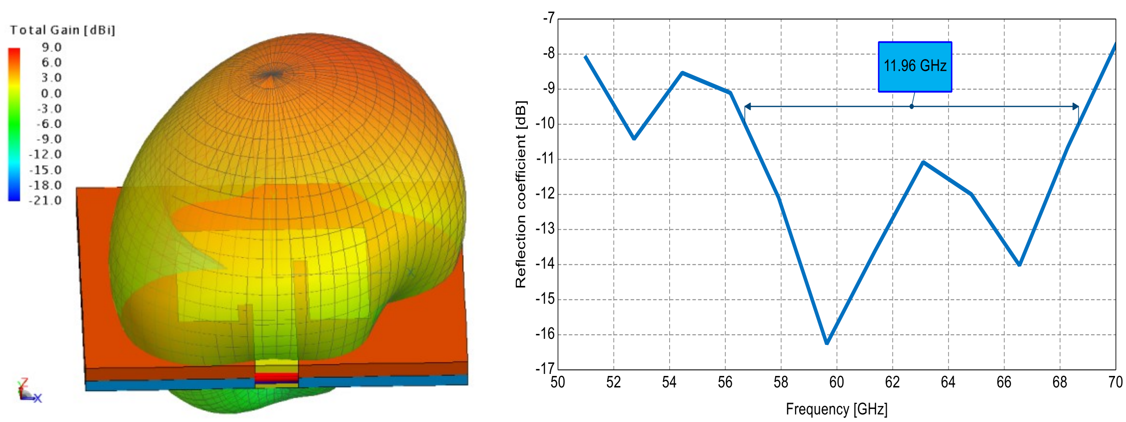


Figure 8.2. (a) The gain and the radiation pattern of design I (DI) (b) Return loss

Figure 8.3 shows the RHC (right-handed circular-polarization) and LHC (left-handed circular-polarization) gain for the proposed antenna design I (DI). We can observe that the antenna has RHC with a half power beamwidth (HPBW) of 57° and 67° for $\phi = 0°$ and 90°, respectively. Also, the antenna has LHC with a HPBW of 61° and 74° for $\phi = 0°$ and 90°, respectively.

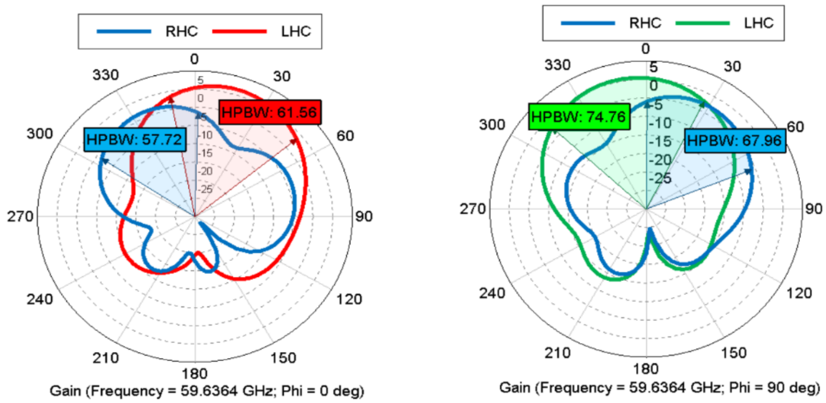

Figure 8.3. The RHC and LHC gains for design I (DI) (a) for $\phi = 0°$ (b) for $\phi = 90°$

Figure 8.4 shows the simulated $|S_{11}|$ result for the proposed antenna for design II (DI). The $|S_{11}|$ for design II is less than -10 dB for the frequency range of 54.91 GHz and 67.83 GHz, resulting in a bandwidth of 12.92 GHz or 21.53%. The simulated antenna gain and the radiation efficiency of the proposed patch antenna for design II are 8 dBi and 96% at 60 GHz, respectively. Both Figure 8.3 and Figure 8.5 also demonstrate that the proposed antennas are characterized by omnidirectional radiation pattern.

Figure 8.5 shows the RHC and LHC gains for the proposed antenna design II (DII). We can observe that the antenna has RHC with a half power beamwidth of 55° and 66° for $\phi = 0°$ and 90°, respectively. Also, the antenna has an LHC with a half power beamwidth of 60° and 75° for $\phi = 0°$ and 90° , respectively.

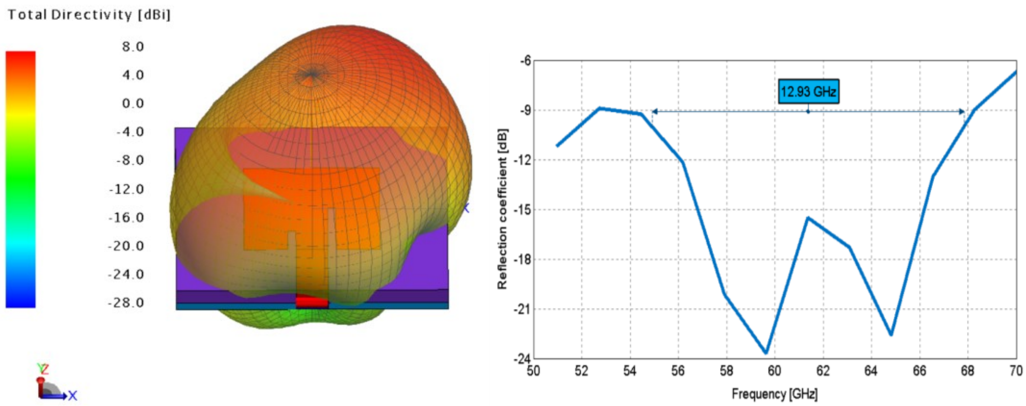


Figure 8.4. (a) The gain and the radiation pattern of design II (DII). (b) Return loss

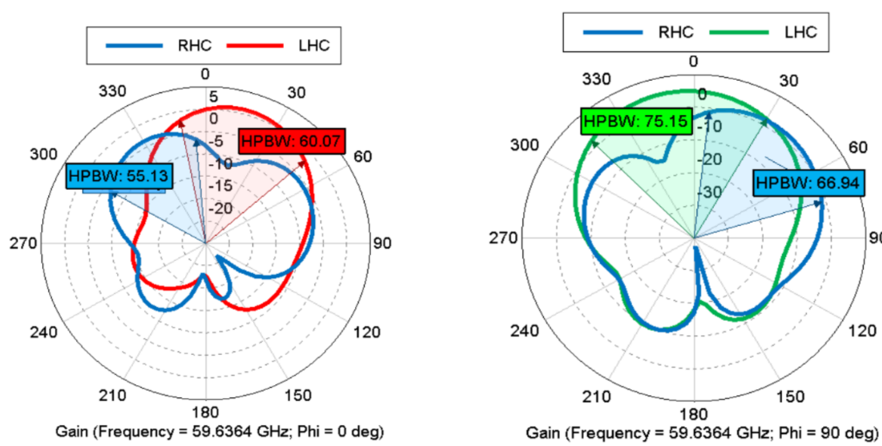


Figure 8.5. The RHC and LHC gains for design II (DII) (a) for $\phi = 0°$ (b) for $\phi = 90°$

We present the comparison results of the performance of the proposed antenna to other patch antenna designs. In order to provide a fair comparison, we have only considered the single element antennas. The comparison was made on the basis of gain (dBi), bandwidth BW (%), return loss RL (dB), the dielectric material used for substrate, feeding technique, and the total dimension of the antenna. The results of the comparison are given in Table 8.2. As can be seen, the proposed antenna design offers a superior gain and a larger bandwidth while achieving similar RL when compared with the prior designs.

Table 8.2. Comparison of the proposed antenna to other patch antenna designs

| Ref. | Gain (dB) | BW (GHz) | RL (dB) | Substrate | Feeding Technique | Total Size (mm) |
|---|---|---|---|---|---|---|
| [148] | 7.4 | 17 | -12 | Teflon 2.2 | GSG (ground signal ground) | 5.5 x 3 x 0.25 |
| [131] | 8.7 | 6.67 | -30 | Corning 7740 glass 4.6 | CPW (coplanar waveguide) | 2.2 x 2.2 x 0.2 |
| [132] | 6 | 11.6 | -30 | Ferro A6M 5.99 | SIW (substrate integrated) | 2.5 x 2.5 x 0.384 |
| D1 | 9 | 19.9 | -16 | Multilayer | Microstrip | 4 x 4.96 x 0.36 |
| D2 | 8 | 21.5 | -24 | Multilayer | Microstrip | 4.29 x 4.96 x 0.48 |

### 8.4 Summary and Conclusions

In this chapter, we have presented a multilayer substrate (LTCC and Styrofoam) asymmetric inset fed microstrip patch antenna for broadband, high-data rate wireless applications at millimeter wave frequencies (specifically 60 GHz). The antenna configuration is designed and analyzed by using Altair Feko commercial software. The dimensions of the substrate, radiating patch and feed line were optimized to enhance the antenna performance parameters. The LTCC layer of the substrate with its high dielectric constant led to an extremely low dielectric loss. Meanwhile, the second layer of substrate (Styrofoam) on which the antenna is supported, due to its low dielectric constant, led to the broadband characteristics of the antenna. Further, the design consisted of a simple microstrip feed network, which allowed for its integration with MMICs and system on a chip (SOC) at mm-wave frequencies. The asymmetric inset feed led to the generation of two resonance frequencies, thereby increasing the bandwidth and making the antenna circularly polarized. From the simulation results, it was concluded that the proposed single element antenna provides a high gain and a broad bandwidth in spite of its simple design.

# CHAPTER 9

# COMPARISON WITH EXPERIMENT AND CONCLUSION

## 9.1 Experimental Set-Up

To compare the theoretical results, we performed various experiments with the HVAC ducts. The duct used in the experiments is of diameter 12.7 cm and is made up of galvanized steel as shown in Figure 9.1.

Figure 9.1. HVAC duct of diameter 12.7 cm and made up of galvanized steel

## 9.2 Transceiver Chipset

In order to characterize the 60 GHz system, we used the Tensorcom chipsets TC60G-USB3-EVB as the transmitter and receiver for the experiment as shown in Figure 9.2. The EVB is an 802.11ad/WiGig USB 3.0 dongle solution that includes a low-profile system in package having an IEEE 802.11ad/WiGig compliant PHY layer that supports the seven single-carrier (SC) PHY modes i.e., Modulation and Coding rates with a top end PHY rate of 1.9 Gbps. The 2 × 2 patch antenna excites waveguide modes in the duct system. The mm-wave signal propagates through the HVAC duct and is captured by the receiver EVB. Modes propagate with different group velocities and attenuation constants, experiencing multiple reflections from terminations and non-uniformities. The center frequency of the chipset is 59.40 GHz, and it supports a bandwidth of 2.16 GHz. Few other parameters for the EVB are transmitter EIRP = 14 dBm, the received signal tolerable EVM= -14 dB and the receiver sensitivity: -65 dBm. For the experiments in this work, we have used MCS_2 i.e., $\pi$/2-BPSK with a coding rate of 1/2. Modulation bandwidth for the transmitted signal is 1760 MHz.

Figure 9.2. Tensorcom EVB used as the transceiver in the HVAC duct experiments

The Tensorcom's chipsets come with a Linux based front end application (Speed Test). The Speed Test application provided with the chipset is used to evaluate the RF performance of Tensorcom's EVBs. We can select the beamforming sectors and the MCS for the transmitted data. The front-end application (shown in Figure 9.3) displays the signal to noise ratio, error vector magnitude, RSSI and the bit rate for the transmitted as well as the received data.

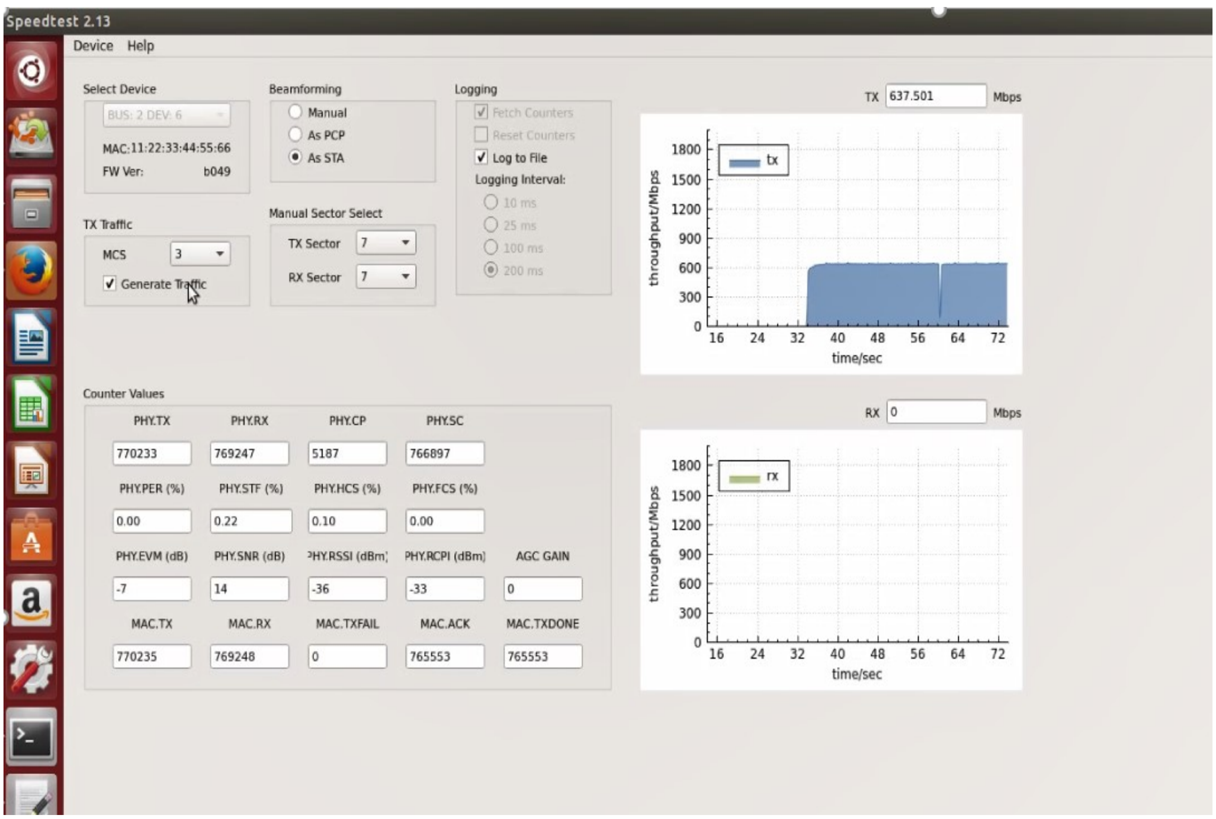


Figure 9.3. Speed-test GUI application for Tensorcom chipsets

The experimental setup is shown in Figure 9.4. The transmitter and receiver chipsets are connected to different laptops using USB dongles.

Figure 9.4. Tensorcom transceiver systems communicating through free space channel

### 9.3 Transceiver Antenna Simulation

Based on the antenna details provided with the chipset, we simulated the antenna radiation pattern. The design for the antenna which consists of 2x2 patch array (2 antennas for transmitter and 2 for receiver) is shown in Figure 9.5.

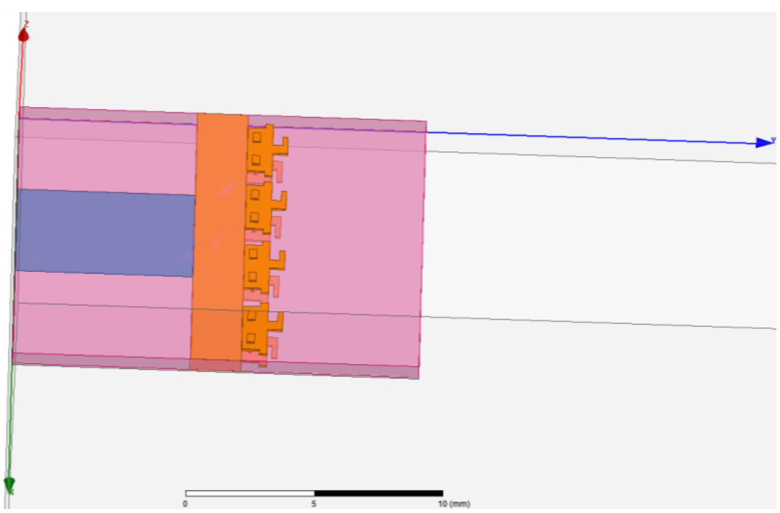

Figure 9.5. HFSS design of the dipole array antenna used in the experiments

The three-dimension (3D) gain and radiation pattern are around 8 dB in the vertical or $\theta$ direction relative to the axis of the antenna as shown in Figure 9.6.

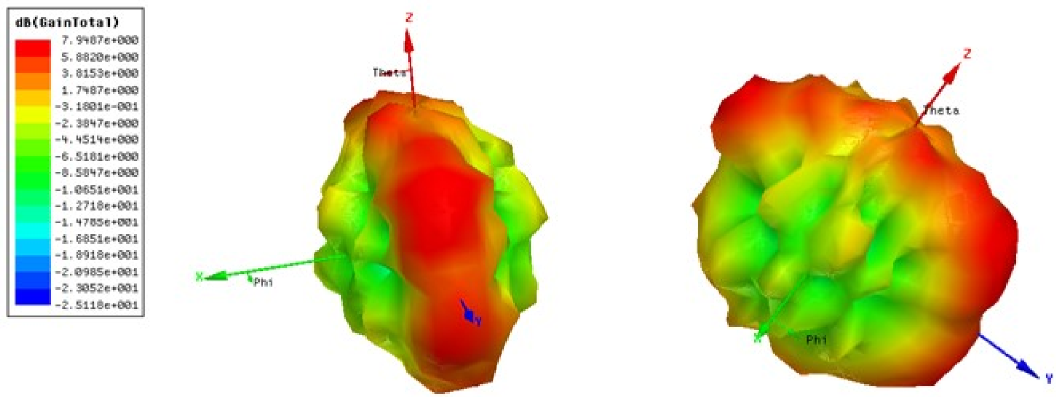


Figure 9.6. 3D radiation pattern and gain of the dipole array antenna using HFSS

Figure 9.7 shows the plot for the return loss for the dipole array antenna and we can see that the return loss in dBm goes up to −35 dBm at 61 GHz and the figure also shows that the bandwidth is around 2.16 GHz.

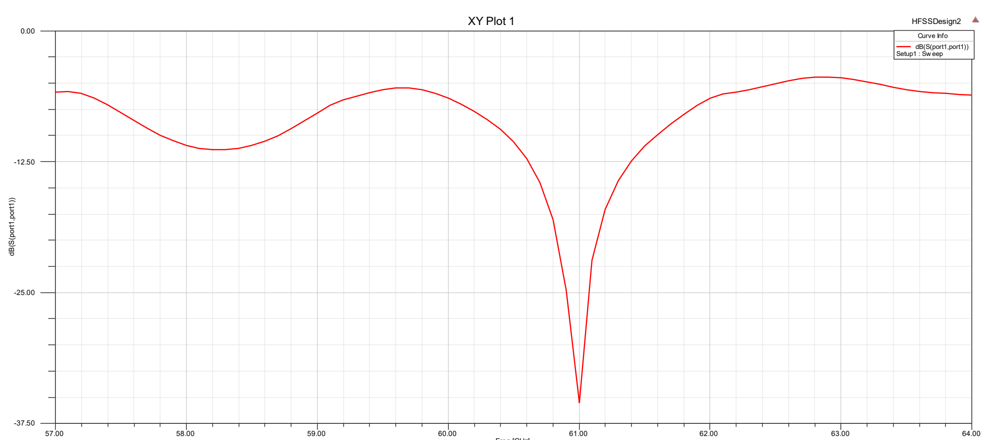


Figure 9.7. Return loss for simulated dipole array antenna using HFSS

We considered that the chipsets are inserted in a straight HVAC duct made up of galvanized steel and of diameter 12.7 cm with open ends as shown in Figure 9.8.

Figure 9.8. Tensorcom chipsets for mm-wave communication

### 9.4 Results for a Straight HVAC Duct

The analytical and experimental RSSI values for a straight waveguide of diameter 12.5 cm and length of 1 m, 2 m, 4 m and 8 m are shown in Figure 9.9.

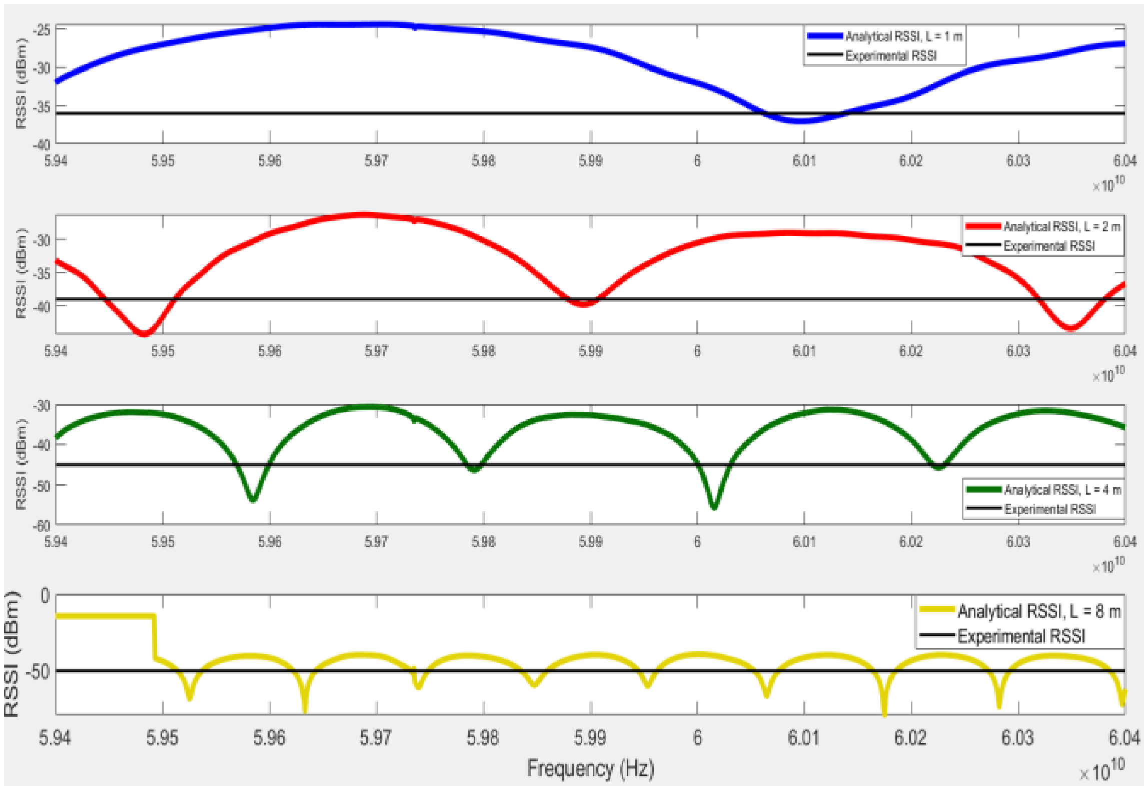

Figure 9.9. Theoretical and experimental RSSI values for a straight cylindrical duct

As the analytical and experimental results agree for a duct of length 8 m, analytical RSSI values are calculated for longer HVAC ducts. For a distance of 20 m and 50 m, the RSSI values are -59.3 dBm and -70 dBm, respectively.

In Table 9.1 we present different experimental parameters obtained using the speed-test application. We can see from the values, that a SNR of 5 dB and a bit rate of 630 Mbps is achieved for a distance of 8 m using HVAC ducts at 60 GHz.

Table 9.1. Experimental results obtained for various duct lengths

| Duct Length (m) | RSSI (dBm) | SNR (dB) | EVM (dB) | Bit Rate (Mbps) |
|---|---|---|---|---|
| 1 | -36 | 12 | -9 | 649 |
| 2 | -39 | 12 | -9 | 640 |
| 4 | -45 | 8 | -8 | 637 |
| 8 | -50 | 5 | -5 | 630 |

Table 9.2. Experimental results considering the alignment of transmitter

| Length | EVM (dB) | | SNR (dB) | | RSSI (dBm) | | RCPI (dBm) | | Throughput (Mbps) | |
|---|---|---|---|---|---|---|---|---|---|---|
| | Tx 0 | Tx 45 | Tx 0 | Tx 45 | Tx 0 | Tx 45 | Tx 0 | Tx 45 | Tx 0 | Tx 45 |
| 1.06 | -9.1 | -9.5 | 11.6 | 13 | -36.6 | -36 | -37.5 | -34.3 | 640.7 | 640.7 |
| 2.03 | -8.4 | -5 | 11.6 | 9.5 | -36 | -37 | -33 | -37 | 641 | 640.6 |
| 3.17 | -5 | -5.5 | 6.8 | 9 | -39.8 | -39.2 | -41.5 | -40.2 | 641 | 640.2 |
| 4.04 | -6.2 | -4.2 | 7.5 | 5.5 | -38.9 | -45 | -40.2 | -46.9 | 640.2 | 640.0 |
| 4.85 | -4.8 | -4.6 | 6.3 | 6.4 | -40.1 | -43.2 | -41.3 | -43 | 641.3 | 640.2 |

To understand the effect of the alignment of the transmitter and the receiver inside the HVAC duct, we performed experiments, by changing the orientation of either the transmitter or the receiver and recording the different physical parameters. EVM increases as we increase the length of the duct. SNR decreases as we increase the length of the duct. RSSI increases as we increase the length of the duct. RCPI increases as we increase the length of the duct. Throughput remains almost constant as we increase the length of the duct. However small decrease in throughput for transmitter launch angle 45 as compared to transmitter launch angle 0.

Further we looked at the different RF parameters when both the transmitter and receiver are at $90^{\circ}$ orientation. In this particular scenario, the maximum amount of radiation will be towards the HVAC duct walls. However, the radiation pattern of the transmitter and receiver pattern used in this experiment is of very wide beam-width covering upto $\pm 60°$. Therefore, we observed that in this case the results were exactly same as the case when the transmitter and the receiver were aligned and kept at 0°. The other observation is about the relative alignment of the transmitter and the receiver. If the transmitter and the receiver are aligned in the same direction, then their alignment with respect to the HVAC duct does not have any effect on the signal transmission or reception.

Finally, to compare the results for the HVAC duct to the free space, we compare the analytical and simulation throughput (bits per second in GHz) results for a 16 QAM modulation. The length of the duct considered is 4.6 m which is same as the distance between the transmitter and the receiver in free space. The analytical and simulation results are very close for the HVAC duct. For the analytical values, we take an average of the parameter values obtained over the different frequency points. Further, as compared to the free space simulation, we can see that the bit rate achieved for the HVAC duct is almost double than that of the free space for the various SNR values.

Table 9.3. Comparison of analytical and simulated throughput for HVAC and free-space

| SNR (dB) | HVAC Duct | | Free-Space | |
|---|---|---|---|---|
| | Analytical | Simulation | Analytical | Simulation |
| 5 | 5.15 | 5.1 | 2.06 | 2.12 |
| 10 | 9.08 | 8.98 | 3.24 | 3.31 |
| 15 | 13.5 | 13.02 | 4.35 | 4.43 |
| 20 | 21.6 | 20.4 | 6.39 | 6.46 |
| 25 | 29.12 | 27.08 | 7.96 | 8.05 |
| 30 | 35.7 | 32.77 | 9.19 | 9.20 |

Discussion

A simple mechanism for the distribution of mm-wave signals at extremely high data rates (630 Mbps for a distance of 8 m) using HVAC ducts in an indoor environment was proposed. Channel frequency response for the duct system was obtained and the results showed an attenuation of -30 dB, which is very low compared to that of the free space path loss. Calculation of other channel parameters and experiments for different MCS and larger distances are in progress. However, it suffices to say that the HVAC ducts can serve as a reliable means to provide indoor communication at a very high data rate.

## 9.5 Results for HVAC Duct with a Bend

To validate the model, we performed experiments with a circular HVAC duct of diameter 12.7 cm made of galvanized steel. For the experiment we used the Tensorcom chipsets TC60G-USB3-EVB as the transmitter and receiver. The TC60G-USB3-EVB evaluation system includes a low-profile SiP having an IEEE 802.11ad/WiGig compliant PHY layer that supports the seven single-carrier (SC) PHY modes (MCS_1 through MCS_7) with a top end PHY rate of 1.9 Gbps. For the experiments in this work, we have used MCS_2 i.e., $\pi$/2-BPSK with a coding rate of 1/2. Modulation bandwidth for the transmitted signal is 1760 MHz. The Speed Test application provided with the chipset is used to evaluate the RF performance of Tensorcom's EVBs.

Figure 9.10 shows the HVAC duct section bent at angles (a) 45°, (b) 90° and (c) 180°. The data recorded using the speed test application generates the experimental RSSI values for ducts of length 4 m and 8 m and bend angles 0°(straight), 45°, 90° and 180° (U shape) and diameter 12.7 cm with open ends. These values are compared against the theoretical RSSI values obtained using (1) and (3) (we consider all the relevant modes) in Table 9.4. Other system parameters used are as follows: $R$ = 20 $cm$, $\phi$ = 0°, 45°, 90° and 180°.

(a)

(b)

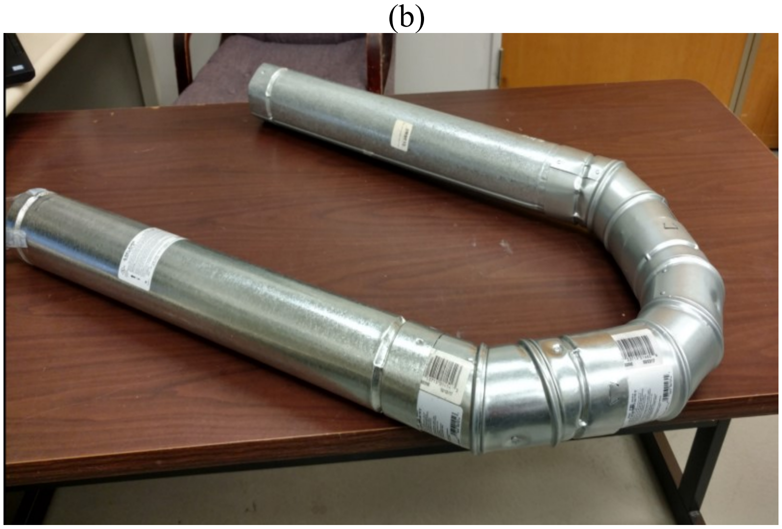

(c)

Figure 9.10. HVAC duct section bent at angles (a) 45°, (b) 90° and (c) 180°

Table 9.4. Comparison of analytical and experimental RSSI for HVAC duct

| Duct Length (m) | Bend Angle (degrees) | Analytical RSSI (dBm) | Experimental RSSI (dBm) | Experimental Throughput (Mbps) |
|---|---|---|---|---|
| 4 | 0 | -32.77 | -37 | 543.70 |
| 4 | 45 | -40.08 | -40 | 542.40 |
| 4 | 90 | -45.22 | -44 | 544.93 |
| 4 | 180 | -41.04 | -42 | 542.63 |
| 8 | 0 | -37.50 | -38 | 543.20 |
| 8 | 45 | -43.91 | -44 | 543.90 |
| 8 | 90 | -48.65 | -48 | 543.50 |
| 8 | 180 | -46.47 | -48 | 542.20 |

To understand the effect of the alignment of the transmitter and the receiver inside the HVAC duct which has bends, we performed experiments, by changing the orientation of either the transmitter or the receiver and recording the different physical parameters. In this particular experiment, we considered the duct bent at 90°. EVM increases as we increase the length of the duct. SNR decreases as we increase the length of the duct. RSSI increases as we increase the length of the duct. RCPI increases as we increase the length of the duct. Throughput remains almost constant as we increase the length of the duct. However small decrease in throughput for transmitter launch angle 45 as compared to transmitter (Tx) launch angle 0.

Table 9.5. Experimental result for 90° Bent HVAC duct and Tx launch angle 45°

| Length (m) | EVM (dB) | SNR (dB) | RSSI (dBm) | RCPI (dBm) | Throughput (Mbps) |
|---|---|---|---|---|---|
| 1.0668 | -5.75 | 9.37 | -39.75 | -41.1 | 640.77 |
| 2.032 | -5.04 | 8.73 | -39.95 | -41.34 | 639.56 |
| 3.175 | -3.99 | 7.87 | -40.27 | -42.25 | 638.9 |
| 4.0386 | -3.67 | 5.75 | -41.26 | -43.29 | 638.87 |
| 4.8514 | -3.13 | 3.92 | -42.94 | -44.52 | 637.28 |

# REFERENCES


[1] A. N. Uwaechia and N. M. Mahyuddin, "A Comprehensive Survey on Millimeter Wave Communications for Fifth-Generation Wireless Networks: Feasibility and Challenges," in IEEE Access, vol. 8, pp. 62367-62414, 2020, doi: 10.1109/ACCESS.2020.2984204.

[2] J. Huang, R. Feng, J. Sun, C. Wang, W. Zhang and Y. Yang, "Comparison of Propagation Channel Characteristics for Multiple Millimeter Wave Bands," 2017 IEEE 85th Vehicular Technology Conference (VTC Spring), 2017, pp. 1-5, doi: 10.1109/VTCSpring.2017.8108205.

[3] T. S. Rappaport et al., "Millimeter Wave Mobile Communications for 5G Cellular: It Will Work!," in IEEE Access, vol. 1, pp. 335-349, 2013, doi: 10.1109/ACCESS.2013.2260813.

[4] S. Geng, J. Kivinen, X. Zhao and P. Vainikainen, "Millimeter-Wave Propagation Channel Characterization for Short-Range Wireless Communications," in IEEE Transactions on Vehicular Technology, vol. 58, no. 1, pp. 3-13, Jan. 2009, doi: 10.1109/TVT.2008.924990.

[5] S. Horikoshi, M. Fuji, M. Itami and K. Itoh, "A study on multipath propagation modeling in millimeter wave IVC," The 5th International Symposium on Wireless Personal Multimedia Communications, 2002, pp. 286-290 vol.1, doi: 10.1109/WPMC.2002.1088178.

[6] T. S. Rappaport, Y. Qiao, J. I. Tamir, J. N. Murdock and E. Ben-Dor, "Cellular broadband millimeter wave propagation and angle of arrival for adaptive beam steering systems (invited paper)," 2012 IEEE Radio and Wireless Symposium, 2012, pp. 151-154, doi: 10.1109/RWS.2012.6175397.

[7] S. G. Larew, T. A. Thomas, M. Cudak and A. Ghosh, "Air interface design and ray tracing study for 5G millimeter wave communications," 2013 IEEE Globecom Workshops (GC Wkshps), 2013, pp. 117-122, doi: 10.1109/GLOCOMW.2013.6824972.

[8] K. Guan et al., "Channel Sounding and Ray Tracing for Intrawagon Scenario at mm-wave and Sub-mm-wave Bands," in IEEE Transactions on Antennas and Propagation, vol. 69, no. 2, pp. 1007-1019, Feb. 2021, doi: 10.1109/TAP.2020.3016399.

[9] F. Huang, J. Zhou, Z. Yu, B. Yang, J. Lan and W. Huang, "The research of broadband MIMO millimeter wave transceiver system: Design and test," 2016 IEEE Asia Pacific Conference on Circuits and Systems (APCCAS), 2016, pp. 176-179, doi: 10.1109/APCCAS.2016.7803926.

[10] J. Chen, W. Lin, P. Yan, J. Xu, D. Hou and W. Hong, "Design of mm-Wave transmitter and receiver for 5G," 2017 10th Global Symposium on Millimeter-Waves, 2017, pp. 92-93, doi: 10.1109/GSMM.2017.7970330.

[11] T. Ninomiya, T. Saito, Y. Ohashi and H. Yatsuka, "60-GHz transceiver for high-speed wireless LAN system," 1996 IEEE MTT-S International Microwave Symposium Digest, 1996, pp. 1171-1174 vol.2, doi: 10.1109/MWSYM.1996.511238.

[12] S. K. Reynolds et al., "A 16-element phased-array receiver IC for 60-GHz communications in SiGe BiCMOS," 2010 IEEE Radio Frequency Integrated Circuits Symposium, 2010, pp. 461-464, doi: 10.1109/RFIC.2010.5477306.

[13] A. Babakhani, X. Guan, A. Komijani, A. Natarajan and A. Hajimiri, "A 77-GHz Phased-Array Transceiver With On-Chip Antennas in Silicon: Receiver and Antennas," in IEEE Journal of Solid-State Circuits, vol. 41, no. 12, pp. 2795-2806, Dec. 2006, doi: 10.1109/JSSC.2006.884811.

[14] S. Kato et al., "Single carrier transmission for multi-gigabit 60-GHz WPAN systems," in IEEE Journal on Selected Areas in Communications, vol. 27, no. 8, pp. 1466-1478, October 2009, doi: 10.1109/JSAC.2009.091016.

[15] S. Dutta, M. Mezzavilla, R. Ford, M. Zhang, S. Rangan and M. Zorzi, "Frame Structure Design and Analysis for Millimeter Wave Cellular Systems," in IEEE Transactions on Wireless Communications, vol. 16, no. 3, pp. 1508-1522, March 2017, doi: 10.1109/TWC.2017.2647803.

[16] T. Zwick, T. J. Beukema and Haewoon Nam, "Wideband channel sounder with measurements and model for the 60 GHz indoor radio channel," in IEEE Transactions on Vehicular Technology, vol. 54, no. 4, pp. 1266-1277, July 2005, doi: 10.1109/TVT.2005.851354.

[17] Haibing Yang, Smulders and Herben, "Indoor Channel Measurements and Analysis in the Frequency Bands 2 GHz and 60 GHz," 2005 IEEE 16th International Symposium on Personal, Indoor and Mobile Radio Communications, 2005, pp. 579-583, doi: 10.1109/PIMRC.2005.1651502.

[18] J. Wang, R. V. Prasad and I. Niemegeers, "Analyzing 60 GHz radio links for indoor communications," in IEEE Transactions on Consumer Electronics, vol. 55, no. 4, pp. 1832-1840, November 2009, doi: 10.1109/TCE.2009.5373739.

[19] D. He et al., "Channel Measurement, Simulation, and Analysis for High-Speed Railway Communications in 5G Millimeter-Wave Band," in IEEE Transactions on Intelligent Transportation Systems, vol. 19, no. 10, pp. 3144-3158, Oct. 2018, doi: 10.1109/TITS.2017.2771559.

[20] J. Kibiłda et al., "Indoor Millimeter-Wave Systems: Design and Performance Evaluation," in Proceedings of the IEEE, vol. 108, no. 6, pp. 923-944, June 2020, doi: 10.1109/JPROC.2020.2989189.

[21] S. Deng, M. K. Samimi and T. S. Rappaport, "28 GHz and 73 GHz millimeter-wave indoor propagation measurements and path loss models," 2015 IEEE International Conference on Communication Workshop (ICCW), 2015, pp. 1244-1250, doi: 10.1109/ICCW.2015.7247348.

[22] V. Semkin, A. Karttunen, J. Järveläinen, S. Andreev and Y. Koucheryavy, "Static and dynamic millimeter-wave channel measurements at 60 GHz in a conference room," 12th European Conference on Antennas and Propagation (EuCAP 2018), 2018, pp. 1-5, doi: 10.1049/cp.2018.0701.

[23] M. Kim, S. Kishimoto, S. Yamakawa and K. Guan, "Millimeter-Wave Intra-Cluster Channel Model for In-Room Access Scenarios," in IEEE Access, vol. 8, pp. 82042-82053, 2020, doi: 10.1109/ACCESS.2020.2991044.

[24] M. Fernández, L. Zhang, S. L. Cotton and D. Guerra, "Path Loss Measurements of User Equipment to Access Point Communications at 60 GHz," 2020 IEEE International Symposium on Broadband Multimedia Systems and Broadcasting (BMSB), 2020, pp. 1-5, doi: 10.1109/BMSB49480.2020.9379818.

[25] S. Balakrishnan et al., "60 GHz Multipath Propagation Analysis and Inference for an Indoor Scenario," 2020 IEEE 92nd Vehicular Technology Conference (VTC2020-Fall), 2020, pp. 1-5, doi: 10.1109/VTC2020-Fall49728.2020.9348806.

[26] M. E. Hajj, G. El Zein, G. Zaharia, H. Farhat and S. Sadek, "Angular Measurements and Analysis of the Indoor Propagation Channel at 60 GHz," 2019 International Conference on Wireless and Mobile Computing, Networking and Communications (WiMob), 2019, pp. 121-126, doi: 10.1109/WiMOB.2019.8923261.

[27] M. E. Hajj, G. Zaharia, G. El Zein, H. Farhat and S. Sadek, "Millimeter-Wave Propagation Measurements at 60 GHz in Indoor Environments," 2019 International Symposium on Signals, Circuits and Systems (ISSCS), 2019, pp. 1-4, doi: 10.1109/ISSCS.2019.8801751.

[28] N. Moraitis and P. Constantinou, "Indoor channel measurements and characterization at 60 GHz for wireless local area network applications," in IEEE Transactions on Antennas and Propagation, vol. 52, no. 12, pp. 3180-3189, Dec. 2004, doi: 10.1109/TAP.2004.836422.

[29] G. R. Maccartney, T. S. Rappaport, S. Sun and S. Deng, "Indoor Office Wideband Millimeter-Wave Propagation Measurements and Channel Models at 28 and 73 GHz for Ultra-Dense 5G Wireless Networks," in IEEE Access, vol. 3, pp. 2388-2424, 2015, doi: 10.1109/ACCESS.2015.2486778.

[30] P. F. M. Smulders, "Statistical Characterization of 60-GHz Indoor Radio Channels," in IEEE Transactions on Antennas and Propagation, vol. 57, no. 10, pp. 2820-2829, Oct. 2009, doi: 10.1109/TAP.2009.2030524.

[31] B. Ai et al., "On Indoor Millimeter Wave Massive MIMO Channels: Measurement and Simulation," in IEEE Journal on Selected Areas in Communications, vol. 35, no. 7, pp. 1678-1690, July 2017, doi: 10.1109/JSAC.2017.2698780.

[32] C. R. Anderson et al., "In-building wideband multipath characteristics at 2.5 and 60 GHz," Proceedings IEEE 56th Vehicular Technology Conference, 2002, pp. 97-101 vol.1, doi: 10.1109/VETECF.2002.1040310.

[33] P. Nobles and F. Halsall, "Indoor propagation at 17 GHz and 60 GHz-measurements and modelling," IEE National Conference on Antennas and Propagation, 1999, pp. 93-96, doi: 10.1049/cp:19990022.

[34] Yuksekkaya, B. (2017). Indoor Channel Modelling for SISO and Massive SIMO in the 60 GHz mm-Wave Band. Elektronika Ir Elektrotechnika, 23(4), 39-44. https://doi.org/10.5755/j01.eie.23.4.18720.

[35] A. Karstensen, Wei Fan, I. Carton and G. F. Pedersen, "Comparison of ray tracing simulations and channel measurements at mm-wave bands for indoor scenarios," 2016 10th European Conference on Antennas and Propagation (EuCAP), 2016, pp. 1-5, doi: 10.1109/EuCAP.2016.7481361.

[36] A. Zhou, J. Huang, J. Sun, Q. Zhu, C. Wang and Y. Yang, "60 GHz channel measurements and ray tracing modeling in an indoor environment," 2017 9th International Conference on Wireless Communications and Signal Processing (WCSP), 2017, pp. 1-6, doi: 10.1109/WCSP.2017.8170934.

[37] X. Wu et al., "60-GHz Millimeter-Wave Channel Measurements and Modeling for Indoor Office Environments," in IEEE Transactions on Antennas and Propagation, vol. 65, no. 4, pp. 1912-1924, April 2017, doi: 10.1109/TAP.2017.2669721.

[38] G. V. Eleftheriades, A. S. Omar, and L. P. B. Katehi G. M. Rebeiz, “Some important properties of waveguide junction generalized scattering matrices in the context of the mode matching technique,” IEEE Transactions on Microwave Theory and Techniques, vol. 42, no. 10, pp. 1896–1903, October 1984.

[39] M. A. Mustafar et al., "Milimeter-Wave Beamforming MIMO Antenna Design for 5G Wireless Applications," 2018 IEEE International RF and Microwave Conference (RFM), 2018, pp. 9-12, doi: 10.1109/RFM.2018.8846545.

[40] M. A. Almasi, R. Amiri, H. Jafarkhani and H. Mehrpouyan, "mm-wave Lens-Based MIMO System for Suppressing Small-Scale Fading and Shadowing," in IEEE

Transactions on Wireless Communications, vol. 19, no. 8, pp. 5292-5306, Aug. 2020, doi: 10.1109/TWC.2020.2991776.

[41] Z. Genc, W. V. Thillo, A. Bourdoux and E. Onur, "60 GHz PHY Performance Evaluation with 3D Ray Tracing under Human Shadowing," in IEEE Wireless Communications Letters, vol. 1, no. 2, pp. 117-120, April 2012, doi: 10.1109/WCL.2012.022012.120033.

[42] S. Yang, J. Zhang and J. Zhang, "Impact of Foliage on Urban Mm-wave Wireless Propagation Channel: A Ray-tracing Based Analysis," 2019 International Symposium on Antennas and Propagation (ISAP), 2019, pp. 1-3.

[43] J. Lee, J. Choi, J. Lee and S. Kim, "Permittivity Effect of Building Materials on 28 GHz mm-wave Channel Using 3D Ray Tracing Simulation," GLOBECOM 2017 - 2017 IEEE Global Communications Conference, 2017, pp. 1-6, doi: 10.1109/GLOCOM.2017.8254893.

[44] A. L. Freire et al., "Polarimetric Diffuse Scattering Channel Measurements at 26 GHz and 60 GHz," 2018 IEEE 29th Annual International Symposium on Personal, Indoor and Mobile Radio Communications (PIMRC), 2018, pp. 210-214, doi: 10.1109/PIMRC.2018.8581035.

[45] A. Al-Hourani, "On the Probability of Line-of-Sight in Urban Environments," in IEEE Wireless Communications Letters, vol. 9, no. 8, pp. 1178-1181, Aug. 2020, doi: 10.1109/LWC.2020.2984497.

[46] K. Hassan, M. Masarra, M. Zwingelstein and I. Dayoub, "Channel Estimation Techniques for Millimeter-Wave Communication Systems: Achievements and Challenges," in IEEE Open Journal of the Communications Society, vol. 1, pp. 1336-1363, 2020, doi: 10.1109/OJCOMS.2020.3015394.

[47] P. Zhang, J. Li, H. Wang, H. Wang and W. Hong, "Indoor Small-Scale Spatiotemporal Propagation Characteristics at Multiple Millimeter-Wave Bands," in IEEE Antennas and Wireless Propagation Letters, vol. 17, no. 12, pp. 2250-2254, Dec. 2018, doi: 10.1109/LAWP.2018.2872051.

[48] Alkhawatrah, Mohammad & Qasem, Nidal. (2016). Improving and Extending Indoor Connectivity Using Relay Nodes for 60 GHz Applications. International Journal of Advanced Computer Science and Applications. 7. 10.14569/IJACSA.2016.070456.

[49] S. G. Larew, T. A. Thomas, M. Cudak and A. Ghosh, " Air interface design and ray tracing study for 5G millimeter wave communications," 2013 IEEE Globecom Workshops (GC Wkshps), 2013, pp. 117-122, doi: 10.1109/GLOCOMW.2013.6824972.

[50] Y. You and L. Zhang, "Bayesian Matching Pursuit-Based Channel Estimation for Millimeter Wave Communication," in IEEE Communications Letters, vol. 24, no. 2, pp. 344-348, Feb. 2020, doi: 10.1109/LCOMM.2019.2953706.

[51] F. Fuschini, M. Zoli, E. M. Vitucci, M. Barbiroli and V. Degli-Esposti, "A Study on Millimeter-Wave Multiuser Directional Beamforming Based on Measurements and Ray Tracing Simulations," in IEEE Transactions on Antennas and Propagation, vol. 67, no. 4, pp. 2633-2644, April 2019, doi: 10.1109/TAP.2019.2894271.

[52] W. Khawaja, O. Ozdemir, Y. Yapici, F. Erden and I. Guvenc, "Coverage Enhancement for NLOS mm-wave Links Using Passive Reflectors," in IEEE Open Journal of the Communications Society, vol. 1, pp. 263-281, 2020, doi: 10.1109/OJCOMS.2020.2969751.

[53] E. Bangar, N. Taherkhani and K. Kiasaleh, "Characterization of Indoor Heating, Ventilation and Air Conditioning Duct System as a Communication Channel at 60 GHz," 2020 IEEE Texas Symposium on Wireless and Microwave Circuits and Systems (WMCS), 2020, pp. 1-7, doi: 10.1109/WMCS49442.2020.9172409.

[54] E. Bangar and K. Kiasaleh, "Experimental Validation of the Performance of Heating, Ventilation and Air Conditioning Ducts as Communication Channel at 60 GHz," 2020 IEEE International Symposium on Local and Metropolitan Area Networks (LANMAN, 2020, pp. 1-2, doi :10.1109/LANMAN49260.2020.9153253

[55] E. M. Vitucci et al., "A Study on Dual-Directional Mm-wave Indoor Channel Characteristics," 2019 13th European Conference on Antennas and Propagation (EuCAP), 2019, pp. 1-5.

[56] P. V. Nikitin, D. D. Stancil, O. K. Tonguz, A. E. Xhafa, A. G. Cepni and D. Brodtkorb, "RF propagation in an HVAC duct system: impulse response characteristics of the channel," IEEE Antennas and Propagation Society International Symposium (IEEE Cat. No.02CH37313), 2002, pp. 726-729 vol.2, doi: 10.1109/APS.2002.1016748.

[57] M. J. Kazemi, A. Abdipur and A. Mohammadi, "Indoor propagation MIMO channel modeling in 60 GHz using SBR based 3D ray tracing technique," 2012 Second Conference on Millimeter-Wave and Terahertz Technologies (MMWaTT), 2012, pp. 25-28, doi: 10.1109/MMWaTT.2012.6532159.

[58] M. Kacou, V. Guillet, G. El Zein and G. Zaharia, "Coverage and Throughput Analysis at 60 GHz for Indoor WLAN with Indirect Paths," 2018 IEEE 29th Annual International Symposium on Personal, Indoor and Mobile Radio Communications (PIMRC), 2018, pp. 1-5, doi: 10.1109/PIMRC.2018.8580903.

[59] P. V. Nikitin (2002), Analysis of Heating, Ventilation, And Air Conditioning Ducts as a Radio Frequency Communication Channel, (dissertation submitted to the graduate school). Carnegie Mellon University, Pittsburgh, Pennsylvania, US.

[60] P. V. Nikitin and D. D. Stancil, "Antenna radiation resistance in waveguide and in free-space," in IEEE Transactions on Antennas and Propagation, vol. 53, no. 6, pp. 2126-2128, June 2005, doi: 10.1109/TAP.2005.848524.

[61] P. V. Nikitin et al., "Antennas in a waveguide propagation environment," IEEE Antennas and Propagation Society International Symposium. Digest. Held in conjunction with: USNC/CNC/URSI North American Radio Sci. Meeting (Cat. No.03CH37450), 2003, pp. 1181-1184 vol.2, doi: 10.1109/APS.2003.1219446.

[62] P. V. Nikitin and D. D. Stancil, "Connection between radiation resistances of antenna in rectangular waveguide and in free-space," IEEE Antennas and Propagation Society Symposium, 2004., 2004, pp. 2035-2038 Vol.2, doi: 10.1109/APS.2004.1330607.

[63] V. Subramaniam, G. N. De Brabander, D. H. Naghski and J. T. Boyd, "Measurement of mode field profiles and bending and transition losses in curved optical channel waveguides," in Journal of Lightwave Technology, vol. 15, no. 6, pp. 990-997, June 1997, doi: 10.1109/50.588672.

[64] W. W. S. Lee and E. K. N. Yung, "The input impedance of a coaxial line fed probe in a cylindrical waveguide," in IEEE Transactions on Microwave Theory and Techniques, vol. 42, no. 8, pp. 1468-1473, Aug. 1994, doi: 10.1109/22.297808.

[65] R. G. Kouyoumjian and P. H. Pathak, "A uniform geometrical theory of diffraction for an edge in a perfectly conducting surface," in Proceedings of the IEEE, vol. 62, no. 11, pp. 1448-1461, Nov. 1974, doi: 10.1109/PROC.1974.9651.

[66] D. G. Dudley and S. F. Mahmoud, "Linear source in a circular tunnel," in IEEE Transactions on Antennas and Propagation, vol. 54, no. 7, pp. 2034-2047, July 2006, doi: 10.1109/TAP.2006.877195.

[67] C. Zhou and J. Waynert, "The Equivalence of the Ray Tracing and Modal Methods for Modeling Radio Propagation in Lossy Rectangular Tunnels," in IEEE Antennas and Wireless Propagation Letters, vol. 13, pp. 615-618, 2014, doi: 10.1109/LAWP.2014.2313312.

[68] P. V. Nikitin, D. D. Stancil, A. G. Cepni, A. E. Xhafa, O. K. Tonguz and D. Brodtkorb, "Propagation modelling of complex HVAC networks using transfer matrix method [indoor communication application]," IEEE Antennas and Propagation Society International Symposium. Digest. Held in conjunction with: USNC/CNC/URSI North American Radio Sci. Meeting (Cat. No.03CH37450), 2003, pp. 126-129 vol.2, doi: 10.1109/APS.2003.1219195.

[69] K. Witrisal, "On estimating the RMS delay spread from the frequency-domain level crossing rate," in IEEE Communications Letters, vol. 5, no. 7, pp. 287-289, July 2001, doi: 10.1109/4234.935744.

[70] K. Kim, M. Kim, J. Park, J. Lee, J. Liang and B. Park, "Joint probability distribution of power delay profiles based on 28 GHz channel measurements," 2016 IEEE-APS Topical Conference on Antennas and Propagation in Wireless Communications (APWC), 2016, pp. 187-190, doi: 10.1109/APWC.2016.7738153.

[71] P. V. Nikitin, D. D. Stancil, O. K. Tonguz, A. E. Xhafa, A. G. Cepni and D. Brodtkorb, "Impulse response of the HVAC duct as a communication channel," in IEEE Transactions on Communications, vol. 51, no. 10, pp. 1736-1742, Oct. 2003, doi: 10.1109/TCOMM.2003.818098.

[72] R. S. Jini and M. N. Upama Rajan, "FPGA Based Low Power OFDM Transceiver For 60GHz millimeter Wave Wireless Communication Systems," 2019 9th International Conference on Advances in Computing and Communication (ICACC), 2019, pp. 147-151, doi: 10.1109/ICACC48162.2019.8986175.

[73] M. S. Sim, Y. Lim, S. H. Park, L. Dai and C. Chae, "Deep Learning-Based mm-wave Beam Selection for 5G NR/6G With Sub-6 GHz Channel Information: Algorithms and Prototype Validation," in IEEE Access, vol. 8, pp. 51634-51646, 2020, doi: 10.1109/ACCESS.2020.2980285.

[74] H. Ding and K. G. Shin, "Accurate Angular Inference for 802.11ad Devices Using Beam-Specific Measurements," in IEEE Transactions on Mobile Computing, doi: 10.1109/TMC.2020.3015936.

[75] R. P. Torres, L. Valle, M. Domingo, S. Loredo and M. C. Diez, "CINDOOR: an engineering tool for planning and design of wireless systems in enclosed spaces," in IEEE Antennas and Propagation Magazine, vol. 41, no. 4, pp. 11-22, Aug. 1999, doi: 10.1109/74.789733.

[76] R. F. Harrington, “Time-Harmonic Electromagnetic Fields”, McGraw-Hill, New York, NY, 1961.

[77] J. Molina-Garcia-Pardo, M. Liénard and P. Degauque, "Modal theory for interpreting path loss and MIMO capacity in a tunnel excited by an outside antenna," 2012 8th International Wireless Communications and Mobile Computing Conference (IWCMC), 2012, pp. 1165-1168, doi: 10.1109/IWCMC.2012.6314371.

[78] P. V. Nikitin (2002), Analysis of Heating, Ventilation, And Air Conditioning Ducts as a Radio Frequency Communication Channel, (dissertation submitted to the graduate school). Carnegie Mellon University, Pittsburgh, Pennsylvania, US.

[79] Chenming Zhou, Joseph Waynert, Timothy Plass, and Ronald Jacksha, "Attenuation Constants of Radio Waves in Lossy-Walled Rectangular Waveguides," Progress In Electromagnetics Research, Vol. 142, 75-105, 2013, doi:10.2528/PIER13061709

[80] P. V. Nikitin, D. D. Stancil, A. G. Cepni, O. K. Tonguz, A. E. Xhafa and D. Brodtkorb, "Propagation model for the HVAC duct as a communication channel," in IEEE Transactions on Antennas and Propagation, vol. 51, no. 5, pp. 945-951, May 2003.

[81] H.-W. Glock and U. van Rienen, “An iterative algorithm to evaluate multimodal S-parameter measurements,” IEEE Transactions on Magnetics, vol. 36, no. 4, pp. 1841–1845, July 2000.

[82] H.-W. Glock, F. Marhauser, P. Hulsmann, M. Kurz, and H. Klein, “Analysis of HOM interaction between cavities by multimodal s-parameter measurements,” Proceedings of the 1997 Particle Accelerator Conference, vol. 1, no. 1, pp. 521–523, 1997.

[83] A. Weisshaar, S. M. Goodnick, and V. K. Tripathi, “A rigorous and efficient method of moments solution for curved waveguide bends,” IEEE Transactions on Microwave Theory and Techniques, vol. 40, no. 12, pp. 2200–2206, 1992.

[84] Guo-Xin Fan and Qing Huo Liu, “Dyadic Green’s functions for curved waveguides and cavities and their reformulation,” Antennas and Propagation Society International Symposium, no. 3, pp. 1504–1507, 1998.

[85] A. Weisshaar, M. Mongiardo, and V. K. Tripathi, “Accurate and efficient CAD-oriented modeling of circular waveguide bends,” MTT-S International Microwave Symposium Digest, vol. 3, pp. 1591–1594, 1997.

[86] M. H. Kermani and M. Kamarei, "A ray-tracing method for predicting delay spread in tunnel environments," 2000 IEEE International Conference on Personal Wireless Communications. Conference Proceedings (Cat. No.00TH8488), 2000, pp. 538-542, doi: 10.1109/ICPWC.2000.905917.

[87] T. Holt, K. Pahlavan and J. F. Lee, "A graphical indoor radio channel simulator using 2D ray tracing," [1992 Proceedings] The Third IEEE International Symposium on Personal, Indoor and Mobile Radio Communications, 1992, pp. 411-416, doi: 10.1109/PIMRC.1992.279896.

[88] Z. Yun and M. F. Iskander, "Ray Tracing for Radio Propagation Modeling: Principles and Applications," in IEEE Access, vol. 3, pp. 1089-1100, 2015, doi: 10.1109/ACCESS.2015.2453991.

[89] E. Gunduzalp, G. Yildirim and Y. Tatar, "Radio Propagation Prediction Using SBR in a Tunnel with Narrow Cross-Section and Obstacles," 2019 International Conference on

Applied Automation and Industrial Diagnostics (ICAAID), 2019, pp. 1-6, doi: 10.1109/ICAAID.2019.8934973.

[90] C. G. Liu, E. T. Zhang, Z. P. Wu and B. Zhang, "Modelling radio wave propagation in tunnels with ray-tracing method," 2013 7th European Conference on Antennas and Propagation (EuCAP), 2013, pp. 2317-2321.

[91] M. Comiter et al., "Millimeter-Wave Field Experiments with Many Antenna Configurations for Indoor Multipath Environments," 2017 IEEE Globecom Workshops (GC Wkshps), 2017, pp. 1-6, doi: 10.1109/GLOCOMW.2017.8269033.

[92] M. U. Sheikh, K. Ruttik, R. Jäntti and J. Hämäläinen, "Measurements and Ray Tracing Simulations: Impact of Different Antenna Positions on Meeting Room Coverage at 60 GHz," 2020 European Conference on Networks and Communications (EuCNC), 2020, pp. 63-67, doi: 10.1109/EuCNC48522.2020.9200969.

[93] K. Chandra, R. V. Prasad, B. Quang and I. G. M. M. Niemegeers, "CogCell: cognitive interplay between 60 GHz picocells and 2.4/5 GHz hotspots in the 5G era," in IEEE Communications Magazine, vol. 53, no. 7, pp. 118-125, July 2015, doi: 10.1109/MCOM.2015.7158274.

[94] G. Yue, D. Yu, H. Qiu, K. Guan, L. Yang and Q. Lv, "Measurements and Ray Tracing Simulations for Non-Line-of-Sight Millimeter-Wave Channels in a Confined Corridor Environment," in IEEE Access, vol. 7, pp. 85066-85081, 2019, doi: 10.1109/ACCESS.2019.2924510.

[95] S. Li, Y. Liu, L. Lin, D. Sun, S. Yang and X. Sun, "Simulation and Modeling of Millimeter-Wave Channel at 60 GHz in Indoor Environment for 5G Wireless Communication System," 2018 IEEE International Conference on Computational Electromagnetics (ICCEM), 2018, pp. 1-3, doi: 10.1109/COMPEM.2018.8496691.

[96] Y. Kimura and Y. Tsunemitsu, "Analysis of Effective Coverage Area in 60GHz-Band Millimeter Wave Wireless LAN for High Speed Railway Passenger Car and Indoor Room," 2019 International Symposium on Antennas and Propagation (ISAP), 2019, pp. 1-3.

[97] D. Sun, Y. Liu and S. Li, "Simulation and Analysis of 60GHz Millimeter-Wave Propagation Characteristics in Corridor Environment," 2018 International Conference on Microwave and Millimeter Wave Technology (ICMMT), 2018, pp. 1-3, doi: 10.1109/ICMMT.2018.8563468.

[98] A. A. AlAbdullah, N. Ali, H. Obeidat, R. A. Abd-Alhmeed and S. Jones, "Indoor millimetre-wave propagation channel simulations at 28, 39, 60 and 73 GHz for 5G wireless networks," 2017 Internet Technologies and Applications (ITA), 2017, pp. 235-239, doi: 10.1109/ITECHA.2017.8101945.

[99] M. Wang, Y. Liu, S. Li and Z. Chen, "60 GHz millimeter-wave propagation characteristics in indoor environment," 2017 IEEE 9th International Conference on Communication Software and Networks (ICCSN), 2017, pp. 749-752, doi: 10.1109/ICCSN.2017.8230211.

[100] Z. Sheng, Y. Liu, Z. Chen, S. Li and X. Zhang, "Study on the RMS and path loss of 60GHz millimeter-wave in typical indoor environment," 2017 Sixth Asia-Pacific Conference on Antennas and Propagation (APCAP), 2017, pp. 1-3, doi: 10.1109/APCAP.2017.8420746.

[101] J. Ruan and Y. Zhang, "Simulation of 60GHz Millimeter-wave Propagation Characteristics Based on SBR Method in Stairwell," 2019 International Applied Computational Electromagnetics Society Symposium - China (ACES), 2019, pp. 1-2, doi: 10.23919/ACES48530.2019.9060568.

[102] D. M. Rose, S. Rey and T. Kürner, "Differential 3D ray-launching using arbitrary polygonal shapes in time-variant indoor scenarios," 2016 Global Symposium on Millimeter Waves (GSMM) & ESA Workshop on Millimetre-Wave Technology and Applications, 2016, pp. 1-4, doi: 10.1109/GSMM.2016.7500285.

[103] F. Voineau et al., "A 12 Gb/s 64QAM and OFDM compatible millimeter-wave communication link using a novel plastic waveguide design," 2018 IEEE Radio and Wireless Symposium (RWS), 2018, pp. 250-252, doi: 10.1109/RWS.2018.8305001.

[104] K. Guan et al., "Complete Propagation Model in Tunnels," in IEEE Antennas and Wireless Propagation Letters, vol. 12, pp. 741-744, 2013, doi: 10.1109/LAWP.2013.2270937.

[105] D. G. Dudley, M. Lienard, S. F. Mahmoud and P. Degauque, "Wireless propagation in tunnels," in IEEE Antennas and Propagation Magazine, vol. 49, no. 2, pp. 11-26, April 2007, doi: 10.1109/MAP.2007.376637.

[106] Z. Hu, P. Zhang, H. Wang, Y. Zhou, X. An and H. Wang, "Ray-Tracing Based Millimeter-Wave Large-Scale Channel Characteristics in Corridor Environment," 2019 International Symposium on Antennas and Propagation (ISAP), 2019, pp. 1-3.

[107] Q. Li et al., "Validation of a Geometry-Based Statistical mm-wave Channel Model Using Ray-Tracing Simulation," 2015 IEEE 81st Vehicular Technology Conference (VTC Spring), 2015, pp. 1-5, doi: 10.1109/VTCSpring.2015.7146155.

[108] B. Colo, A. Fouda and A. S. Ibrahim, "Ray Tracing Simulations in Millimeter-Wave Vehicular Communications," 2019 IEEE 30th Annual International Symposium on Personal, Indoor and Mobile Radio Communications (PIMRC), 2019, pp. 1-4, doi: 10.1109/PIMRC.2019.8904154.

[109] N. R. Leonor, T. R. Fernandes, M. García Sánchez and R. F. S. Caldeirinha, "A 3-D Model for Millimeter-Wave Propagation Through Vegetation Media Using Ray-Tracing," in IEEE Transactions on Antennas and Propagation, vol. 67, no. 6, pp. 4313-4318, June 2019, doi: 10.1109/TAP.2019.2905957.

[110] Z. Gao, B. Liu, Z. Cheng, C. Chen and L. Huang, "Marine mobile wireless channel modeling based on improved spatial partitioning ray tracing," in China Communications, vol. 17, no. 3, pp. 1-11, March 2020, doi: 10.23919/JCC.2020.03.001.

[111] Chang-Fa Yang, Boau-Cheng Wu and Chuen-Jyi Ko, "A ray-tracing method for modeling indoor wave propagation and penetration," in IEEE Transactions on Antennas and Propagation, vol. 46, no. 6, pp. 907-919, June 1998, doi: 10.1109/8.686780.

[112] Shung-Wu Lee and G. Deschamps, "A uniform asymptotic theory of electromagnetic diffraction by a curved wedge," in IEEE Transactions on Antennas and Propagation, vol. 24, no. 1, pp. 25-34, January 1976, doi: 10.1109/TAP.1976.1141283.

[113] Sharaf, Marwa H et al. “A Novel Dual-Band (38/60 GHz) Patch Antenna for 5G Mobile Handsets.” Sensors (Basel, Switzerland) vol. 20,9 2541. 29 Apr. 2020, doi:10.3390/s20092541

[114] S. Yang, Z. Yan, M. Cai, F. Fan and T. Zhang, "A High-Efficiency Double-Layer Transmitarray Antenna Using Low-Loss Dual-Linearly Polarized Elements," in IEEE Antennas and Wireless Propagation Letters, vol. 19, no. 12, pp. 2378-2382, Dec. 2020, doi: 10.1109/LAWP.2020.3033460.

[115] K. Pookkapund, A. Sakonkanapong, R. Kuse, C. Phongcharoenpanich and T. Fukusako, "Broadband Circularly Polarized Microstrip Patch Antenna Using Circular Artificial Ground Structure and Meandering Probe," in IEEE Access, vol. 8, pp. 173854-173864, 2020, doi: 10.1109/ACCESS.2020.3026166.

[116] W. Yang, K. Ma, K. S. Yeo and W. M. Lim, "A Compact High-Performance Patch Antenna Array for 60-GHz Applications," in IEEE Antennas and Wireless Propagation Letters, vol. 15, pp. 313-316, 2016, doi: 10.1109/LAWP.2015.2443054.

[117] W. M. Imran Wan Mohd Zamri and N. C. Karmakar, "4 by 4 ultra-wideband milimeter-wave printed log-periodic dipole array antenna," 2015 IEEE International Symposium on Antennas and Propagation & USNC/URSI National Radio Science Meeting, 2015, pp. 2427-2428, doi: 10.1109/APS.2015.7305602.

[118] W. E. McKinzie, D. M. Nair, B. A. Thrasher, M. A. Smith, E. D. Hughes and J. M. Parisi, "60-GHz 2x2 LTCC Patch Antenna Array With an Integrated EBG Structure for Gain Enhancement," in IEEE Antennas and Wireless Propagation Letters, vol. 15, pp. 1522-1525, 2016, doi: 10.1109/LAWP.2016.2517141.

[119] I. Chen, Y. Tseng and T. Wu, "Beamforming broadside antenna array for 60-GHz technology," 2016 IEEE International Symposium on Radio-Frequency Integration Technology (RFIT), 2016, pp. 1-3, doi: 10.1109/RFIT.2016.7578182.

[120] P. Roy, R. K. Vishwakarma, A. Jain and R. Singh, "Multiband millimeter wave antenna array for 5G communication," 2016 International Conference on Emerging Trends in Electrical Electronics & Sustainable Energy Systems (ICETEESES), 2016, pp. 102-105, doi: 10.1109/ICETEESES.2016.7581361.

[121] D. Zarifi, A. Farahbakhsh and A. U. Zaman, "A Gap Waveguide-Fed Wideband Patch Antenna Array for 60-GHz Applications," in IEEE Transactions on Antennas and Propagation, vol. 65, no. 9, pp. 4875-4879, Sept. 2017, doi: 10.1109/TAP.2017.2722866.

[122] B. Hu, F. Tang, P. Chen and X. Yu, "Fractal UWB patch antenna with omnidirectional pattern," 2017 Sixth Asia-Pacific Conference on Antennas and Propagation (APCAP), 2017, pp. 1-3, doi: 10.1109/APCAP.2017.8420579.

[123] A. Martin, O. Lafond, M. Himdi and X. Castel, "Improvement of 60 GHz Transparent Patch Antenna Array Performance Through Specific Double-Sided Micrometric Mesh Metal Technology," in IEEE Access, vol. 7, pp. 2256-2262, 2019, doi: 10.1109/ACCESS.2018.2886478.

[124] L. Wang, W. Fang, W. Shao, B. Yao, Y. Huang and Y. En, "Broadband Circularly Polarized Cross-Dipole Antenna With Multiple Modes," in IEEE Access, vol. 8, pp. 66489-66494, 2020, doi: 10.1109/ACCESS.2020.2981050.

[125] A. Ghaneizadeh, M. Joodaki, J. Börcsök, A. Golmakani and K. Mafinezhad, "Analysis, Design, and Implementation of a New Extremely Ultrathin 2-D-Isotropic Flexible Energy Harvester Using Symmetric Patch FSS," in IEEE Transactions on Microwave Theory and Techniques, vol. 68, no. 6, pp. 2108-2115, June 2020, doi: 10.1109/TMTT.2020.2982386.

[126] Y. Zheng and S. Yan, "A Low-profile Wideband Pattern and Polarization Diversity Antenna," 2019 Cross Strait Quad-Regional Radio Science and Wireless Technology Conference (CSQRWC), 2019, pp. 1-3, doi: 10.1109/CSQRWC.2019.8799145.

[127] Z. -F. Wu, W. -J. Lu, J. Yu and L. Zhu, "Wideband Null Frequency Scanning Circular Sector Patch Antenna Under Triple Resonance," in IEEE Transactions on Antennas and Propagation, vol. 68, no. 11, pp. 7266-7274, Nov. 2020, doi: 10.1109/TAP.2020.2995459.

[128] A. Jaiswal, M. P. Abegaonkar and S. K. Koul, "2×1 Tapered Recessed Ground Microstrip Patch Antenna Array at 60 GHz," 2019 IEEE Indian Conference on Antennas and Propogation (InCAP), 2019, pp. 1-4, doi: 10.1109/InCAP47789.2019.9134625.

[129] P. Zhang, H. Yi, H. Liu, H. Yang, G. Zhou and L. Li, "Back-to-Back Microstrip Antenna Design for Broadband Wide-Angle RF Energy Harvesting and Dedicated Wireless Power

Transfer," in IEEE Access, vol. 8, pp. 126868-126875, 2020, doi: 10.1109/ACCESS.2020.3008551.

[130] S. Adamshick, S. R. Govindarajulu and E. A. Alwan, "A Novel Low Loss 3D System-in-Package Approach for 60GHz Antenna on Chip Applications," 2020 IEEE 63rd International Midwest Symposium on Circuits and Systems (MWSCAS), 2020, pp. 537-540, doi: 10.1109/MWSCAS48704.2020.9184617.

[131] Jeong-Geun Kim, Hyung Suk Lee, Ho-Seon Lee, Jun-Bo Yoon and S. Hong, "60-GHz CPW-fed post-supported patch antenna using micromachining technology," in IEEE Microwave and Wireless Components Letters, vol. 15, no. 10, pp. 635-637, Oct. 2005, doi: 10.1109/LMWC.2005.856690.

[132] J. Zhu, Y. Yang, C. Chu, S. Li, S. Liao and Q. Xue, "Low-Profile Wideband and High-Gain LTCC Patch Antenna Array for 60 GHz Applications," in IEEE Transactions on Antennas and Propagation, vol. 68, no. 4, pp. 3237-3242, April 2020, doi: 10.1109/TAP.2019.2949913.

[133] A. Jaiswal, M. P. Abegaonkar and S. K. Koul, "60 GHz Recessed Ground Plane Microstrip Patch Antenna Array with Improved Bandwidth and Gain," 2018 IEEE Indian Conference on Antennas and Propogation (InCAP), 2018, pp. 1-4, doi: 10.1109/INCAP.2018.8770834.

[134] T. H. Jang, H. Y. Kim, I. S. Song, C. J. Lee, J. H. Lee and C. S. Park, "A Wideband Aperture Efficient 60-GHz Series-Fed E-Shaped Patch Antenna Array With Copolarized Parasitic Patches," in IEEE Transactions on Antennas and Propagation, vol. 64, no. 12, pp. 5518-5521, Dec. 2016, doi: 10.1109/TAP.2016.2621023.

[135] A. Jaiswal, M. P. Abegaonkar and S. K. Koul, "Highly Efficient, Wideband Microstrip Patch Antenna With Recessed Ground at 60 GHz," in IEEE Transactions on Antennas and Propagation, vol. 67, no. 4, pp. 2280-2288, April 2019, doi: 10.1109/TAP.2019.2894319.

[136] C. Tseng, C. Chen and T. Chu, "A Low-Cost 60-GHz Switched-Beam Patch Antenna Array With Butler Matrix Network," in IEEE Antennas and Wireless Propagation Letters, vol. 7, pp. 432-435, 2008, doi: 10.1109/LAWP.2008.2001849.

[137] H. Vettikalladi, O. Lafond and M. Himdi, "High-Efficient and High-Gain Superstrate Antenna for 60-GHz Indoor Communication," in IEEE Antennas and Wireless Propagation Letters, vol. 8, pp. 1422-1425, 2009, doi: 10.1109/LAWP.2010.2040570.

[138] W. M. Abdel-Wahab and S. Safavi-Naeini, "Wide-Bandwidth 60-GHz Aperture-Coupled Microstrip Patch Antennas (MPAs) Fed by Substrate Integrated Waveguide (SIW)," in IEEE Antennas and Wireless Propagation Letters, vol. 10, pp. 1003-1005, 2011, doi: 10.1109/LAWP.2011.2168373.

[139] H. Sun, Y. Guo and Z. Wang, "60-GHz Circularly Polarized U-Slot Patch Antenna Array on LTCC," in IEEE Transactions on Antennas and Propagation, vol. 61, no. 1, pp. 430-435, Jan. 2013, doi: 10.1109/TAP.2012.2214018.

[140] W. Zhang, Y. P. Zhang, M. Sun, C. Luxey, D. Titz and F. Ferrero, "A 60-GHz Circularly-Polarized Array Antenna-in-Package in LTCC Technology," in IEEE Transactions on Antennas and Propagation, vol. 61, no. 12, pp. 6228-6232, Dec. 2013, doi: 10.1109/TAP.2013.2279992.

[141] K. Chin, W. Jiang, W. Che, C. Chang and H. Jin, "Wideband LTCC 60-GHz Antenna Array With a Dual-Resonant Slot and Patch Structure," in IEEE Transactions on Antennas and Propagation, vol. 62, no. 1, pp. 174-182, Jan. 2014, doi: 10.1109/TAP.2013.2287294.

[142] Y. Li and K. Luk, "Low-Cost High-Gain and Broadband Substrate- Integrated-Waveguide-Fed Patch Antenna Array for 60-GHz Band," in IEEE Transactions on Antennas and Propagation, vol. 62, no. 11, pp. 5531-5538, Nov. 2014, doi: 10.1109/TAP.2014.2350509.

[143] R. K. Mishra, "Simple method for determining the bandwidth of rectangular patch antenna," IEEE Antennas and Propagation Society International Symposium. Transmitting Waves of Progress to the Next Millennium. 2000 Digest. Held in conjunction with: USNC/URSI National Radio Science Meeting (C, 2000, pp. 1402-1405 vol.3, doi: 10.1109/APS.2000.874466.

[144] A. E. I. Lamminen, J. Saily and A. R. Vimpari, "60-GHz Patch Antennas and Arrays on LTCC With Embedded-Cavity Substrates," in IEEE Transactions on Antennas and Propagation, vol. 56, no. 9, pp. 2865-2874, Sept. 2008, doi: 10.1109/TAP.2008.927560.

[145] A. D. Johnson, J. Zhong, S. B. Venkatakrishnan, E. A. Alwan and J. L. Volakis, "Phased Array With Low-Angle Scanning and 46:1 Bandwidth," in IEEE Transactions on Antennas and Propagation, vol. 68, no. 12, pp. 7833-7841, Dec. 2020, doi: 10.1109/TAP.2020.2998869.

[146] T. Manabe, Y. Miura and T. Ihara, "Effects of antenna directivity and polarization on indoor multipath propagation characteristics at 60 GHz," in IEEE Journal on Selected Areas in Communications, vol. 14, no. 3, pp. 441-448, April 1996, doi: 10.1109/49.490229.

[147] Y. J. Yoon and B. Kim, "A new formula for effective dielectric constant in multi-dielectric layer microstrip structure," IEEE 9th Topical Meeting on Electrical Performance of Electronic Packaging (Cat. No.00TH8524), 2000, pp. 163-167, doi: 10.1109/EPEP.2000.895519.

[148] T. H. Jang, Y. H. Han, J. Kim and C. S. Park, "60 GHz Wideband Low-Profile Circularly Polarized Patch Antenna With an Asymmetric Inset," in IEEE Antennas and Wireless

Propagation Letters, vol. 19, no. 1, pp. 44-48, Jan. 2020, doi: 10.1109/LAWP.2019.2952405.

[149] H. Zhang, S. Venkateswaran and U. Madhow, "Channel Modeling and MIMO Capacity for Outdoor Millimeter Wave Links," 2010 IEEE Wireless Communication and Networking Conference, 2010, pp. 1-6, doi: 10.1109/WCNC.2010.5506714.

[150] S. Kirthiga, M. Jayakumar, "Performance Studies and Review of Millimeter Wave MIMO Beamforming at 60 GHz", Procedia Technology, vol. 21, pp 658-666, 2015.

[151] G. Yue, Z. Wang, L. Chen, L. Cheng, J. Tang, X. Zou, Y. Zeng, L. Li " Demonstration of 60 GHz millimeter-wave short-range wireless communication system at 3.5 Gbps over 5 m range," 2017 Science China Information Sciences), vol. 60, no. 8, June 2017.

[152] O. K. Tonguz, A. E. Xhafa, D. D. Stancil, A. G. Cepni, P. V. Nikitin and D. Brodtkorb, "A simple path-loss prediction model for HVAC systems," in IEEE Transactions on Vehicular Technology, vol. 53, no. 4, pp. 1203-1214, July 2004, doi: 10.1109/TVT.2004.830143.

[153] Esha Bangar and Kamran Kiasaleh, "Evaluating Performance of Heating, Ventilation & Air Conditioning Duct Communication Channel at 60 GHz Using Ray Tracing," Progress In Electromagnetics Research C, Vol. 113, 177-195, 2021. doi:10.2528/PIERC21040906.

[154] Banday, Y., Mohammad Rather, G. and Begh, G.R. (2019), Effect of atmospheric absorption on millimetre wave frequencies for 5G cellular networks. IET Communications, 13: 265-270. https://doi.org/10.1049/iet-com.2018.5044.

## BIOGRAPHICAL SKETCH

Esha Bangar was born in Sagour, Madhya Pradesh, India. After completing her schoolwork at St. Joseph Convent School and Army Public School in Sagour in 2005, Esha entered Indira Gandhi Engineering College in Sagour, for her undergraduate studies in Electronics and Communication Engineering. She did summer internship at Bharat Sanchar Nigam Limited in 2008 and attended a robotics workshop conducted by IIT Mumbai in 2009. She cleared Graduate Aptitude Test in Engineering in 2009 which helped her secure an admission in National Institute of Technology (NIT) Kurukshetra for her graduate studies. She also cleared Joint Admission Test for MSc with an All-India Rank of 73. She started her master's in technology studies in 2010 at NIT Kurukshetra. She worked as a teaching assistant for most of her time at NIT. After completing her master's in 2012, Esha started working for Tata Consultancy Services (TCS) in Hyderabad as a trainee in 2013. She moved to Mumbai, Maharashtra, working as a system engineer for TCS, where she worked from 2013 to 2016. In 2016, she moved to Dallas, Texas to begin her PhD studies at The University of Texas at Dallas. She also did an internship at Ansys Inc in Pittsburgh from 2018 August to 2019 August. After her graduation, she is planning to work as an Antenna Engineer in San Diego, California.

# CURRICULUM VITAE

BTech., ECE, RGTU, India (GPA: 8.9/10) 2006 - 2010

MTech., Comm. Engineering, NIT, India (GPA: 9.2/10) 2010 - 2012

- Design of wearable antennas for body area networks using mmwave frequency.
- Spectrum management through cognitive radio technology.

PhD, EE (Wireless RF & Antenna), UT Dallas (GPA: 3.78/4) 2016 - Present

Dissertation – Indoor Heating, Ventilation and Air Conditioning (HVAC) communication realization through high gain ultra-wideband milimeter-wave (mmwave) antenna array.

- Theoretical modelling of HVAC duct using Geometric Optics -
  - Link budget and channel frequency response calculation.
  - Determination of throughput, RSSI, BER, EVM, SNR for different modulation and coding schemes.
  - Impedance matching, TRP and TIS calculation, antenna characterization.
- Design and Simulation of PCB antennas -
  - Aperture coupled microstrip line fed patch with cavity and 4 x 4 array on LTCC substrate.
  - Gain of 18 dB, beamwidth of $\pm$20 degrees, return loss of -12 dB.
- Design of a UWB LTCC substrate high gain cavity resonator dipole array -
  - Microstrip fed dipole structure is divided between the thick LTCC substrate's top and bottom layer.
  - Beam tilting and coupling reduced by a slot.
  - Gain of 10 dB, beamwidth of $\pm$30 degrees, BW 2 GHz with VSWR of 1.6.
- Comparison of theoretical, experimental and simulation results -
  - Experimental results obtained using IEEE 802.11ad/Wigig compliant chipsets.
  - 3D Raytracing simulation based on Image theory.

PUBLICATIONS

- E. Bangar and K. Kiasaleh, "Experimental Validation of the Performance of Heating, Ventilation and Air Conditioning Ducts as Communication Channel at 60 GHz" IEEE LANMAN, Orlando, FL, US, 2020.
- E. Bangar and K. Kiasaleh, "Characterization of Indoor Heating, Ventilation and Air Conditioning Duct System as a Communication Channels at 60 GHz" IEEE Texas Symposium on WMCS, Waco, TX, US, 2020.
- E. Bangar and B. Singh, "Two Stage detector comprising of weighted ED & a decision statistic based on GLRT for Cognitive Radio Networks", International Journal of Electrical, Electronics & Data Communication, Bangalore, Karnataka, India, 2014.

- N. Taherkhani, E. Bangar and K. Kiasaleh, "A Low Complexity M-QAM Soft De-mapping Method in Alpha Stable Field of Interference," 2020 IEEE Texas Symposium on WMCS, Waco, TX, US, 2020.
- E Bangar, N Taherkhani, K Kiasaleh, “Sum Rate Capacity of MIMO HetNet Systems in the Presence of Channel Estimation Error”, arXiv preprint arXiv:1909.10105, 2019.
- Esha Bangar and Kamran Kiasaleh, "Evaluating Performance of Heating, Ventilation & Air Conditioning Duct Communication Channel at 60 GHz Using Ray Tracing," Progress In Electromagnetics Research C, Vol. 113, 177-195, 2021. doi:10.2528/PIERC21040906.

WORK EXPERIENCE

Graduate Research Assistant and Teaching Assistant Aug 2016 – Dec 2020

- Signals and systems
- Electrical circuits lab
- Digital communication system
- Digital Signal Processing

IoT Research Intern, Null IoT LLC May 2018 – Aug 2018

- Design of flexible wearable antennas for IoT wireless communication domain.
- Smart antenna design using channel estimation error knowledge for beamforming.
- Application of sparse approximation algorithms for hybrid beamforming techniques.

Research & Development Intern, Ansys Inc Aug 2018 – Aug 2019

(1) Worked on around 60 antenna designs –
   - Arrays: driven dipole, 8x8 microstrip patch, stacked patch, Vivaldi, cavity, reflectarray.
   - Reflectors: Parabolic, dish with horn at 60 GHz, asymmetric dish, two reflectors with horn.
   - Helix, Yagi-Uda, log-periodic toothed trapezoidal, PIFA, IFA etc.

(2) Feature Testing and Data Analysis –
   - Solver Slider Bar
   - Iterative Solver
   - Discrete Sweep with Dynamic Scheduling
   - Domain Decomposition Matrix Solver.

(3) Extension of HFSS Test Suite using Python